Wind Vibration Analysis
Giant Magellan Telescope

prepared for

Carnegie Observatories
813 Santa Barbara Street
Pasadena, CA 91101

prepared by

Simpson Gumpertz & Heger Inc.
41 Seyon Street, Building 1, Suite 500
Waltham, MA 02453
Tel.: 781 907-9000
Fax: 781 907-9009

Project 050241 30 January 2006

Table of Contents

CONTENTS[1] **Page**

ILLUSTRATIONS

[1]Bold capitalized headings are tab indexed.

APPENDIX

1. INTRODUCTION

1.1 Purposes

The purposes of the wind vibration analysis are

- to study the dynamic response of the Giant Magellan Telescope (GMT) baseline structure to wind disturbance with the goal of determining order of magnitude motions of the optical components which include the primary mirrors, the secondary mirrors, and the instrument platform,

- to identify possible changes to the structure to improve the pointing accuracy of the baseline telescope.

1.2 Scope

The scope of work for this study includes

1. developing a finite element model of the GMT baseline telescope structure by converting and combining existing ALGOR models of the telescope structure and instrument platform into MSC/NASTRAN,

2. calculating the dynamic wind loads on the GMT structure based on wind measurements at Gemini South,

3. performing eigenvalue analysis to determine natural frequencies and mode shapes of the baseline configuration,

4. performing random response analysis to determine the order of magnitude response to dynamic wind loads,

5. identifying areas in the structure that significantly affect the pointing error and perform sensitivity study on alternative configurations,

6. repeating Steps 3 and 4 on recommended configuration.

1.3 Overview of GMT

The Giant Magellan Telescope (GMT) shown in Fig. 1-1 is to be a 21.5 m equivalent aperture optical-infrared telescope located in Chile. The segmented mirror surface consists of seven 8.4 m diameter borosilicate honeycomb mirrors. Each primary mirror is supported on hydraulic mounts connected to a mirror-cell structure. The cell-connector frame supports all seven mirror cells and the secondary truss at three bracket locations. The C-ring assembly supports the cell-connector frame, houses and supports the instrument platform, and defines the altitude axis via hydrostatic bearings. The azimuth structure consists of a large azimuth disk and four OSS support pedestals. The entire structure is supported by the azimuth track and pier, and is housed within a carousel-type enclosure.

2. FINITE ELEMENT MODEL

Mr. Steve Gunnels of Paragon Engineering supplied us with two ALGOR finite-element models for the baseline structure of GMT:

- GMT159 – Model of GMT with fine mesh on the primary mirror surfaces and with the OSS at zenith angle = 30°
- GMT161 – Model of instrument platform (IP)

We translated the two ALGOR models into MSC/NASTRAN using FEMAP and combined the two models to create the baseline GMT finite-element model (FEM). The FEM is shown in Figs. 2-1 and 2-2.

There are a few coordinate systems used in the FEM (Fig. 2-3). The local mirror coordinate systems, the OSS-fixed coordinate system, and the global coordinate system are Cartesian coordinates fixed to the undeformed physical structure or ground.

The standard GMT OSS-fixed (x, y, z) coordinate system given in Ref. 1 is used:

> The OSS-fixed z-axis is coincident with the mechanical axis of the OSS and is positive upwards with the telescope pointing at zenith and defines the nominal optical axis of the telescope. The x-axis is coincident with the elevation axis and intersects the z-axis at the center of the telescope. The y-axis is perpendicular to the x- and z-axes and is positive in the upward direction with the telescope pointing away from zenith.

The (X, Y, Z) axes of the global coordinate system match those of the standard GMT Azimuth Platform coordinate system given in Ref. 1 with azimuth angle = 0°. The global Z-axis is coincident with the vertical rotation axis of the azimuth structure. The (X, Y, Z) axes are coincident with the (x, y, z) axes with the telescope pointed at zenith.

For the local mirror coordinate systems, the local mirror z'-axis is perpendicular to each mirror plane with the local x'-axis in the OSS-fixed x-z plane and the local y'-axis in the OSS-fixed y-z plane.

The primary mirrors are numbered from 1 to 6 clockwise starting at 12:00 and the center mirror is No. 7 (Fig. 2-3).

In the GMT baseline FEM, the primary mirror segments, the primary mirror cells, the cell-connector frame, the C-ring structures, the instrument platform, the azimuth disk, and the OSS pedestals are modeled by plate elements. The hexapod mirror support, the secondary truss,

the secondary support structure, and all the braces are modeled by beam elements. The weights of the secondary mirrors and their mirror cells are included as lumped masses. The stiffness of the hydrostatic bearings and the telescope drives are modeled by equivalent beam elements.

We modified the FEM to include wind loads on the primary mirror segments, primary mirror cells, secondary truss, secondary support structure, secondary mirror, and secondary mirror cell. The details on the wind loads are discussed in the next section.

We also added nodes, elements, and constraint equations to calculate the desired output. These include the following:

- One target node for each of the seven primary mirror segments on the telescope optical axis at the vertex of the parent conic surface. Each target node are connected to all the nodes on each mirror segment via a RBE3 interpolation element that computes the displacements and rotations of the target node using the least square weighted average approach.

- One target node for each of the seven primary mirror segments on the telescope optical axis on the focal plane. The pointing and focus errors are calculated using the optical sensitivity equations discussed in Section 4 as constraint equations.

- One extra target node on the telescope optical axis on the focal plane. The average pointing and focus errors weighted by mirror collecting areas are calculated using constraint equations.

- One encoder reading node on each axis of rotation. The azimuth and elevation encoder readings are calculated based on the rotations of the fixed and rotating parts of the encoders.

3. DYNAMIC WIND LOAD

In this section, we will present the wind measurement data and the methodology used in the development of the dynamic wind loads applied to different parts of the telescope structure in the wind vibration analyses.

Dynamic wind loads can be treated as random excitations that can be described only in a statistical sense. The instantaneous magnitude is not known at any given time; rather, the magnitude is expressed in terms of its statistical properties (such as mean value, standard deviation, and probability of exceeding a certain value). The random excitations are usually described in terms of power spectral density (PSD) functions.

3.1 Wind Data

The dynamic wind data used in this study are based on actual pressure and velocity measurements taken by Dr. David Smith at Gemini South Telescope atop Chile's Cerro Pachón [2]. The Gemini South Telescope has a single 8 m optical mirror. The Gemini South Telescope enclosure is shown in Fig. 3-1.

The test on Gemini South Telescope included twenty-four wind pressure measurements and five wind speed measurements for different wind directions (azimuth angle of attack), telescope orientations (zenith angles), upwind vent-gate positions, downwind vent-gate positions, and wind screen positions. The twenty-four pressure transducers were mounted on the dummy 8 m mirror cell over a 1.4 m by 1.4 m grid. Five three-axis ultrasonic anemometers were used to measure the wind speeds at top of the enclosure, at the secondary mirror, and at edge of the primary mirror at 3:00, 6:00, and 9:00 locations. All the records were 300 sec in length and were sampled at 10 Hz. Some pressure transducer measurements were also recorded on another system and were sampled at 200 Hz. The power spectral density and time history data are available on the AURA New Initiatives Office website [3].

The following two cases were chosen since they are real configurations which might occur during an observation:

- Case 1 – "a00030oo.dat": Vent gate open, wind screen open, telescope pointing into wind, and zenith angle = 30°.
- Case 2 – "a00030ccs.dat": Vent gate closed, wind screen closed, telescope pointing into wind, and zenith angle = 30°.

In both cases, the average outside wind speed was about 13 m/sec which matches typical operational wind speeds.

Since most of the Gemini South wind measurements were sampled at a rate of 10 Hz, we need to extrapolate the resulting PSD curves beyond 5 Hz. Examination of some of the data shows that the PSD curves for Case 2 do not roll off as quickly as those for Case 1. We did have some access to measurements made at Gemini South with 200 Hz sampling rate. Fig. 3-2 shows the pressure PSD of Pressure Tap 1 with 10 Hz and 200 Hz sampling rate for Cases 1 and 2. For Case 1, the data with 200 Hz sampling rate clearly shows a constant slope roll-off in the log-log scale beyond 5 Hz. For Case 2, both data sets appear to encounter a noise floor at the higher frequencies. The data with 200 Hz sampling rate shows a constant slope roll-off in the log-log scale from 1 to 5 Hz similar to that of Case 1. However, the data with 10 Hz sampling rate deviates from the 200 Hz data beyond 1 Hz. We do expect the actual spectra to have a constant slope roll-off on the log-log scale for Case 2 as well, and the discrepancies are probably results of limitations on measurement at low pressures.

3.2 Wind Loads on Telescope Structure

The pressure and velocity measurements described in the above section were used to develop the dynamic wind load spectra on different parts of the telescope structure. Wind loads were applied to the following areas: (1) primary mirror surfaces, (2) primary mirror cells, (3) secondary truss and secondary support structure, and (4) secondary mirror and secondary mirror cell. No wind load was applied to the back face of the primary mirror cells, the C-ring structure, the instrument platform, or other braces below the mirror surface. These areas were assumed to be shielded.

The basic methodology is to apply the wind loads in form of pressure, line load, and concentrated force/moment spectra to plate element, beam elements, and nodes, respectively. Loads are applied over regions consisting of elements or nodes. Loads within each region are assumed to be fully correlated, and loads from different regions are assumed to be uncorrelated.

To convert the velocity measurement into pressure PSD, we squared the velocity time history measurements and obtained the velocity squared PSD. We used the air density for an altitude of 9,000 ft in the calculation of the pressure PSD from the velocity squared PSD.

In the following sections, we will describe the wind loads applied to different parts of the telescope in details.

3.2.1 Primary Mirror Surfaces

We applied random excitation force and moment resultants to each of the seven primary mirrors. The power spectral densities of the force and moment resultants were computed based actual pressure measurements recorded on the M1 mirror at Gemini South. The force and moment time histories were calculated using the time histories of the twenty-four pressure taps and the tributary area of each pressure tap. The calculation conservatively assumes fully correlated pressure over the tributary area of a pressure tap. This methodology fully preserves all relevant time history pressure correlations over the surface of the mirror.

The power spectral densities of the force and moment resultants scaled to the size of the GMT mirror (8.4 m) are shown in Figs. 3-3 through 3-5 for Cases 1 and 2.

For Case 1 (vent gates open and wind screen open), there is little or no correlation among the force, moment about x-axis, and moment about y-axis. The force and moment resultants were applied as uncorrelated nodal forces and moments at the center of each mirror in its local mirror coordinate system. The resultants were distributed to all of the nodes of each mirror via a RBE3 interpolation element.

For Case 2 (vent gates closed and wind screen closed), we observed a correlation between the force and moment about x-axis due to uneven pressure distribution on the mirror face mainly along the y-direction. We believe this is in part due to the configuration of the wind screen resulting in a wind gradient on the mirror surface. We accounted for this gradient by applying the calculated moment resultants to each of the seven mirrors and by scaling the calculated force resultants for each mirror by the best fit line to the normalized cumulative energy of each pressure tap contained between 0.2 Hz and 2 Hz and the elevation of each tap (Fig. 3-6). The scaled force resultant PSD curves for the seven mirrors are shown in Fig. 3-3.

We also investigated an alternative method to apply the wind pressure on the primary mirrors. In this method, each mirror was divided into a number of zones over which pressure was assumed to be correlated. Wind pressures of adjacent regions were assumed to be

uncorrelated. The average of the wind pressure PSD recorded on Gemini South M1 mirror shown in Fig. 3-7 was used for all regions. We used a nine region (3 x 3) layout in this study.

3.2.2 Primary Mirror Cells

We applied random excitation pressure to the front edges and side faces of the primary mirror cells. For the front edges, we used the average of the wind pressure PSD recorded on the Gemini South M1 mirror. Six edge regions per cell were used. For the side faces, we calculated a reference pressure PSD based on the average of the velocity squared PSD recorded by three anemometers above the edges of the Gemini South M1 mirror cell. We used the air density for an altitude of 9,000 ft in calculating the reference pressure. We multiplied the reference pressure by a pressure coefficient to account for the shape of the mirror cell and orientation of face. The pressure coefficients around a short cylinder given in Ref. 4 were used. Each primary mirror cell was considered to be a separate cylinder assuming no interaction between adjacent mirror cells. We applied the pressure to the exposed side faces of the six outer mirror cells with each face as a region for a total of eighteen regions.

The power spectral densities of the pressure applied to the front edges and the reference pressure, without the pressure coefficient, used on the side faces of the primary mirror cell are shown in Figs 3-7 and 3-8 for Cases 1 and 2.

3.2.3 Secondary Truss and Secondary Support Structure

We applied distributed load to the secondary truss and the secondary support structure. We calculated a reference pressure PSD (Fig. 3-9) based on the average of the velocity squared PSD recorded by the anemometer located just above the Gemini South M2 mirror. A velocity factor of 1.17 was used to account for possible increase in wind velocity due to the increased height of the GMT relative to the Gemini South Telescope. We multiplied the reference pressure by a drag coefficient to account for the shape and orientation of the member. The drag coefficients in Ref. 4 were used. We applied distributed load in four separate regions along each of the six legs of the secondary truss. We also applied distributed load to each of the crossover braces and diagonal braces as separate regions. The secondary support structure was divided into three separate regions with distributed loads applied to the members.

3.2.4 Secondary Mirror and Secondary Mirror Cell

We applied nodal forces to the seven M2 mirrors and their mirror cells. We calculated a reference pressure PSD (Fig. 3-9) based on the average of the velocity squared PSD recorded

by the anemometer located just above the Gemini South M2 mirror. A velocity factor of 1.17 was used to account for possible increase in wind velocity due to the increased height of the GMT relative to the Gemini South Telescope. We computed the force on each of the seven mirror cells and applied concentrated force at the C.G. of each mirror-cell assembly. We conservatively considered the forces on the seven M2 mirrors are correlated. We also performed a sensitivity analysis with uncorrelated forces on the seven M2 mirrors.

4. OPTICAL SENSITIVITY EQUATIONS

We used the optical sensitivity equations to calculate the pointing and focus errors resulting from displacements and rotations of the optical components of the telescope, namely the seven primary mirror (M1) segments, the secondary mirrors (M2), and the instrument platform (IP). These equations were presented in Ref. 5 and were included in SGH's finite element model using constraint equations.

For each primary mirror segment, a target node is defined on the telescope optical axis at the vertex of the parent conic surface. The average displacements and rotations of each mirror segment at its target node are computed using a RBE3 interpolation element. The secondary mirrors are assumed to behave as a single mirror; therefore, the rigid body displacements and rotations at its vertex are used. For the instrument platform, the translations of the target node located at the nominal focus position are used.

4.1 Pointing Error

The x-y motions (mm) of the line of sight referenced to the unperturbed focal plane for each of the seven subapertures of the telescope are given by

$$\Delta_x^{(i)} = (-11.26) * x_1^{(i)} + (-1.966) * \Theta_{y,1}^{(i)} + (12.26) * x_2 + (-0.250) * \Theta_{y,2} + (-1.00) * x_3$$

$$\Delta_y^{(i)} = (-11.26) * y_1^{(i)} - (-1.966) * \Theta_{x,1}^{(i)} + (12.26) * y_2 - (-0.250) * \Theta_{x,2} + (-1.00) * y_3$$

where: i = 1 to 6 refer to the off-axis primary mirror segments and i = 7 refers to the center primary mirror segment (Fig. 2-3).

$x_1^{(i)}$ and $y_1^{(i)}$ are the x-y displacements (mm) of the target node representing the i^{th} primary mirror segment, respectively.

$\Theta_{x,1}^{(i)}$ and $\Theta_{y,1}^{(i)}$ are the rotations (arcsec) of the target node representing the i^{th} primary mirror segment about the x and y-axes, respectively.

x_2 and y_2 are the x-y displacements (mm) of the secondary mirror, respectively.

$\Theta_{x,2}$ and $\Theta_{y,2}$ are the rotations (arcsec) of the secondary mirror about the x and y-axes respectively.

x_3 and y_3 are the x-y displacements (mm) of the instrument platform, respectively.

The mean x-y displacements weighted by mirror collecting areas are calculated as

$$\Delta_x = 0.1465 * \sum_{i=1}^{6} \Delta_x^{(i)} + 0.1210 * \Delta_x^{(7)}$$

$$\Delta_y = 0.1465 * \sum_{i=1}^{6} \Delta_y^{(i)} + 0.1210 * \Delta_y^{(7)}$$

The values Δ_x and Δ_y may be converted to arcsec of image displacement by multiplying the displacement by the scale factor of 1.017 arcsec per millimeter (or 25.832 arcsec per inch).

4.2 Focus Error

The focus shift referenced to the unperturbed focal plane for each of the seven subapertures of the telescope is given by

$$\Delta_z^{(i)} = (-127) * z_1^{(i)} + (128) * z_2 + (-1.00) * z_3$$

where: i = 1 to 6 refer to the off-axis primary mirror segments and i = 7 refers to the center primary mirror segment (Fig. 2-3).

$z_1^{(i)}$ is the z-displacement (mm) of the target node representing the i^{th} primary mirror segment.

z_2 is the z-displacement (mm) of the secondary mirror.

z_3 is the z-displacement (mm) of the instrument platform.

The mean focus shift weighted by mirror collecting areas is

$$\Delta_z = 0.1465 * \sum_{i=1}^{6} \Delta_z^{(i)} + 0.1210 * \Delta_z^{(7)}$$

5. RANDOM RESPONSE ANALYSIS

We performed random vibration analyses to obtain wind response of the structure using the finite element model with the wind loads and the optical sensitivity equations described in the previous sections.

The following four conditions were analyzed (referred as Analyses A through D) for the baseline configuration:

- Locked rotor with 2% damping and Case 1 (vent gates open and wind screen open)
- Locked rotor with 2% damping and Case 2 (vent gates closed and wind screen closed)
- Locked rotor with 0.5% damping and Case 1 (vent gates open and wind screen open)
- Free rotor with 2% damping and Case 1 (vent gates open and wind screen open)

A series of analyses (referred as Analyses F through I) were performed to investigate different stiffening options for the secondary truss. For these analyses, we only used the following condition:

- Locked rotor with 2% damping and Case 1 (vent gates open and wind screen open)

After the stiffening options for the secondary truss were selected, the same four conditions were repeated for the recommended configuration (referred as Analyses L through N).

We also investigated the effects of the correlation of the forces on the M2 mirrors using the baseline configuration (referred as Analysis E) and the effects of the different methods of applying wind loads on the M1 mirrors using one of the secondary truss stiffening options (referred as Analysis J).

Table 5-1 shows a list of the analyses performed in this study. In all fourteen analyses, we used the modes between 0 and 30 Hz. The responses were calculated over a frequency range of 0.1 – 25 Hz. The power spectral density curves and RMS values of the following responses were calculated:

- Pointing and focus errors
- Displacements and rotations of the seven M1 mirrors projected to the center of the primary conic surface
- Displacements and rotations of the seven M1 mirrors in their local axes

- Displacements and rotations of the M2 mirror, instrument platform, and a node on the M2 support structure
- Accelerations of a node on the M2 support structure
- EL and AZ encoder readings

We also calculated the power spectral density curves and RMS values of the axial forces in the spring elements representing the elevation and azimuth drives.

Table 5-1 – List of Analyses Performed

Analyses for Baseline Configuration						
Analysis & Appendix No.	**Wind Case[1]**	**Rotor**	**M2 Loading**	**Damping**	**M1 Loading**	**Notes**
A	1	Locked	Correlated	2.0%	Force & Moments	
B	2	Locked	Correlated	2.0%	Force & Moments	
C	1	Locked	Correlated	0.5%	Force & Moments	
D	1	Free	Correlated	2.0%	Force & Moments	
E	1	Locked	Uncorrelated	2.0%	Force & Moments	
Analyses for Secondary Truss Stiffening Options						
Analysis & Appendix No.	**Wind Case[1]**	**Rotor**	**M2 Loading**	**Damping**	**M1 Loading**	**Notes**
F	1	Locked	Correlated	2.0%	Force & Moments	Option 1 – Braced Secondary Truss Support Bracket
G	1	Locked	Correlated	2.0%	Force & Moments	Option 2 – Option 1 and Braced Upper Truss
H	1	Locked	Correlated	2.0%	Force & Moments	Option 3 – Option 1 and Upper Truss with Double Wall Thickness
I	1	Locked	Correlated	2.0%	Force & Moments	Option 4 – Option 2 and Secondary Truss Legs with 50% Deeper Section
J	1	Locked	Correlated	2.0%	Large Pressure Zones	Option 1 – Braced Secondary Truss Support Bracket
Analyses for Recommended Configuration						
Analysis & Appendix No.	**Wind Case[1]**	**Rotor**	**M2 Loading**	**Damping**	**M1 Loading**	**Notes**
K	1	Locked	Correlated	2.0%	Force & Moments	
L	2	Locked	Correlated	2.0%	Force & Moments	
M	1	Locked	Correlated	0.5%	Force & Moments	
N	1	Free	Correlated	2.0%	Force & Moments	

[1] Wind Cases:
Case 1 – Vent Gates Open, Wind Screen Open, Telescope Pointing into Wind, and Zenith Angle = 30°
Case 2 – Vent Gates Closed, Wind Screen Closed, Telescope Pointing into Wind, and Zenith Angle = 30°

6. RESULTS FOR BASELINE CONFIGURATION

We performed eigenvalue analyses and random response analyses for the baseline configuration. The results of these analyses are shown in the following two sections.

6.1 Eigenvalue Analyses

We performed eigenvalue analyses for the baseline configuration with locked- and free-rotor conditions. The resulting natural frequencies and mode shapes are listed in Table 6-1 for the locked- and free-rotor conditions. The first eight mode shapes for the locked-rotor condition are shown in Figs. 6-1 through 6-8.

Table 6-1 – Natural Frequencies and Mode Shapes of Baseline Configuration

Locked Rotor			Free Rotor		
Mode	**Frequency (Hz)**	**Mode Shape**	**Mode**	**Frequency (Hz)**	**Mode Shape**
			1	0.00	Azimuth Rotation
			2	0.00	Elevation Rotation
1	4.43	Lateral Translation	3	4.05	Lateral Translation
2	5.40	Fore-Aft Translation	4	5.59	Fore-Aft Translation
3	5.59	Azimuth Rotation			
4	6.83	Secondary Truss Fore-Aft + Instrument Platform	5	6.85	Secondary Truss Fore-Aft + Instrument Platform
5	7.17	Secondary Truss Lateral	6	7.04	Secondary Truss Lateral
6	7.41	Secondary Truss Fore-Aft	7	7.57	Secondary Truss Fore-Aft
7	7.96	Secondary Truss Torsion	8	7.76	Secondary Truss Torsion
			9	7.93	Secondary Truss Torsion
8	8.01	Secondary Truss Lateral			

In addition to the natural frequencies and mode shapes listed above, there are many primary mirror modes (Fig. 6-9) with natural frequencies from 11.0 Hz to 12.5 Hz and many primary mirror-cell outer-wall out-of-plane bending modes (Fig. 6-10) with the natural frequencies from 12.8 Hz to 13.2 Hz. The secondary truss is active in a large number of modes.

6.2 Random Response Analyses

We performed random response analyses on the baseline configuration for the following four conditions (referred as Analyses A through D):

- Locked rotor with 2% damping and Case 1 (vent gates open and wind screen open)
- Locked rotor with 2% damping and Case 2 (vent gates closed and wind screen closed)
- Locked rotor with 0.5% damping and Case 1 (vent gates open and wind screen open)
- Free rotor with 2% damping and Case 1 (vent gates open and wind screen open)

The power spectral density and the cumulative energy curves for the pointing and focus errors of the four analyses are shown in Figs. 6-11 through 6-16. The RMS pointing and focus errors from 0.1 Hz to 25 Hz are summarized in Table 6-2. The detailed results for Analyses A through D are included in Appendices A through D.

Table 6-2 – RMS Pointing and Focus Errors for Baseline Configuration

	Analysis A Case 1 – Open Locked Rotor 2% Damping	**Analysis B Case 2 – Closed Locked Rotor 2% Damping**	**Analysis C Case 1 – Open Locked Rotor 0.5% Damping**	**Analysis D Case 1 – Open Free Rotor 2% Damping**
	RMS Pointing Error X Direction (arcsec)			
Minimum	0.206	0.077	0.471	5.455
Maximum	0.217	0.081	0.509	5.460
Weighted Mean	0.198	0.076	0.465	5.457
	RMS Pointing Error Y Direction (arcsec)			
Minimum	0.455	0.177	0.935	10.324
Maximum	0.475	0.184	0.986	10.327
Weighted Mean	0.459	0.179	0.947	10.326
	RMS Focus Error Z Direction (mm)			
Minimum	0.205	0.077	0.371	0.202
Maximum	0.338	0.117	0.730	0.337
Weighted Mean	0.250	0.093	0.457	0.246

6.3 Discussion of Results

Table 6-2 shows that the weighted mean RMS point errors for Case 1 (vent gates open and wind screen open) with locked rotor condition and 2% damping to be 0.198 and 0.459 arcsec in the x- and y-directions, respectively. The PSD curves for the x-direction pointing error in Fig. 6-11 show that there are four peaks at about 4.4, 5.5, 7.2, and 8.0 Hz, which match very well with the telescope lateral translation mode at 4.43 Hz, the telescope azimuth rotation mode at 5.59 Hz, the secondary truss lateral translation mode at 7.17 Hz, and the secondary truss lateral translation mode at 8.01 Hz, respectively. The cumulative energy curves in Fig. 6-12 show that the two secondary truss lateral translation modes at 7.17 and 8.01 Hz contribute significantly to the total error. Similar observations can be made on the PSD curves for the y-direction pointing error shown in Fig. 6-13. These are peaks at 5.4, 6.8, and 7.4 Hz, which match the telescope fore-aft translation mode at 5.40 Hz, the secondary truss fore-aft translation and instrument platform mode at 6.83 Hz, and the secondary truss fore-aft translation mode at 7.41 Hz, respectively. Fig. 6-14 also shows that the secondary truss fore-aft translation mode at 7.41 Hz contributes significantly to the total error.

Table 6-2 shows that the weighted mean RMS focus error for Case 1 (vent gates open and wind screen open) with locked-rotor condition and 2% damping to be 0.250 mm. The cumulative energy curves in Fig. 6-16 show that significant contribution to the total error occurs at about 14.7 Hz, which matches to a few of the secondary truss piston modes.

Therefore, for the baseline configuration, the modes of the secondary truss contribute significantly to the pointing and focus errors. Further examination of the relevant mode shapes shows that the secondary truss legs are bending in both the in-plane and out-of-plane directions and that the support brackets at the bases of the secondary truss legs are rotating. Stiffening the secondary truss and bracing its support brackets should improve the optical performance of the telescope. Different secondary truss stiffening options were analyzed. The details and the results are discussed in the next section.

Effect of Closed and Open Vent Gates and Wind Screen

The wind loads on the telescope structure for Case 2 (vent gates closed and wind screen closed) are significantly less than those for Case 1 (vent gates open and wind screen open). As shown in Table 6-2, the RMS pointing and focus errors for Case 2 are about 0.4 times those for Case 1.

Effect of Damping

Damping has a significant effect on the magnitude of the structural response to dynamic loadings. We expect the damping for the GMT structure to range from 0.5% to 2% of critical damping. Table 6-2 shows the RMS pointing error in the y-direction for 0.5% damping to be about 2.1 times that for 2% damping.

Effect of Free and Locked Rotor

The RMS pointing errors for the free-rotor condition are significantly higher than those for the locked-rotor condition because of the response of the two rigid body modes at zero frequency. The rigid body modes increase the pointing errors at low frequencies below 1 or 2 Hz. Above 2 Hz, the pointing responses do not change significantly. Since the pointing errors from 0.1 Hz to 1 Hz are mainly due to the rigid body modes and can be measured by the encoders, these pointing errors can be removed by the telescope main drives with a control system bandwidth up to 2 Hz. Therefore, we recomputed the RMS pointing and focus errors between 1 Hz and 25 Hz for both the locked- and free-rotor conditions. The results in Table 6-3 show

that the RMS pointing error in the y-direction for the free-rotor condition is about 1.4 times that for the locked rotor condition.

Table 6-3 – RMS Pointing and Focus Errors (1 Hz to 25 Hz) for Locked and Free Rotor

	Analysis A Case 1 – Open Locked Rotor 2% Damping	Analysis D Case 1 – Open Free Rotor 2% Damping
	RMS Pointing Error X Direction (arcsec)	
Minimum	0.197	0.211
Maximum	0.208	0.231
Weighted Mean	0.193	0.212
	RMS Pointing Error Y Direction (arcsec)	
Minimum	0.440	0.602
Maximum	0.460	0.630
Weighted Mean	0.445	0.614
	RMS Focus Error Z Direction (mm)	
Minimum	0.201	0.198
Maximum	0.316	0.314
Weighted Mean	0.243	0.240

7. RESULTS FOR SECONDARY TRUSS STIFFENING OPTIONS

The results of baseline configuration show that the main contributor to the pointing error is the motion of the secondary mirror. Examination of the relevant mode shapes shows that the rotational flexibility of the secondary truss support bracket and the bending flexibility (in plane and out of plane) of the secondary truss may be adding to the motion of the secondary mirror.

7.1 Random Response Analyses

We performed a series of random response analyses to examine the effect of the following secondary truss stiffening options (referred as Analyses F through I):

- **Option 1 – Braced Secondary Truss Support Bracket.** Two 5 in. diameter Schedule 40 pipes, as shown in Fig. 7-1, were added to stiffen the secondary truss support bracket against rotation.

- **Option 2 – Option 1 and Braced Upper Truss.** In addition to the braced secondary truss support bracket, diagonal and horizontal braces were added to the upper portion of the secondary truss as shown in Fig. 7-2. These braces were given the properties of a rectangular hollow steel tube 20 in. x 4 in. x 0.5 in. Distributed wind loads were applied to these braces.

- **Option 3 – Option 1 and Upper Truss with Double Wall Thickness.** In addition to the braced secondary truss support bracket, the areas and moments of inertia of the elements of the upper truss legs were doubled to approximate doubling of the wall thicknesses.

- **Option 4 – Option 2 and Secondary Truss Legs with 50% Deeper Section.** In addition to the braced secondary truss support bracket and the braced upper truss, the depths of the elements of the secondary truss legs were increased by a factor of 1.5. The distributed wind loads were also increased to account for the increased depth.

For all the above analyses, we used the locked rotor condition with 2% damping and Case 1 (vent gates open and wind screen open).

The power spectral density and the cumulative energy curves for the pointing and focus errors of the four analyses are shown in Figs. 7-3 through 7-8. The RMS pointing and focus errors from 0.1 Hz to 25 Hz are summarized in Table 7-1 together with those of the baseline configuration. The detailed results for Analyses F through I are included in Appendices F through I.

Table 7-1 – RMS Pointing and Focus Errors for Secondary Truss Stiffening Options

	Analysis A Baseline	Analysis F Option 1	Analysis G Option 2	Analysis H Option 3	Analysis I Option 4
	RMS Pointing Error X Direction (arcsec)				
Minimum	0.206	0.159	0.136	0.133	0.142
Maximum	0.217	0.189	0.146	0.155	0.156
Weighted Mean	0.198	0.153	0.123	0.122	0.128
	RMS Pointing Error Y Direction (arcsec)				
Minimum	0.455	0.364	0.274	0.295	0.283
Maximum	0.475	0.384	0.294	0.312	0.307
Weighted Mean	0.459	0.368	0.277	0.297	0.289
	RMS Focus Error Z Direction (mm)				
Minimum	0.205	0.197	0.143	0.162	0.140
Maximum	0.338	0.359	0.264	0.300	0.263
Weighted Mean	0.250	0.237	0.163	0.208	0.155

7.2 Discussion of Results

Table 7-1 shows that each of the stiffening options significantly reduces the pointing errors:

- **Option 1 – Braced Secondary Truss Support Bracket.** Adding braces to stiffen the secondary truss support bracket against rotation reduces the pointing errors to about 0.8 times those for the baseline configuration.

- **Option 2 – Option 1 and Braced Upper Truss.** Adding diagonal and horizontal braces to the upper portion of the secondary truss reduces the pointing errors to about 0.8 times those for Option 1.

- **Option 3 – Option 1 and Upper Truss with Double Wall Thickness.** Doubling the areas and moments of inertia of the elements of the upper truss legs reduces the pointing errors to about 0.8 times those for Option 1.

- **Option 4 – Option 2 and Secondary Truss Legs with 50% Deeper Section.** Increasing the depths of the secondary truss legs by a factor of 1.5 increases the pointing errors to about 1.05 times those for Option 2. This is probably the results of the increased wind load on the deeper section.

Based on the above results, we recommend using a configuration that includes addition of braces to stiffen the secondary truss support brackets (Option 1), addition of diagonal and horizontal braces to the upper truss (Option 2), and the increased thickness of upper truss (Option 3).

8. RESULTS FOR RECOMMENDED CONFIGURATION

The results of the analyses on secondary truss stiffening options show that the addition of braces to stiffen the secondary truss support brackets (Option 1), addition of diagonal and horizontal braces to the upper truss (Option 2), and the increased thickness of upper truss (Option 3) all reduce the pointing error. A recommended configuration using all of these modifications was examined.

We performed eigenvalue analyses and random response analyses for the recommended configuration. The results of these analyses are shown in the following two sections.

8.1 Eigenvalue Analysis

We performed eigenvalue analyses for the recommended configuration with locked- and free-rotor conditions. The resulting natural frequencies are shown in Table 8-1 for the locked- and free-rotor conditions. The first nine mode shapes for the locked-rotor condition are shown in Figs. 8-1 through 8-9.

Table 8-1 – Natural Frequencies and Mode Shapes of Recommended Configuration

Locked Rotor			Free Rotor		
Mode	**Frequency (Hz)**	**Mode Shape**	**Mode**	**Frequency (Hz)**	**Mode Shape**
			1	0.00	Azimuth Rotation
			2	0.00	Elevation Rotation
1	4.40	Lateral Translation	3	4.00	Lateral Translation
2	5.35	Fore-Aft Translation	4	5.59	Fore-Aft Translation
3	5.57	Azimuth Rotation			
4	6.85	Secondary Truss Fore-Aft + Instrument Platform	5	6.87	Secondary Truss Fore-Aft + Instrument Platform
5	7.31	Secondary Truss Lateral	6	7.12	Secondary Truss Lateral
6	7.75	Secondary Truss Fore-Aft			Secondary Truss Fore-Aft
7	8.41	Secondary Truss 2:00 to 7:00	7	8.25	Secondary Truss 2:00 to 7:00
8	8.51	Secondary Truss 5:00 to 11:00	8	8.35	Secondary Truss 5:00 to 11:00
			9	8.68	Secondary Truss Out-of-Plane Bending
9	9.37	Secondary Truss Torsion	10	9.26	Secondary Truss Torsion

In addition to the natural frequencies and mode shapes listed above, there are many primary mirror modes with natural frequencies from 11.1 Hz to 12.5 Hz and many primary mirror-cell outer wall out-of-plane bending modes with natural frequencies from 12.9 Hz to 13.7 Hz. The secondary truss is active in a large number of modes.

8.2 Random Response Analyses

We performed random response analyses on the baseline configuration for the following four conditions (referred as Analyses K through N):

- Locked rotor with 2% damping and Case 1 (vent gates open and wind screen open)
- Locked rotor with 2% damping and Case 2 (vent gates closed and wind screen closed)
- Locked rotor with 0.5% damping and Case 1 (vent gates open and wind screen open)
- Free rotor with 2% damping and Case 1 (vent gates open and wind screen open)

The power spectral density and the cumulative energy curves for the pointing and focus errors of the four analyses are shown in Figs. 8-10 through 8-15. The RMS pointing and focus errors from 0.1 Hz to 25 Hz are summarized in Table 8-2. The detailed results for Analyses K through N are included in Appendices K through N.

Table 8-2 – RMS Pointing and Focus Errors for Recommended Configuration

	Analysis K Case 1 – Open Locked Rotor 2% Damping	**Analysis L Case 2 – Closed Locked Rotor 2% Damping**	**Analysis M Case 1 – Open Locked Rotor 0.5% Damping**	**Analysis N Case 1 – Open Free Rotor 2% Damping**
	RMS Pointing Error X Direction (arcsec)			
Minimum	0.106	0.036	0.209	5.422
Maximum	0.117	0.040	0.236	5.426
Weighted Mean	0.091	0.035	0.184	5.424
	RMS Pointing Error Y Direction (arcsec)			
Minimum	0.196	0.077	0.355	10.706
Maximum	0.211	0.083	0.394	10.710
Weighted Mean	0.195	0.078	0.364	10.708
	RMS Focus Error Z Direction (mm)			
Minimum	0.121	0.046	0.223	0.115
Maximum	0.230	0.074	0.431	0.229
Weighted Mean	0.143	0.052	0.271	0.138

8.3 Discussion of Results

Comparing Table 8-2 to Table 6-2 shows that the pointing and focus errors for recommended configuration are about 0.5 times those for the baseline configuration. As shown in Figs. 8-10 through 8-15, the peaks in PSD curves from the secondary truss modes have been significantly reduced as the results of the secondary truss stiffening.

Effect of Closed and Open Vent Gates and Wind Screen

The wind loads on the telescope structure for Case 2 (vent gates closed and wind screen closed) are significantly less than those for Case 1 (vent gates open and wind screen open). As

shown in Table 8-2, the RMS pointing and focus errors for Case 2 are about 0.4 times those for Case 1.

Effect of Damping

Damping has a significant effect on the magnitude of the structural response to dynamic loadings. We expect the damping for the GMT structure to range from 0.5% to 2% of critical damping. Table 8-2 shows the RMS pointing error in the y-direction for 0.5% damping to be about 1.9 times that for 2% damping.

Effect of Free and Locked Rotor

The RMS pointing errors for the free-rotor condition are significantly higher than those for the locked-rotor condition because of the response of the two rigid body modes at zero frequency. The rigid body modes increase the pointing errors at low frequencies below 1 or 2 Hz. Above 2 Hz, the pointing responses do not change significantly. Since the pointing errors from 0.1 Hz to 1 Hz are mainly due to the rigid body modes and can be measured by the encoders, these pointing errors can be removed by the telescope main drives with a control system bandwidth up to 2 Hz. Therefore, we recomputed the RMS pointing and focus errors between 1 Hz and 25 Hz for both the locked- and free-rotor conditions. The results in Table 8-3 show that the RMS pointing error in the y-direction for the free-rotor condition is about 1.6 times that for the locked-rotor condition.

Table 8-3 – RMS Pointing and Focus Errors (1 Hz to 25 Hz) for Locked and Free Rotor

	Analysis L Case 1 – Open Locked Rotor 2% Damping	**Analysis N Case 1 – Open Free Rotor 2% Damping**
	RMS Pointing Error X Direction (arcsec)	
Minimum	0.092	0.097
Maximum	0.106	0.110
Weighted Mean	0.086	0.092
	RMS Pointing Error Y Direction (arcsec)	
Minimum	0.182	0.289
Maximum	0.196	0.312
Weighted Mean	0.184	0.296
	RMS Focus Error Z Direction (mm)	
Minimum	0.114	0.109
Maximum	0.200	0.198
Weighted Mean	0.133	0.128

9. RESULTS FOR OTHER SENSITIVITY ANALYSES

We performed additional random response analyses to investigate the effects of the correlation of the forces on the M2 mirrors and the effects of the different methods of applying wind loads on the M1 mirrors.

9.1 Correlated and Uncorrelated Forces on M2

We performed random response analyses using the baseline configuration with correlated and uncorrelated forces on the M2 mirrors. The wind loads on the seven M2 mirrors were applied as concentrated forces at the C.G. of the seven mirror-cell assemblies. These forces can be considered fully correlated or uncorrelated. The correlated forces will impose a larger combined force on the secondary support structure but will not impose the additional resultant moment that may occur due to the difference in forces among the seven M2 mirrors. In this comparison, we used the locked rotor condition with 2% damping and Case 1 (vent gates open and wind screen open).

The RMS pointing and focus errors from 0.1 Hz to 25 Hz with the correlated and uncorrelated forces on the M2 mirrors are summarized in Table 9-1. The detailed results for Analyses A and E are included in Appendices A and E.

Table 9-1 – RMS Pointing and Focus Errors for Correlated and Uncorrelated Forces on M2

	Analysis A Correlated Forces on M2	Analysis E Uncorrelated Forces on M2
	RMS Pointing Error X Direction (arcsec)	
Minimum	0.206	0.207
Maximum	0.217	0.217
Weighted Mean	0.198	0.199
	RMS Pointing Error Y Direction (arcsec)	
Minimum	0.455	0.455
Maximum	0.475	0.474
Weighted Mean	0.459	0.458
	RMS Focus Error Z Direction (mm)	
Minimum	0.205	0.187
Maximum	0.338	0.326
Weighted Mean	0.250	0.235

These results show that there is only a small difference in RMS pointing errors in the x- and y-directions for the correlated and uncorrelated cases. The RMS focus error is slightly larger for the correlated case. Therefore, the difference between the correlated and uncorrelated cases is not significant relative to other factors that contribute to the pointing errors. The correlated case

was chosen to be the default case for all other analyses since it gives slightly conservative results.

9.2 Effect of M1 Mirror Loading Method

We examined two methods of loading the M1 mirrors: Method 1 – force and moment method, and Method 2 – pressure zone method. These methods are described in the dynamic wind load section. We performed random response analyses using one of the secondary truss stiffening options (Option 1) and locked rotor condition with 2% damping and Case 1 (vent gates open and wind screen open).

The RMS pointing and focus errors from 0.1 Hz to 25 Hz for the two methods of M1 mirror loading are summarized in Table 9-2. The detailed results for Analyses F and J are included in Appendices F and J.

Table 9-2 – RMS Pointing and Focus Errors for Two Methods of M1 Mirror Loading

	Analysis F Force and Moment on M1	**Analysis J Large Pressure Zone on M1**
	RMS Pointing Error X Direction (arcsec)	
Minimum	0.159	0.151
Maximum	0.189	0.182
Weighted Mean	0.153	0.152
	RMS Pointing Error Y Direction (arcsec)	
Minimum	0.364	0.360
Maximum	0.384	0.381
Weighted Mean	0.368	0.367
	RMS Focus Error Z Direction (mm)	
Minimum	0.197	0.173
Maximum	0.359	0.324
Weighted Mean	0.237	0.214

These results show that there is only a small difference in RMS pointing errors in the x- and y-directions for the two methods. The RMS focus error is slightly larger for the force and moment method. Therefore, the difference between the two methods of M1 mirror loading is not significant relative to other factors that contribute to the pointing errors. The force and moment method was chosen to be the default case for all other analyses, since it gives slightly conservative results.

10. DISCUSSION

The goals of this study are to determine order of magnitude pointing and focus errors resulting from wind disturbance on the GMT structure and to identify possible modifications to the structure to improve the optical performance.

In this study, we elected to use the wind data recorded at Gemini South because this test contains one of the most comprehensive pressure and velocity measurements on an actual telescope structure. The time history records and the power spectral density curves are available for a variety of cases. We calculated the dynamic wind loads on the GMT structure by adjusting and adapting the pressure and velocity measurements at Gemini South.

However, if more accurate results are needed, there are some limitations in using this approach:

- The shape of the Gemini enclosure is different from the carousel-type enclosure currently envisioned for GMT. The arrangements of the shutters and vents for the two enclosures are not the same. The wind flow around and through the two enclosures will be different.
- The Gemini South Telescope has a single 8 m optical mirror and the GMT will have seven 8.4 m mirrors. The two telescope structures and secondary support trusses do not share a lot of similarities. The wind flow around the two telescope structures are not the same.
- Almost all the wind measurements at Gemini South were performed with the wind screen open. This may not be the typical observation mode. By using the wind measurement with the wind screen open, the wind loads calculated for the secondary mirrors, the secondary support structure, and secondary truss may be too conservative.

For the preliminary and final design phases, wind tunnel tests or computational fluid dynamic analyses for the GMT enclosure and telescope structure are needed to better define the wind disturbance on the GMT structure.

Damping also has a significant effect on the dynamic response in the telescope structure. Cares must be taken to ensure telescope structure is properly damped.

In this study, although we calculated the encoder readings resulting from the wind disturbance, we did not considered the responses of the control system. The wind vibration analysis should be integrated with control system analysis and design so that end-to-end analysis or integrated structural-optical-control analysis can be performed.

In this study, we identified areas in the structure that need improvement and evaluated several stiffening options. However, we did not perform a full optimization of the entire telescope structure given the current stage of the telescope design and the accuracy of the wind loads discussed above. As the telescope design matures, we recommend performing optimization of the structure when more accurate definition of the wind disturbances on the telescope structure is available.

11. REFERENCES

[1] Johns, Matthew W., “Giant Magellan Telescope Design Requirements Document”, Revision 1.8, 23 Apr. 2005.

[2] MACL Report #05-08570-001, “Gemini South 8m Optical Telescope, Final Report”, Modal Analysis and Controls Laboratory, Mechanical Engineering Department, University of Massachusetts at Lowell, Lowell, MA, Oct. 2000.

[3] http://www.aura-nio.noao.edu/studies/smith0208/tests/index.html

[4] National Research Council of Canada (NRC-CNRC), *User’s Guide to National Building Code 1995 Structural Commentaries (Part 4),* 1st edition, 1996.

[5] Johns, Matthew W., “Optical Sensitivity Equations for use in the Dynamical Response Analysis for the Giant Magellan Telescope”, 10 June 2005.

O:\DATEFILE\2005\Kan\FWK16-R-nl.doc

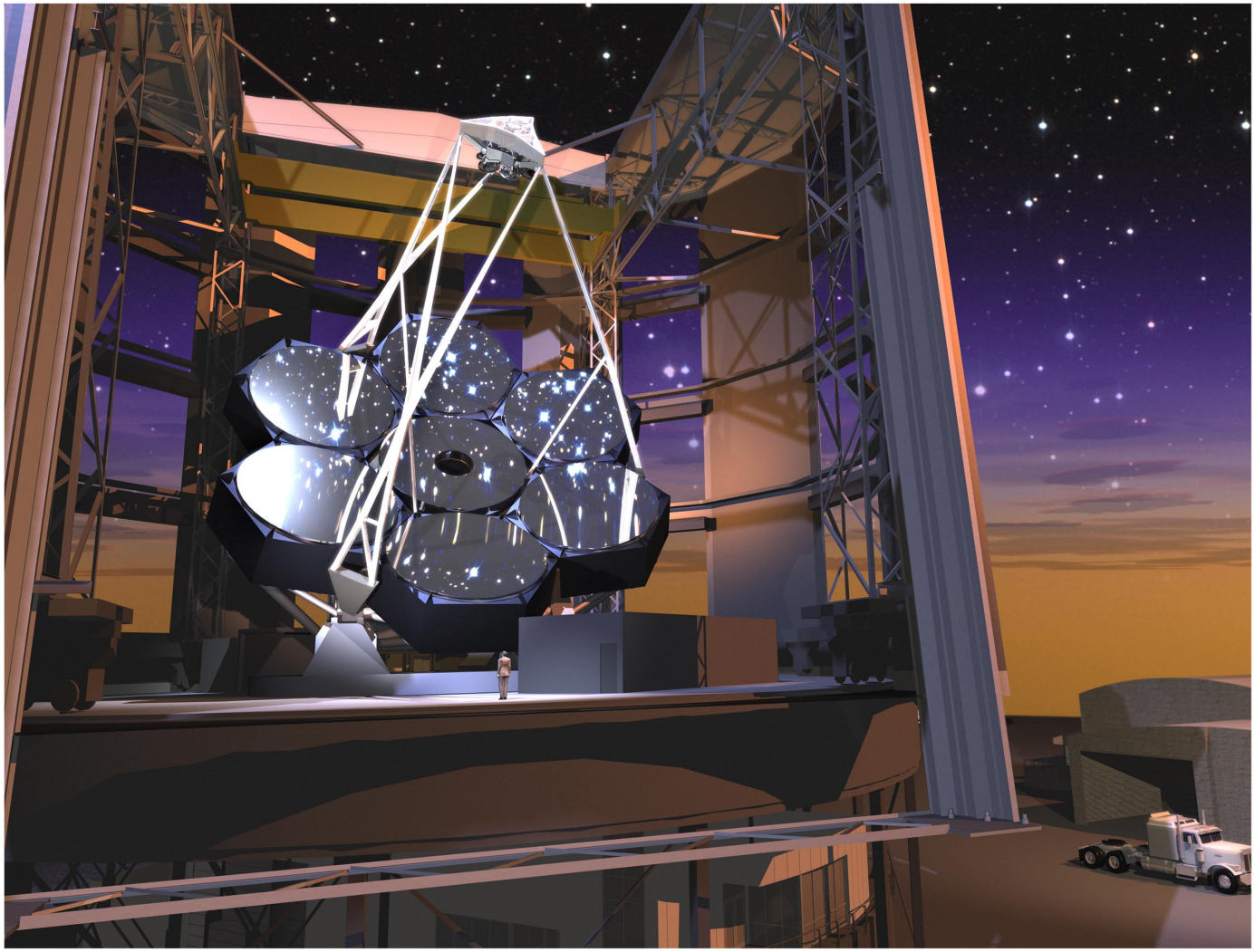

Figure 1-1 – Rendering of GMT and Enclosure

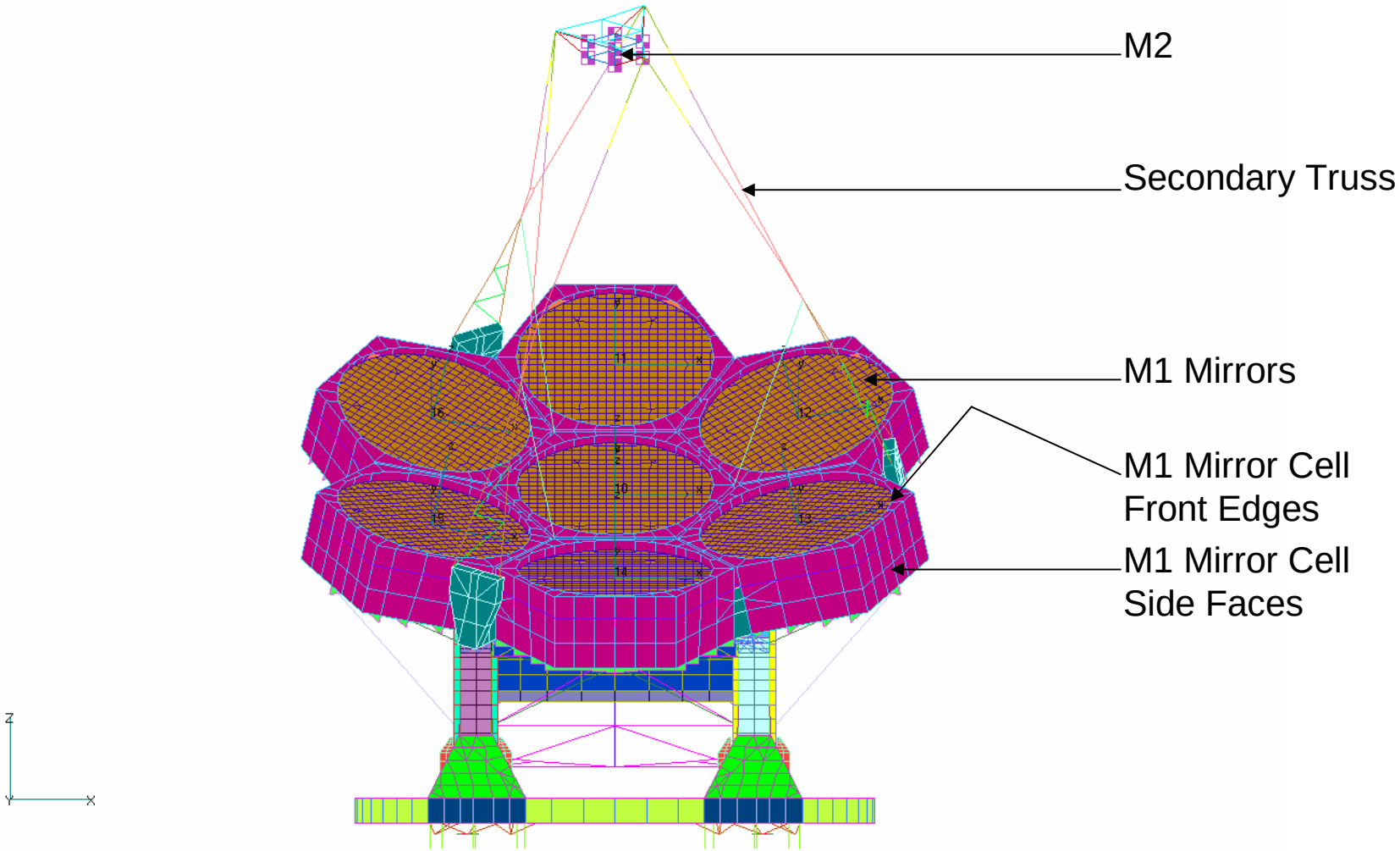

Figure 2-1 – Front View of Finite Element Model

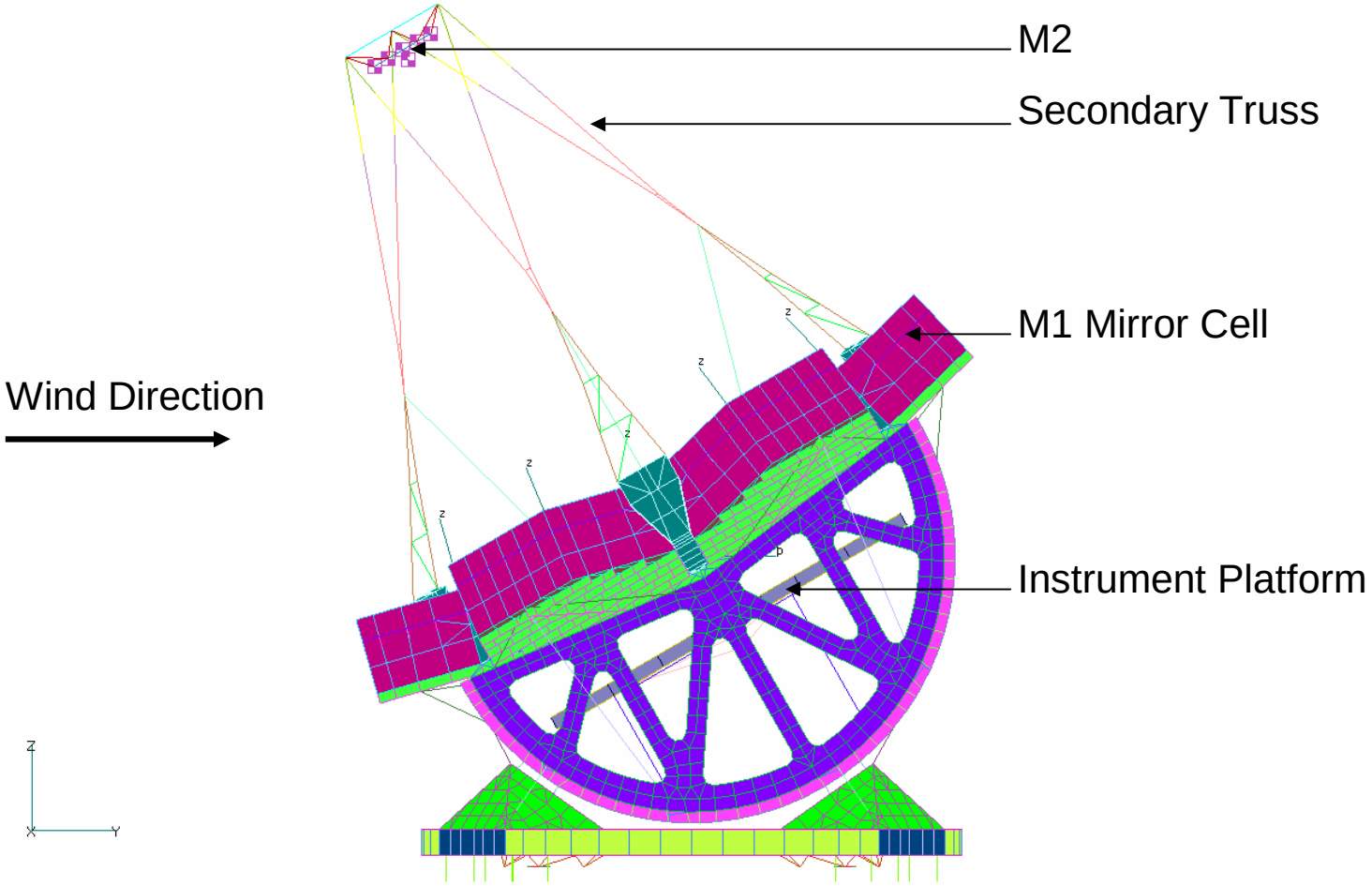

Figure 2-2 – Side View of Finite Element Model

The local mirror coordinate systems (x', y', z'): local z' is perpendicular to the mirror plane; local x' and y' is in the OSS-fixed x-z and y-z planes respectively.

The OSS-fixed coordinate system (x, y, z) used for all optical sensitivity equations is aligned with the local mirror coordinate system of Mirror 7.

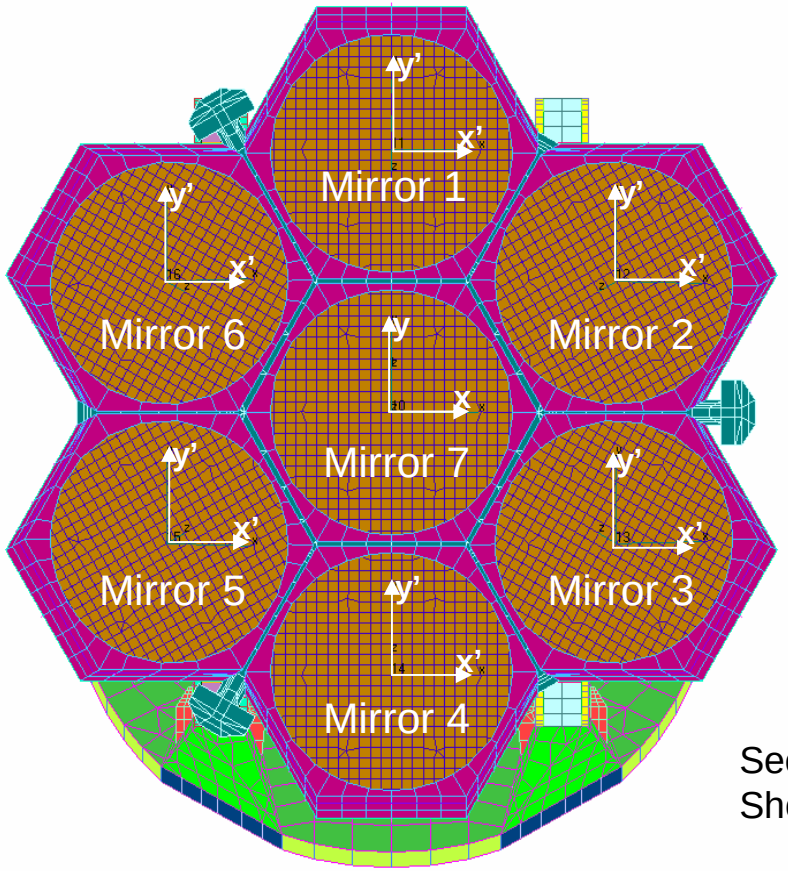

Global Coordinate System

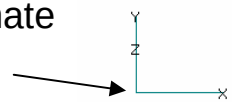

Secondary Truss and M2 Not Shown for Clarity

Figure 2-3 – View of FEM from M2 towards M1 showing Mirror Numbering and Coordinate Systems

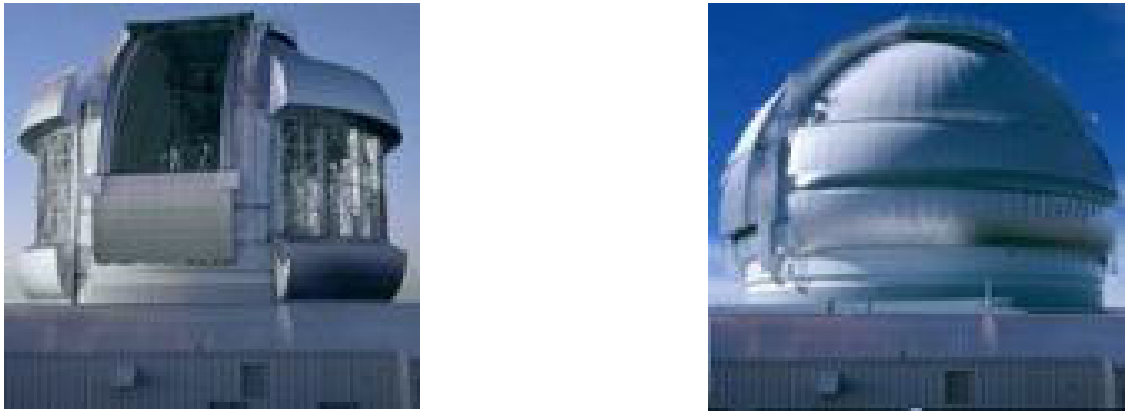

Figure 3-1 – Gemini South Telescope Enclosure, Vent Gates Closed (Left) and Vent Gates Open (Right)

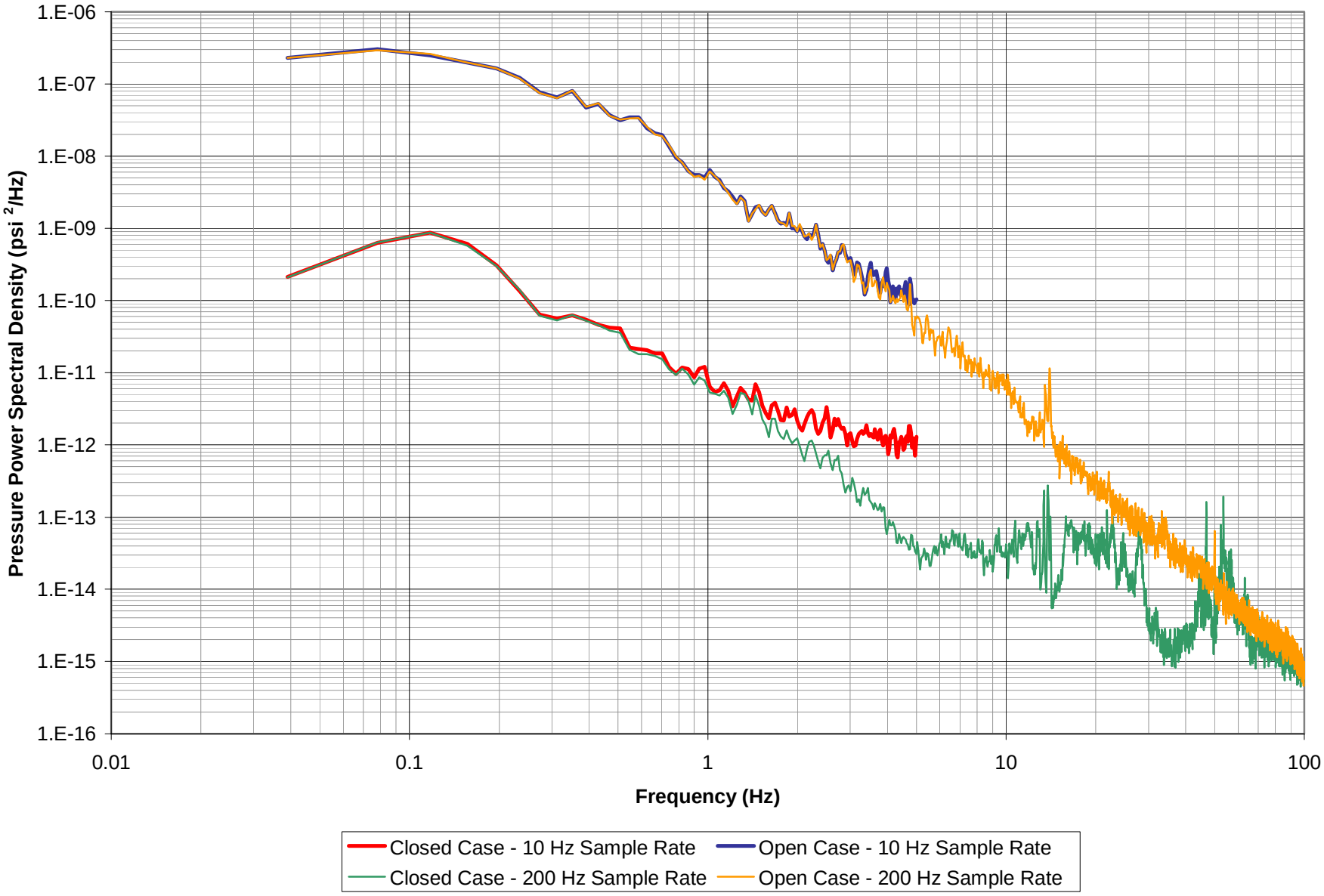

Figure 3-2 – Wind Pressure PSD at Pressure Tap 1 for Cases 1 and 2 with 10 Hz and 200 Hz Sampling Rate

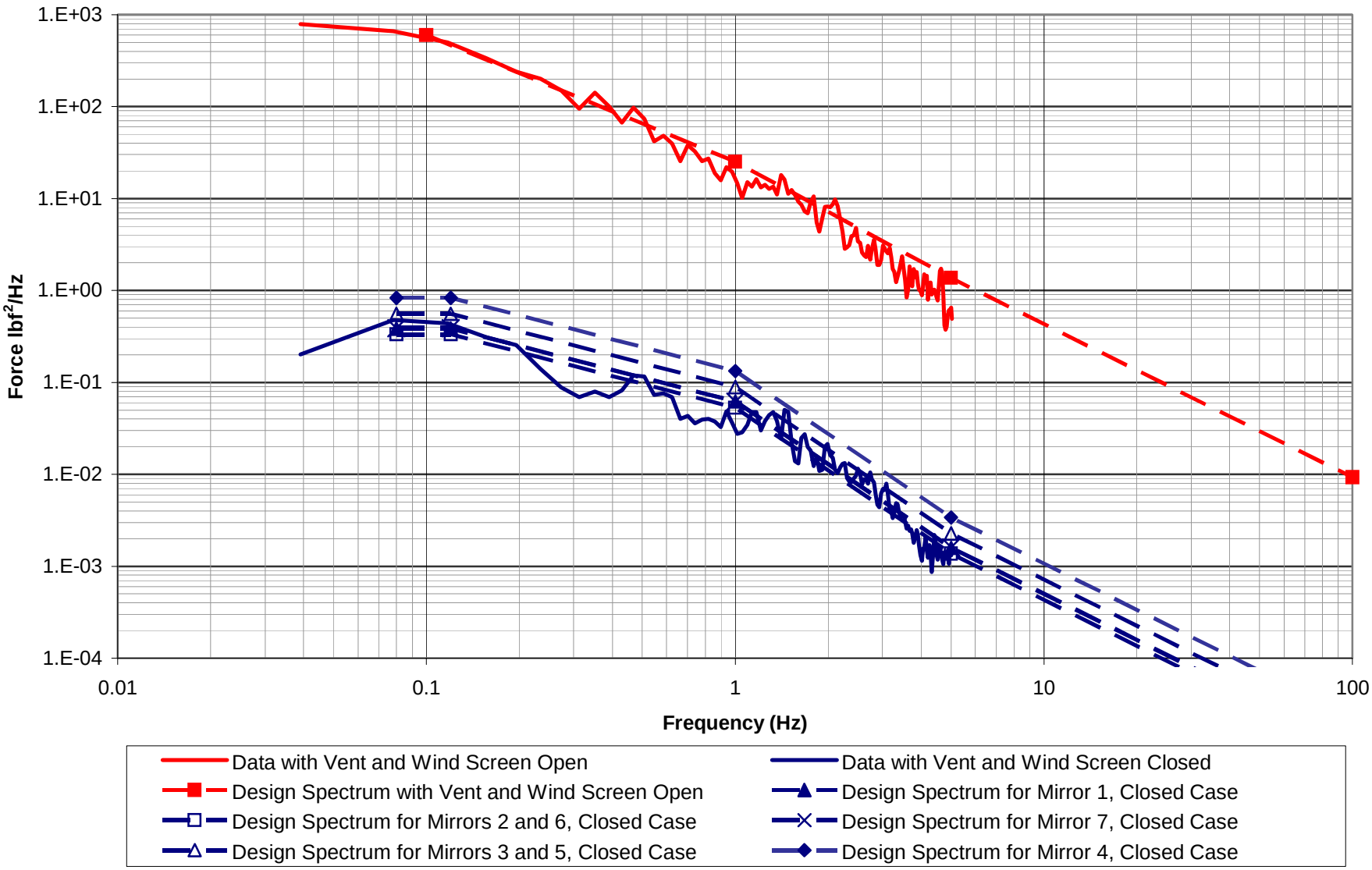

Figure 3-3 – M1 Force PSD for Cases 1 and 2

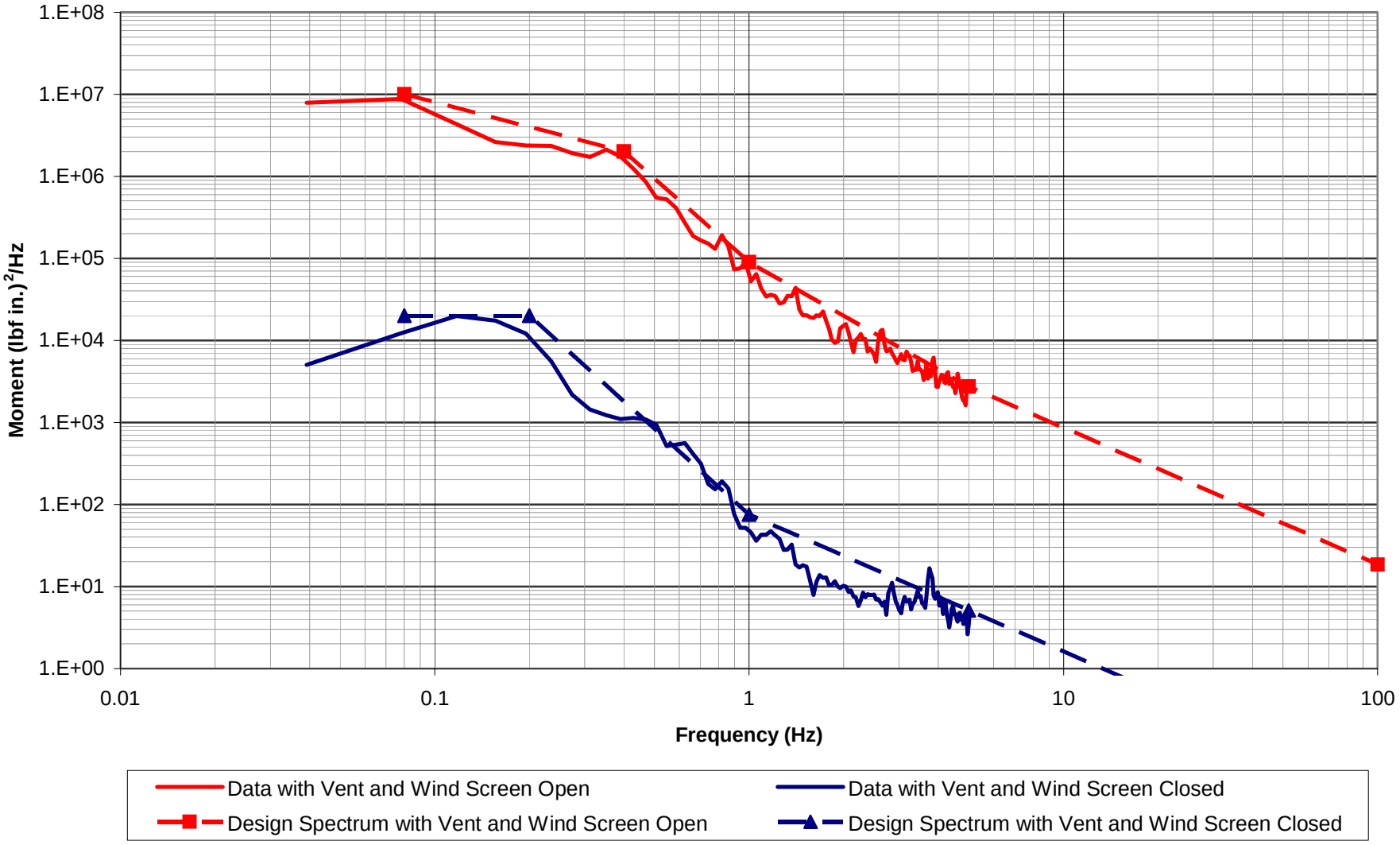

Figure 3-4 – M1 Moment about X-Axis PSD for Cases 1 and 2

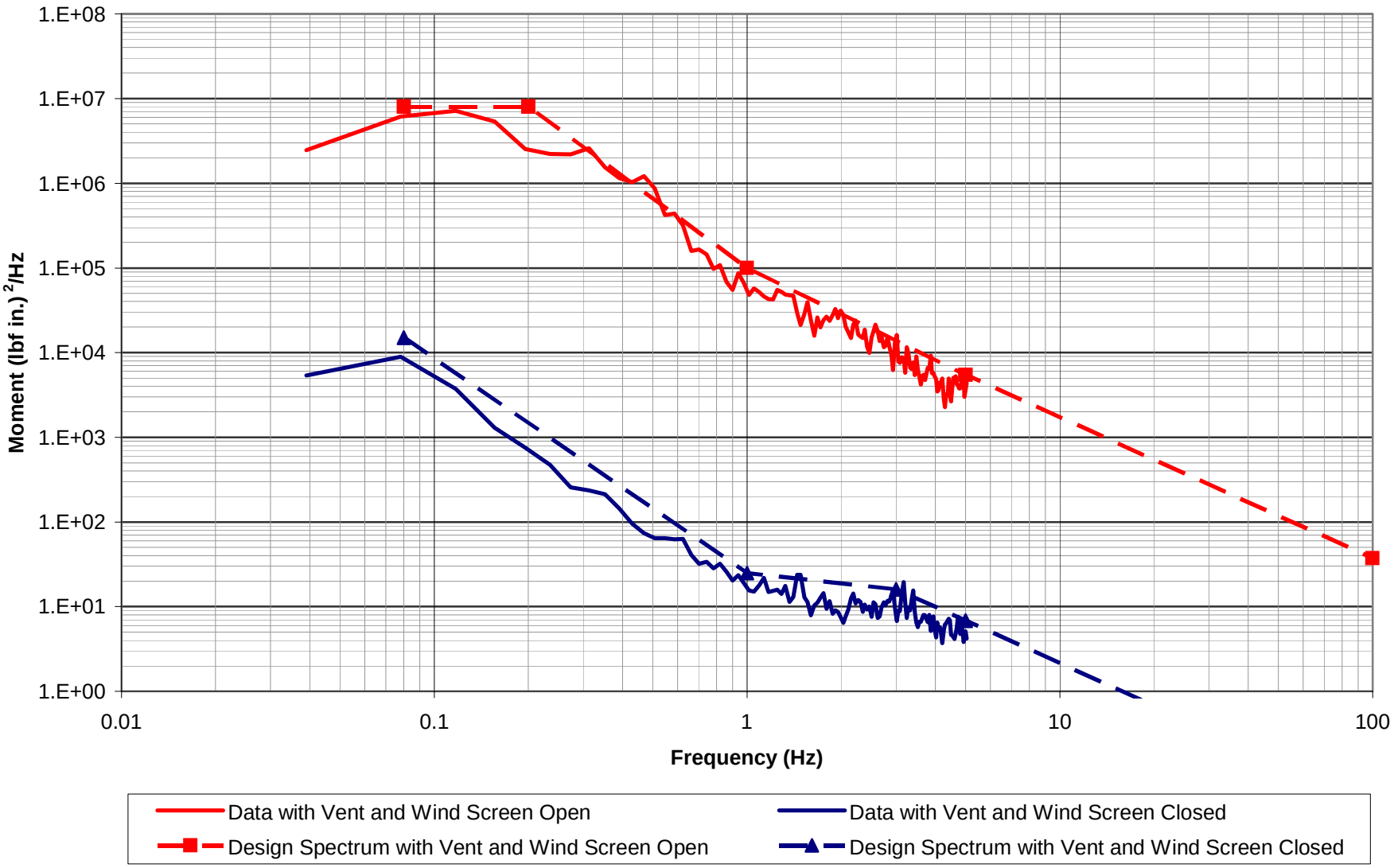

Figure 3-5 – M1 Moment about Y-Axis PSD for Cases 1 and 2

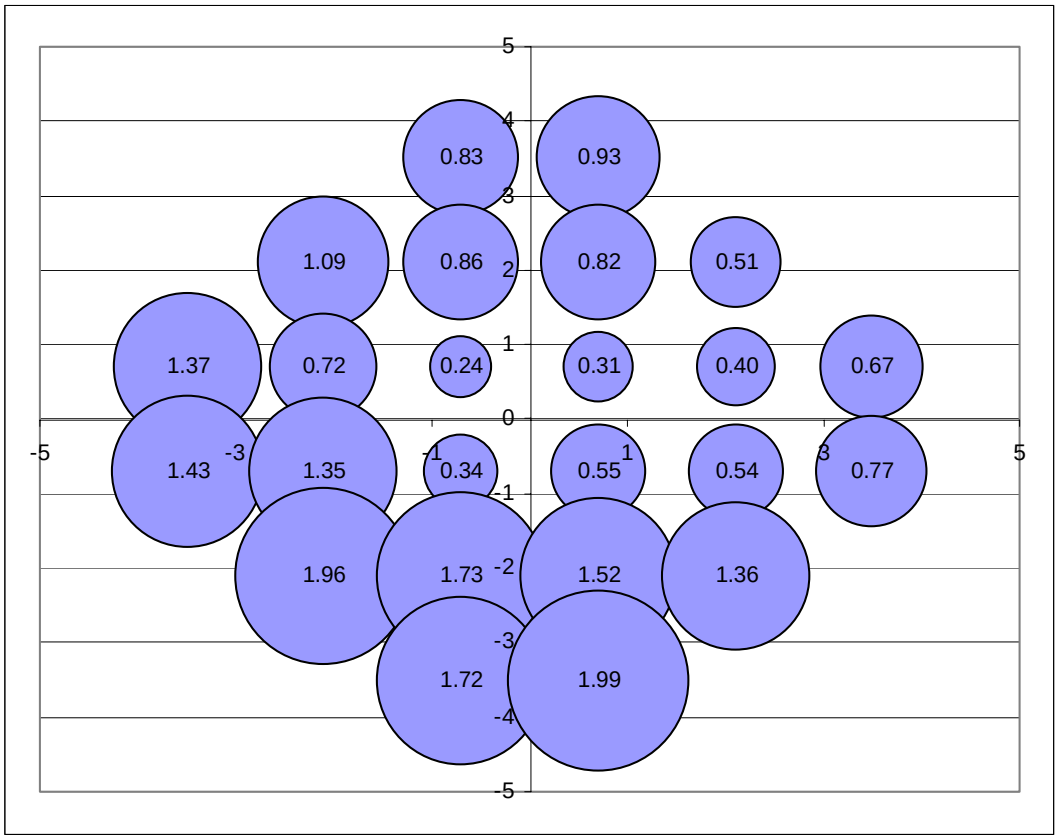

Figure 3-6 – Normalized Cumulative Wind Pressure Energy for Each Pressure Tap between 0.2 Hz and 2.0 Hz for Case 2

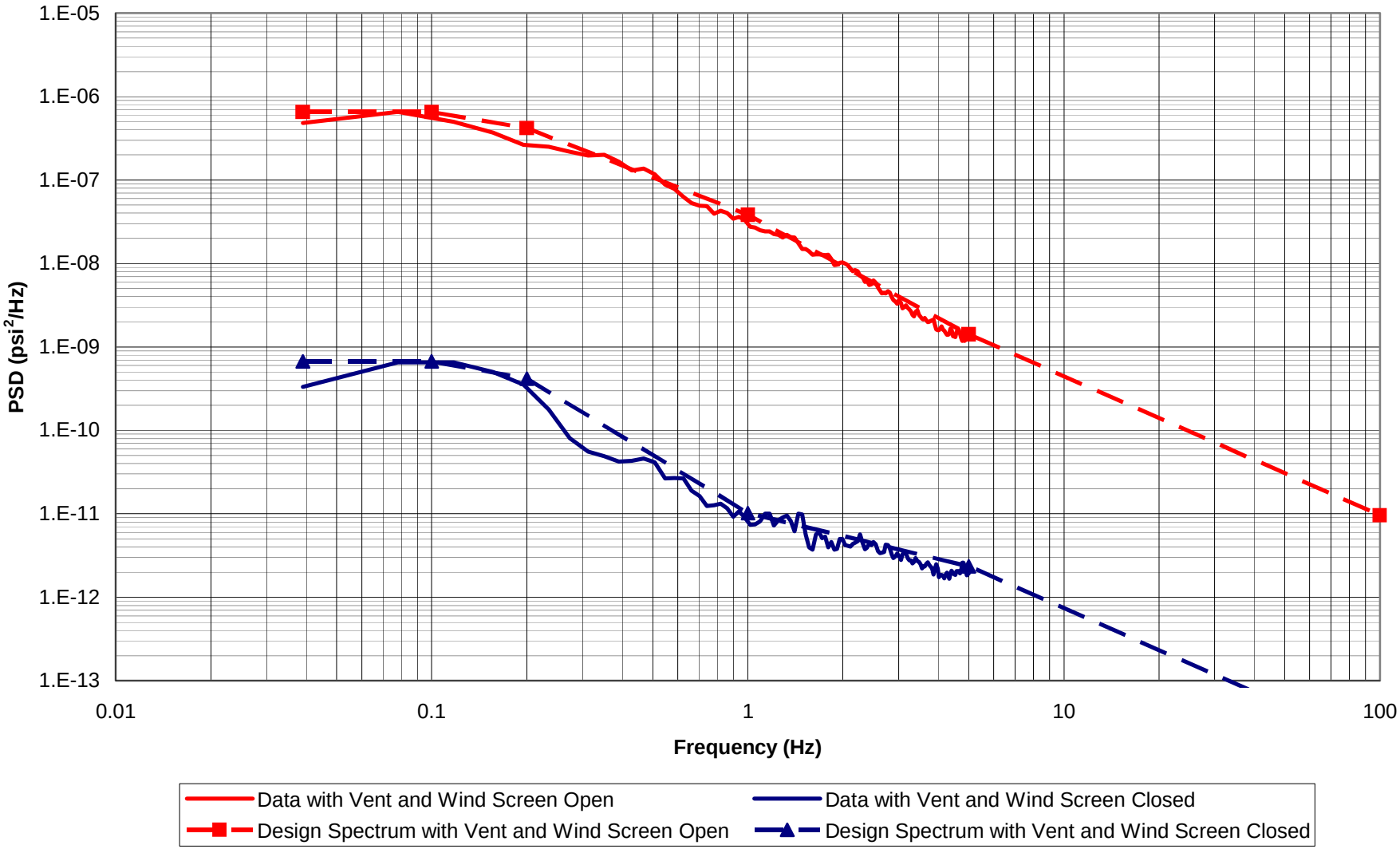

Figure 3-7 – Average M1 Pressure PSD for Cases 1 and 2

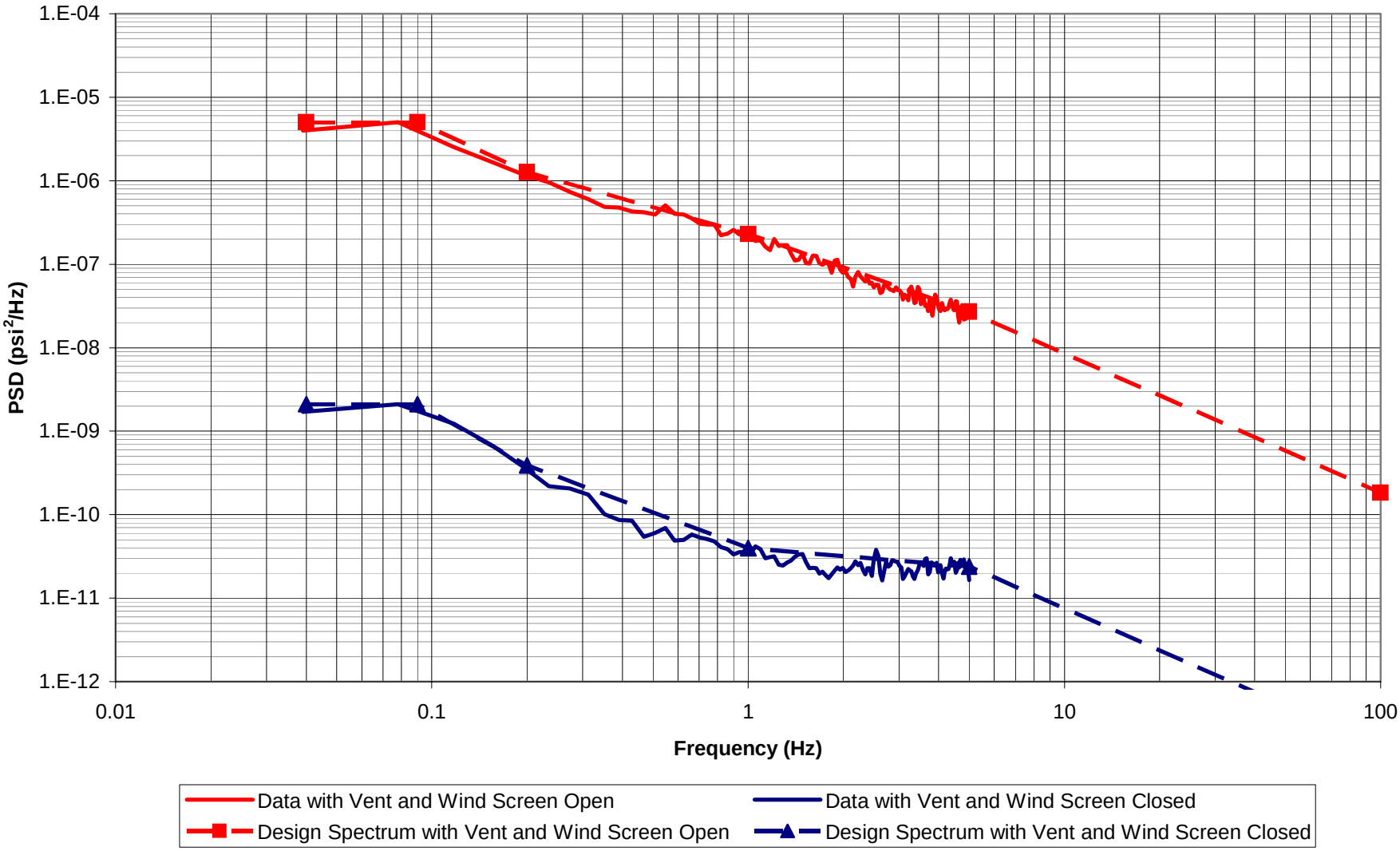

Figure 3-8 – Reference Pressure PSD Calculated from Velocity Measurements at M1 for Cases 1 and 2

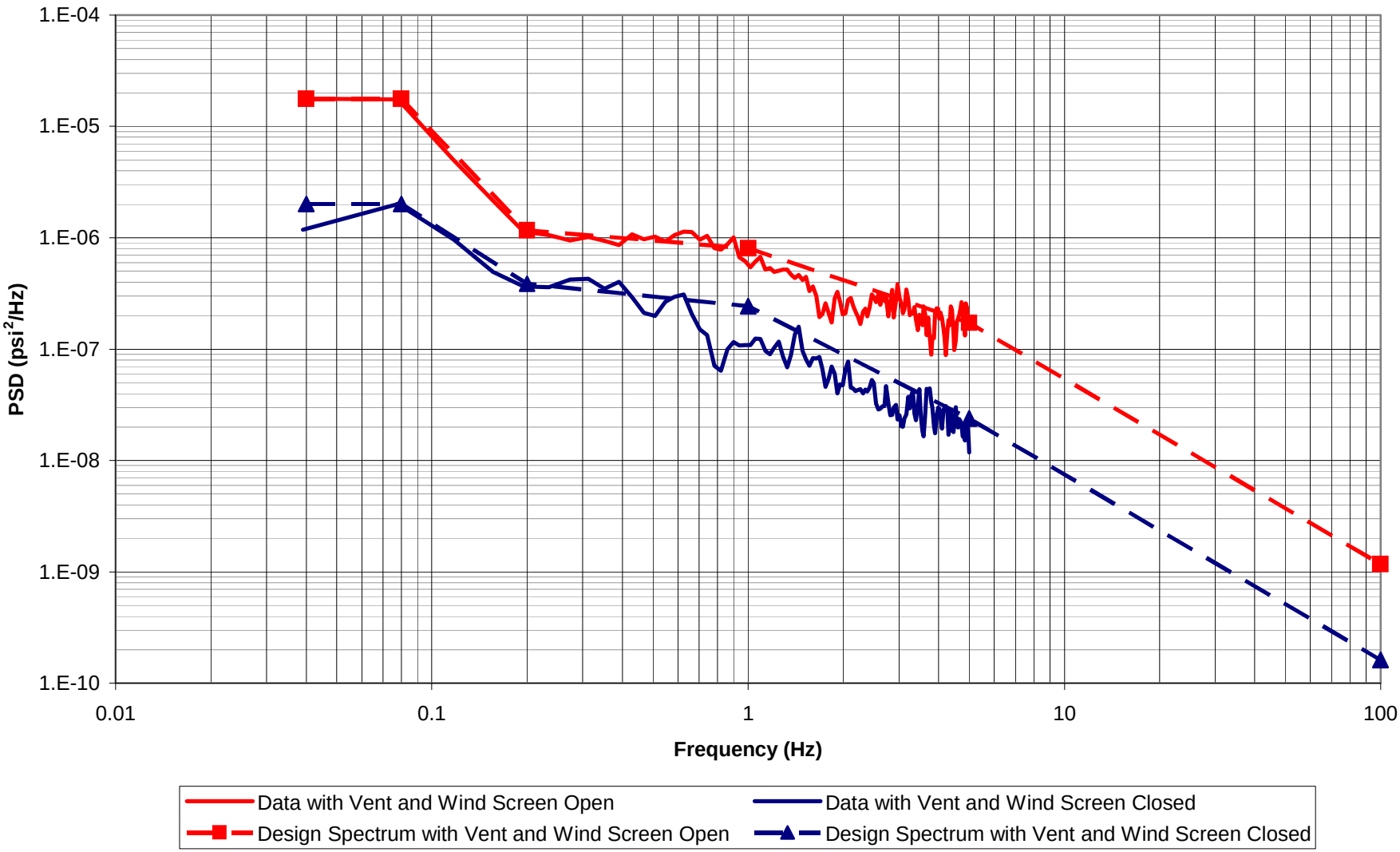

Figure 3-9 – Reference Pressure PSD Calculated from Velocity Measurements at M2 for Cases 1 and 2

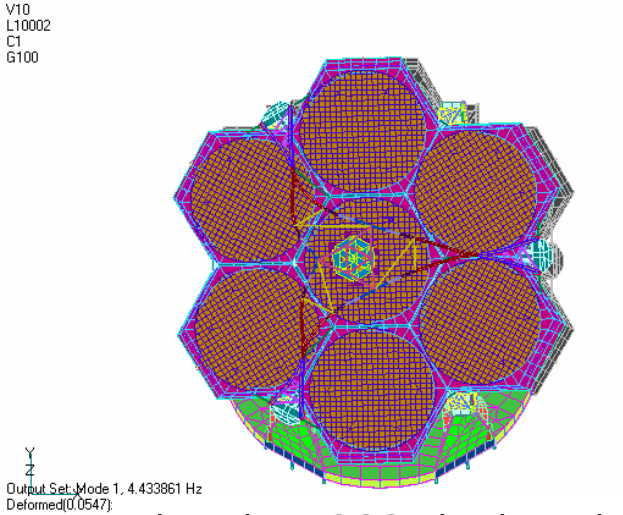

View along OSS-Fixed Z-Axis

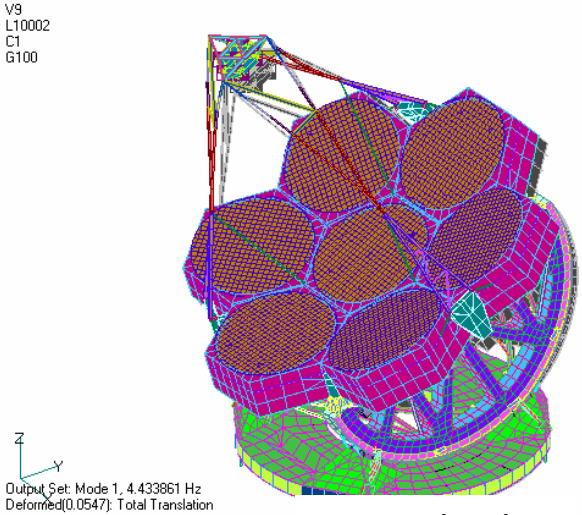

Isometric View

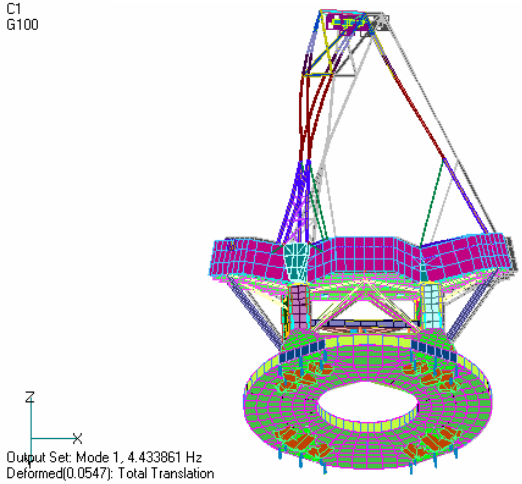

View along OSS-Fixed Y-Axis

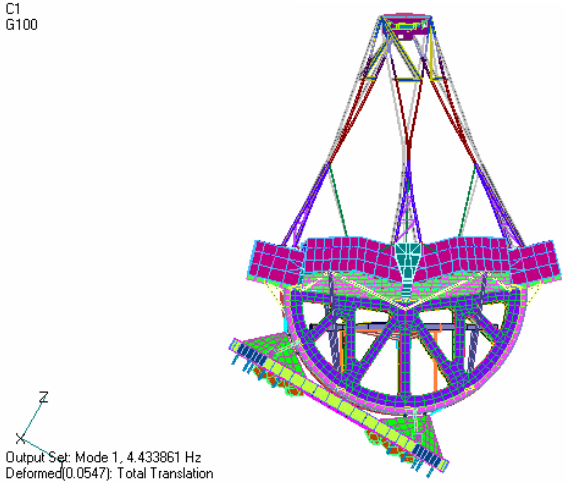

View along OSS-Fixed X-Axis

Figure 6-1 – Baseline Configuration, Locked Rotor, Mode 1, 4.43 Hz
Undeformed Model in Grey

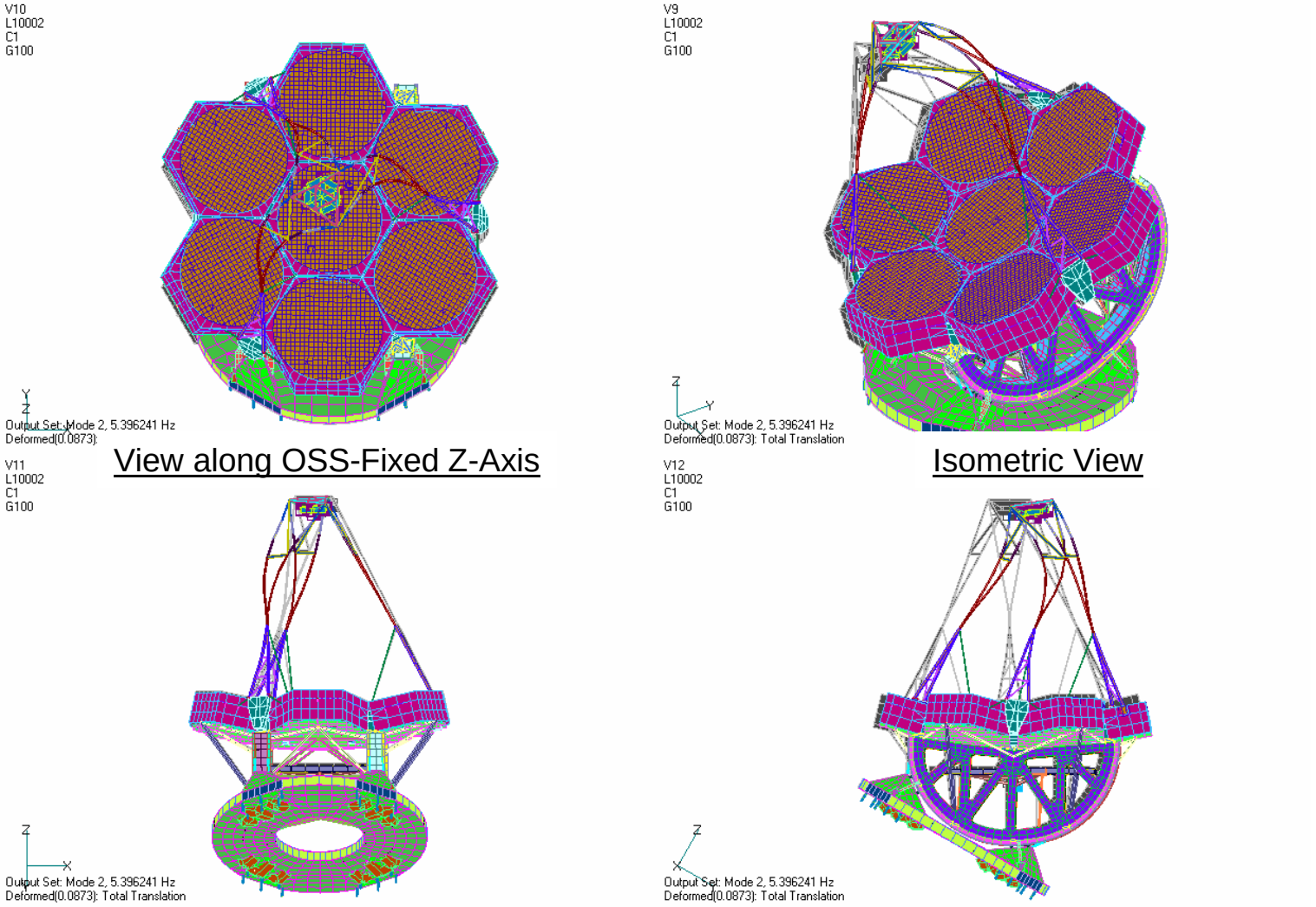

View along OSS-Fixed Z-Axis

Isometric View

View along OSS-Fixed Y-Axis

View along OSS-Fixed X-Axis

Figure 6-2 – Baseline Configuration, Locked Rotor, Mode 2, 5.40 Hz
Undeformed Model in Grey

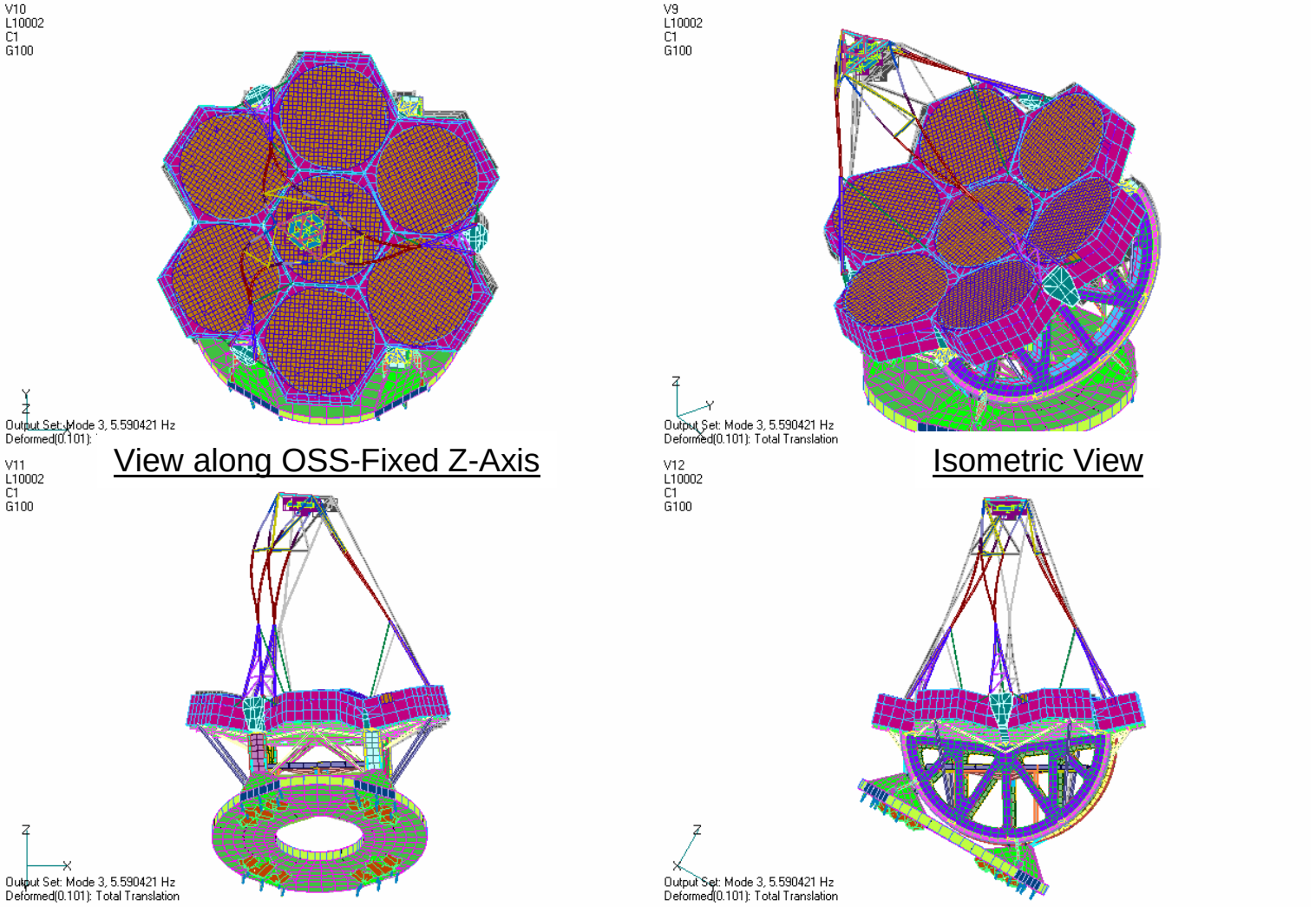

Figure 6-3 – Baseline Configuration, Locked Rotor, Mode 3, 5.59 Hz
Undeformed Model in Grey

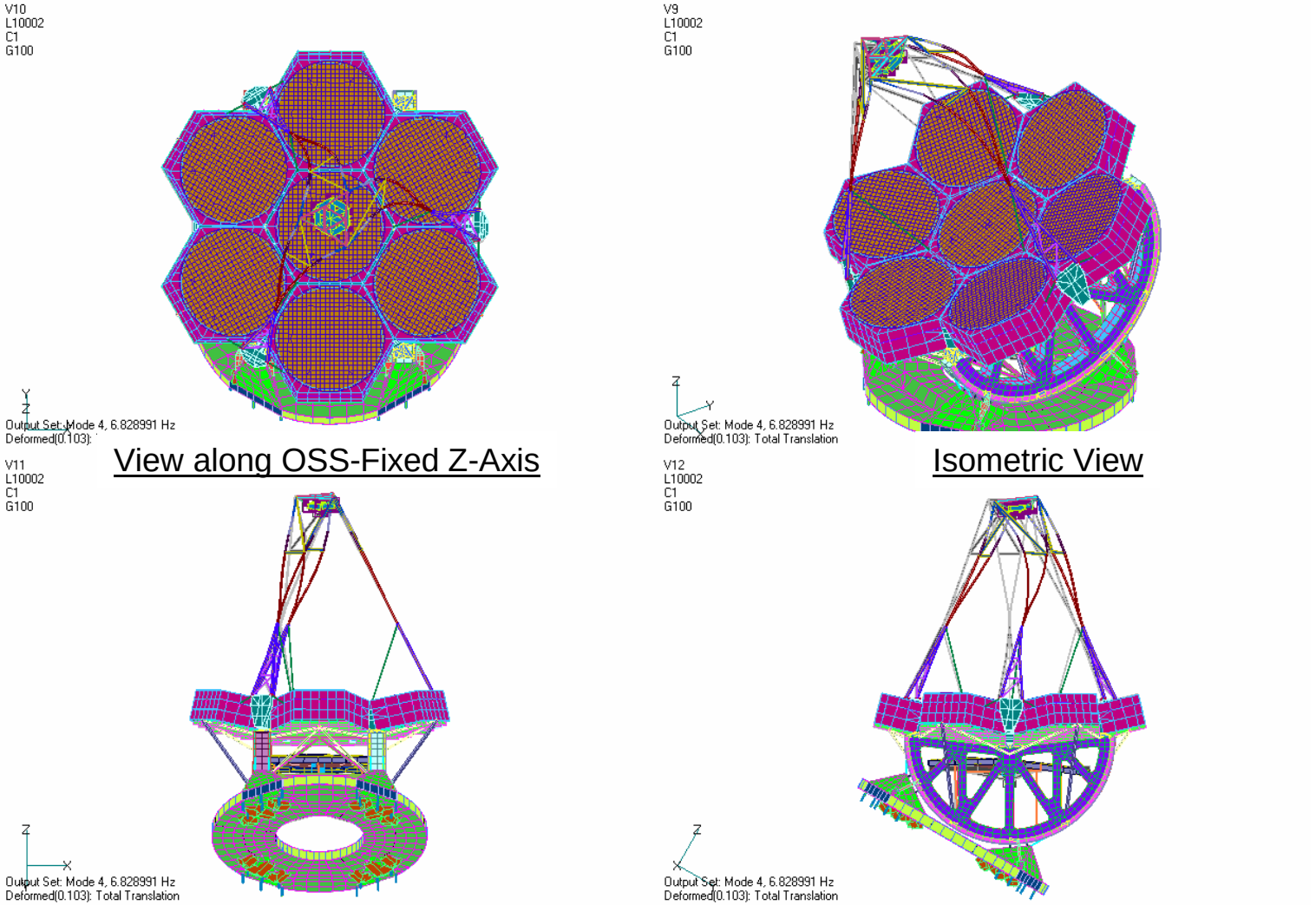

Figure 6-4 – Baseline Configuration, Locked Rotor, Mode 4, 6.83 Hz
Undeformed Model in Grey

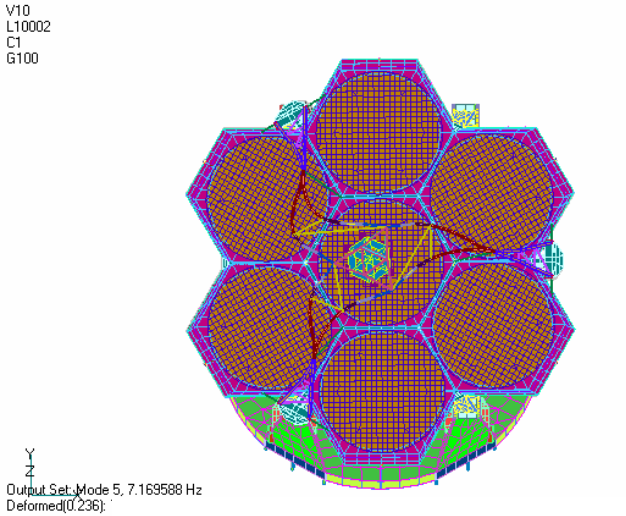

View along OSS-Fixed Z-Axis

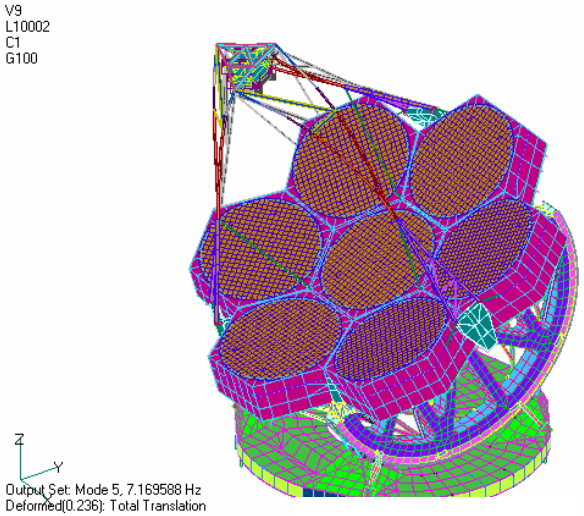

Isometric View

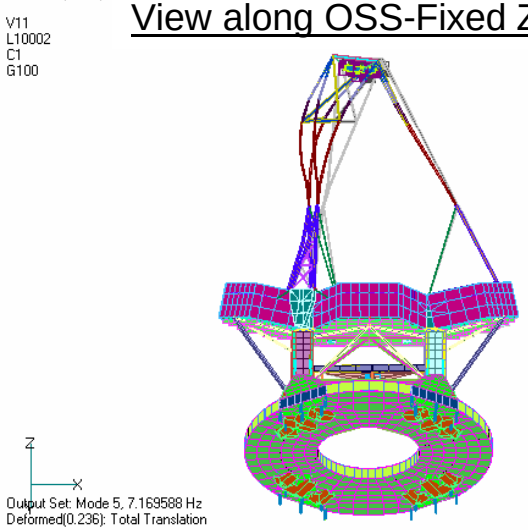

View along OSS-Fixed Y-Axis

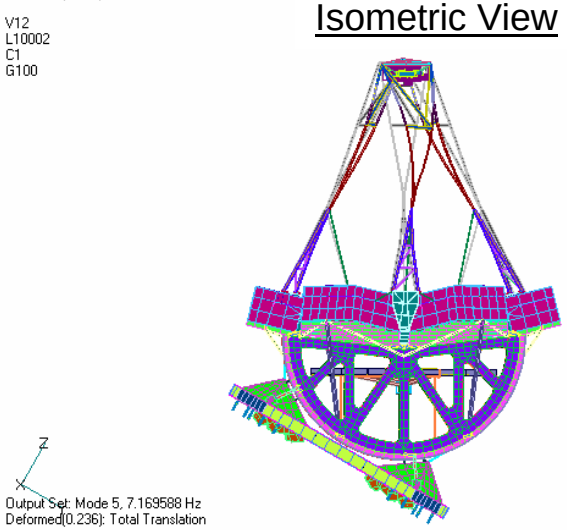

View along OSS-Fixed X-Axis

Figure 6-5 – Baseline Configuration, Locked Rotor, Mode 5, 7.17 Hz
Undeformed Model in Grey

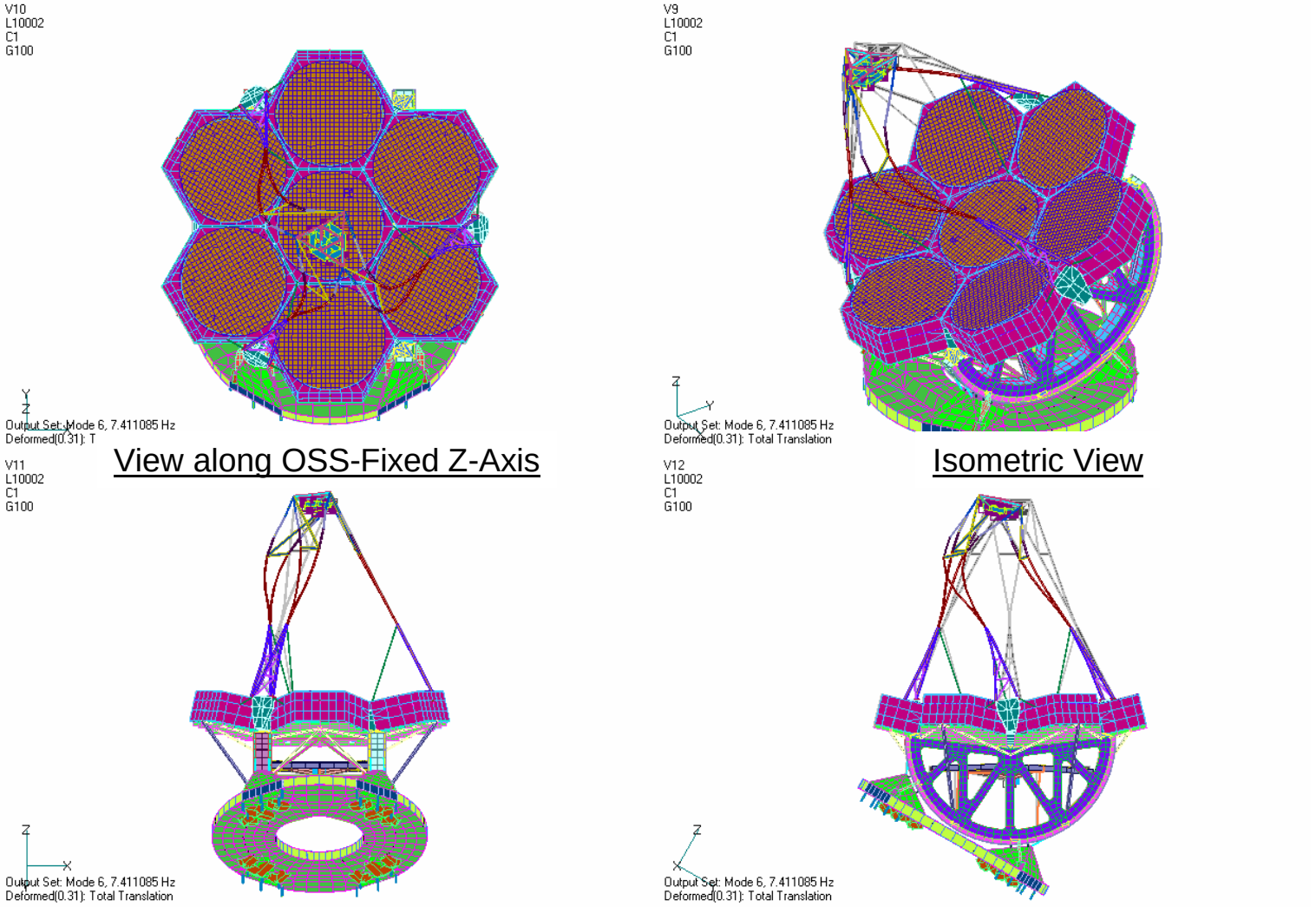

Figure 6-6 – Baseline Configuration, Locked Rotor, Mode 6, 7.41 Hz
Undeformed Model in Grey

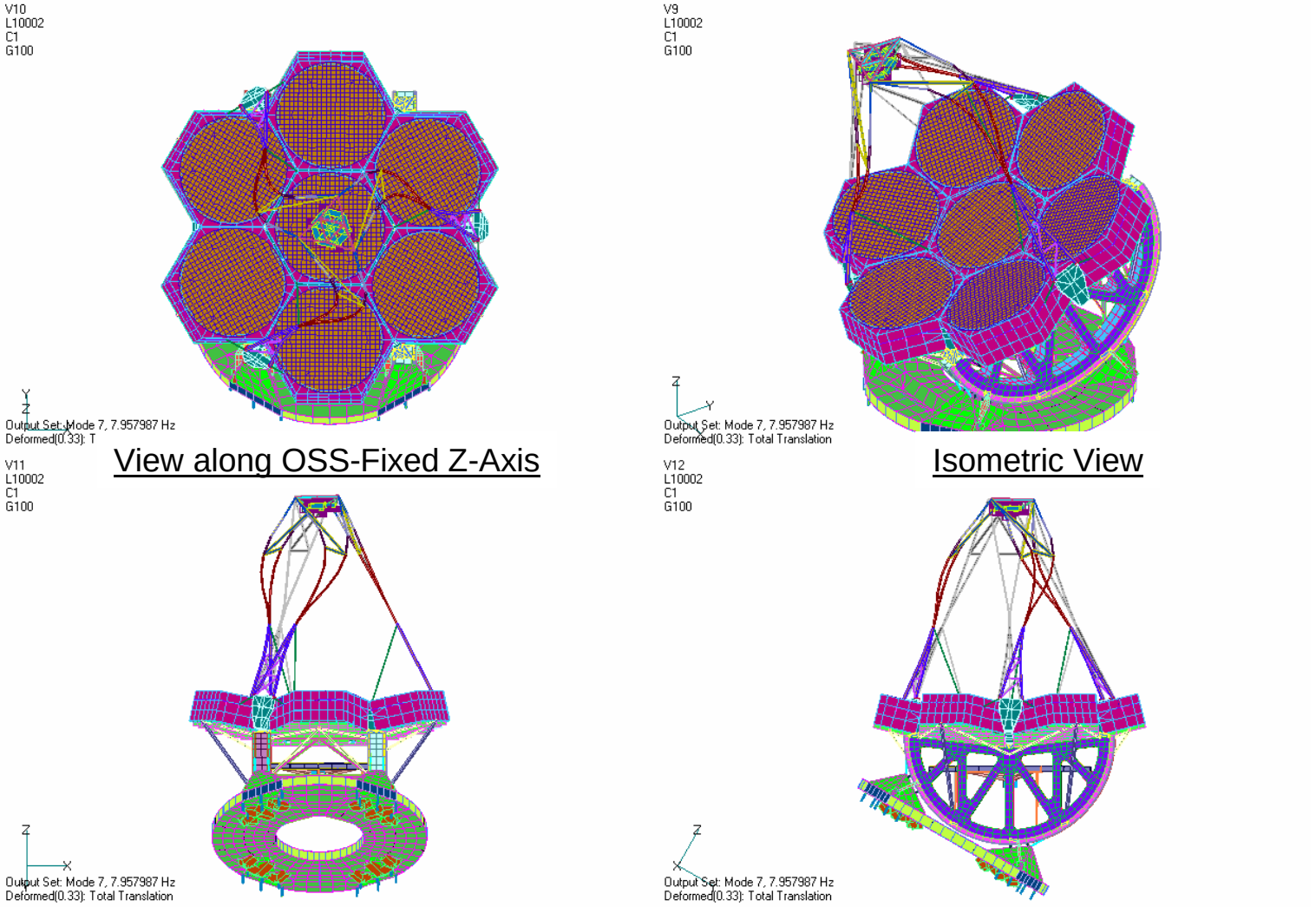

View along OSS-Fixed Z-Axis

Isometric View

View along OSS-Fixed Y-Axis

View along OSS-Fixed X-Axis

Figure 6-7 – Baseline Configuration, Locked Rotor, Mode 7, 7.96 Hz
Undeformed Model in Grey

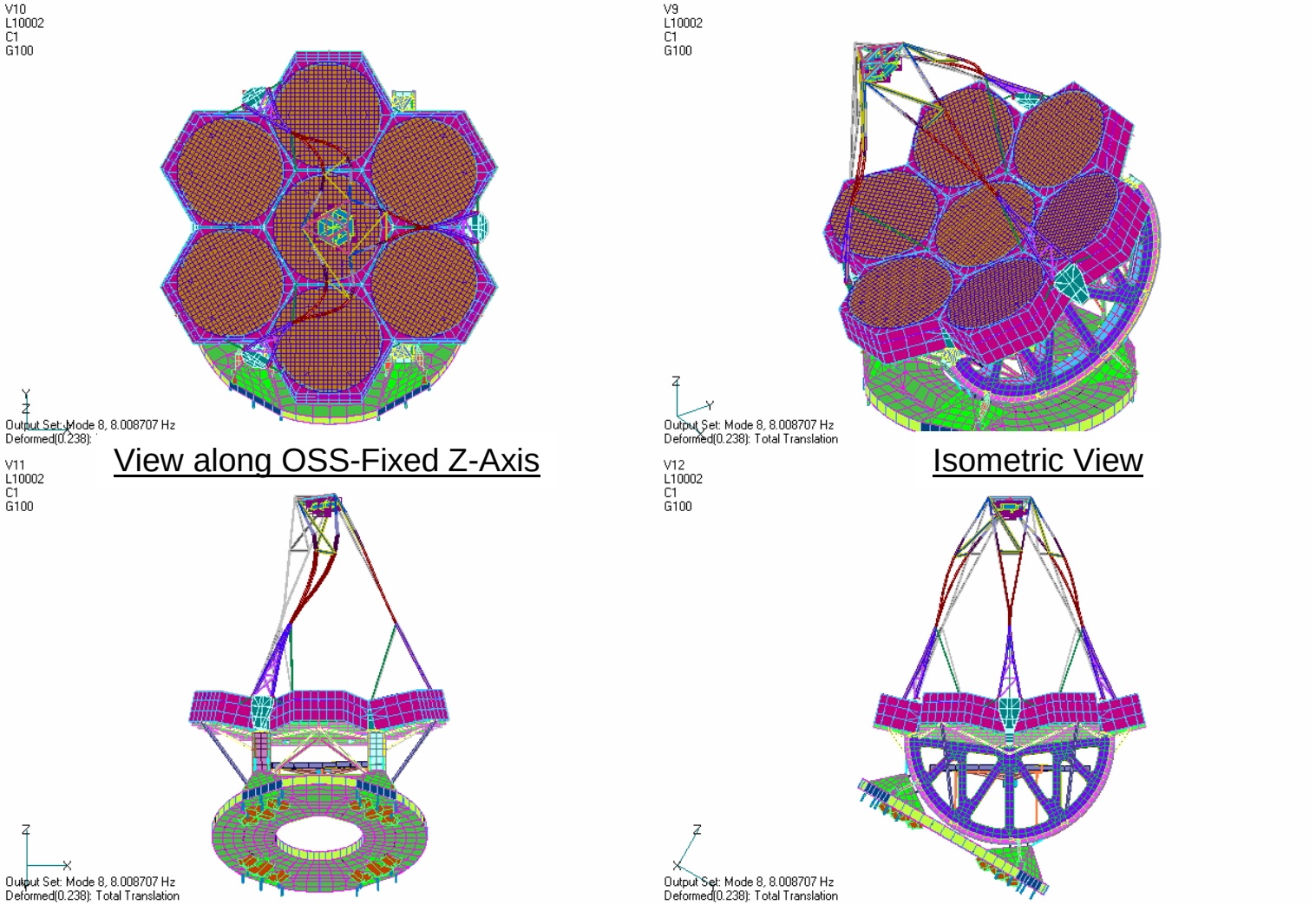

Figure 6-8 – Baseline Configuration, Locked Rotor, Mode 8, 8.01 Hz
Undeformed Model in Grey

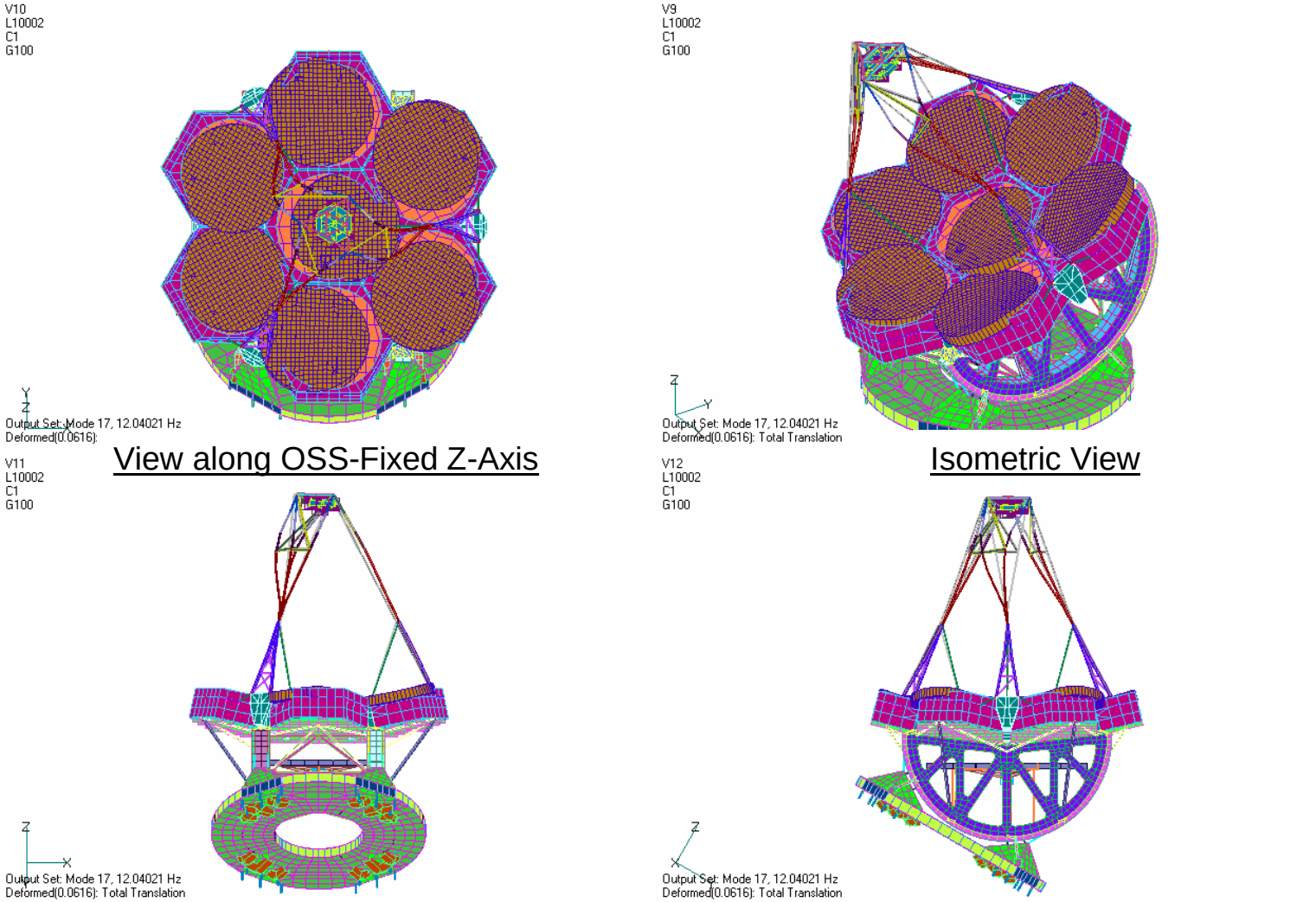

Figure 6-9 – Baseline Configuration, Locked Rotor, Mode 17, 12.04 Hz
Undeformed Model in Grey

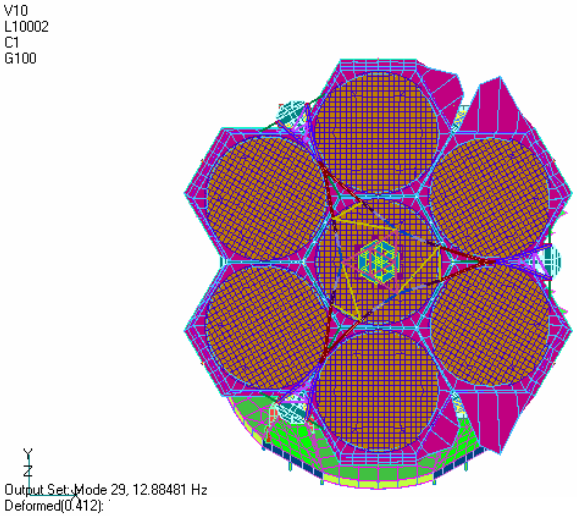

View along OSS-Fixed Z-Axis

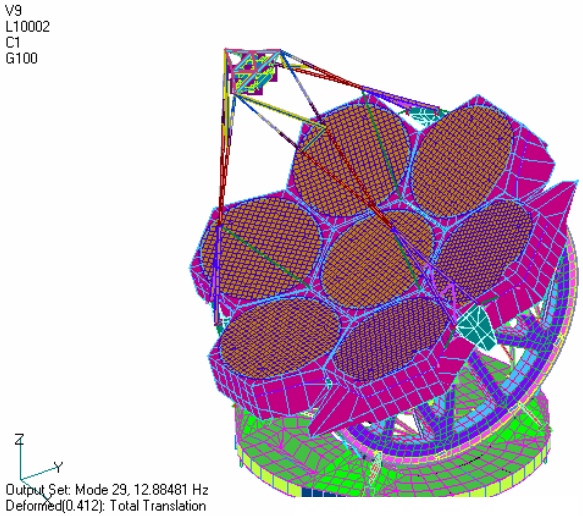

Isometric View

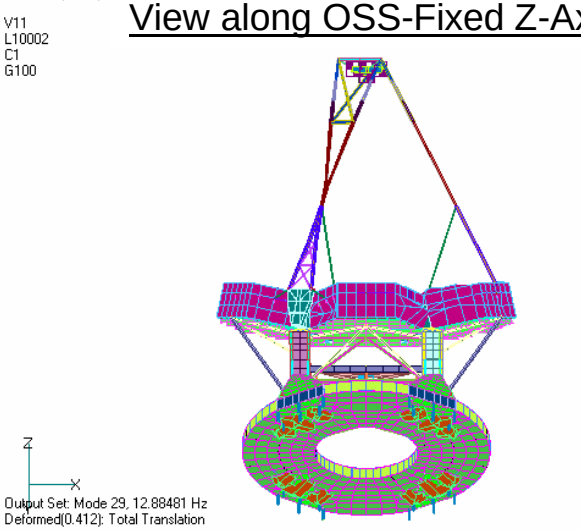

View along OSS-Fixed Y-Axis

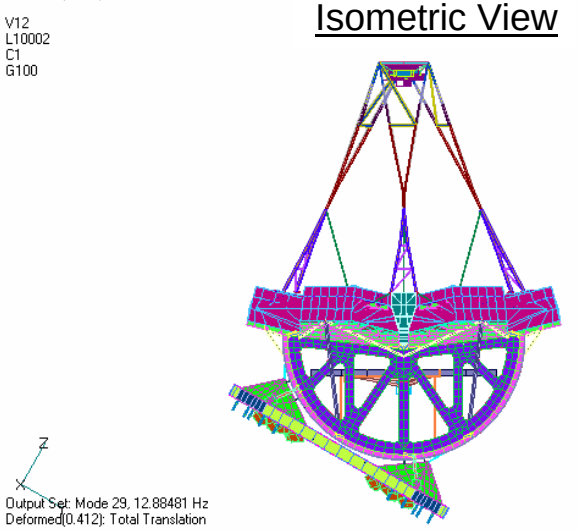

View along OSS-Fixed X-Axis

Figure 6-10 – Baseline Configuration, Locked Rotor, Mode 29, 12.88 Hz
Undeformed Model in Grey

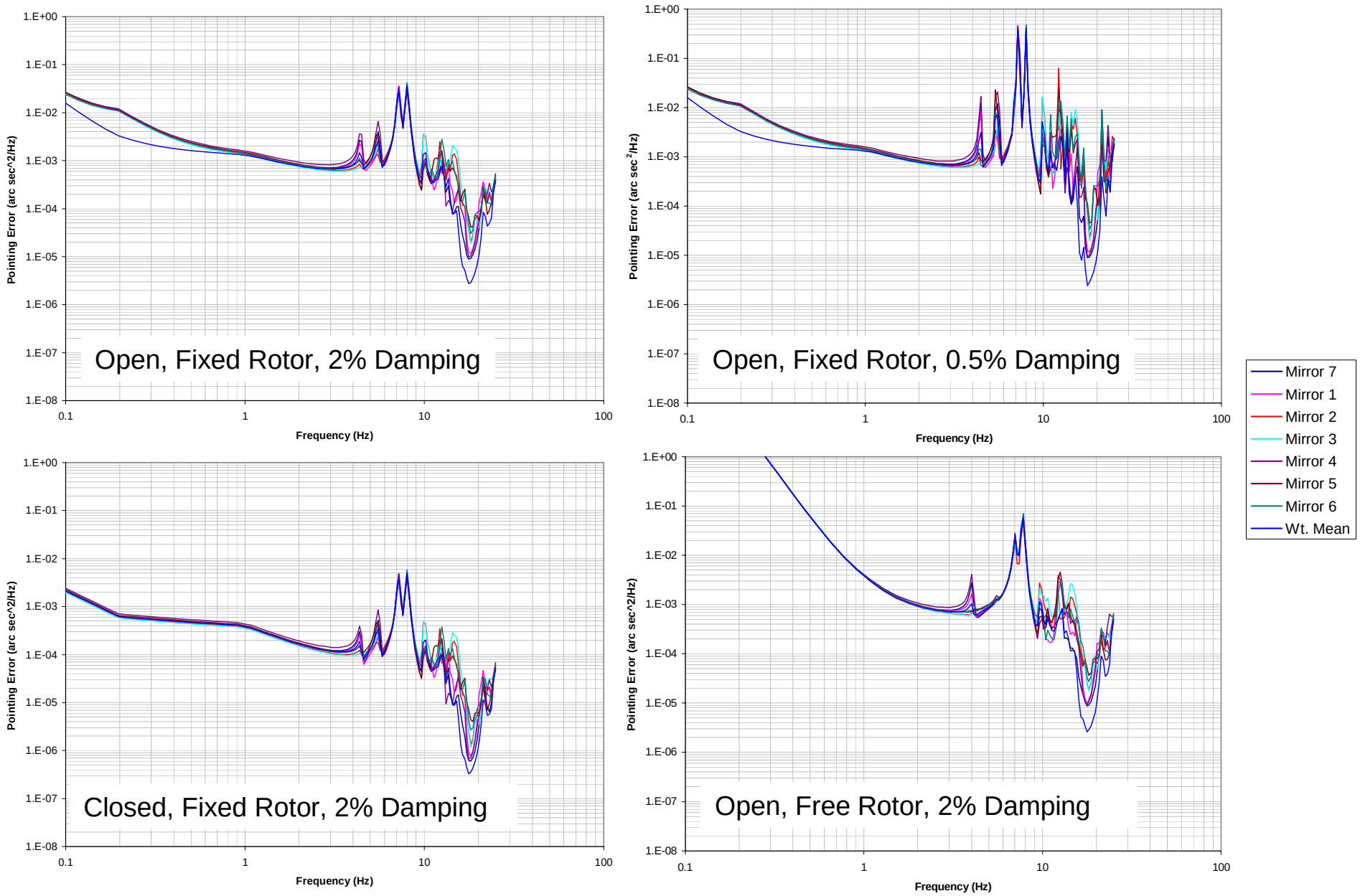

Figure 6-11 – Baseline Configuration, PSD of Pointing Error in X-Direction

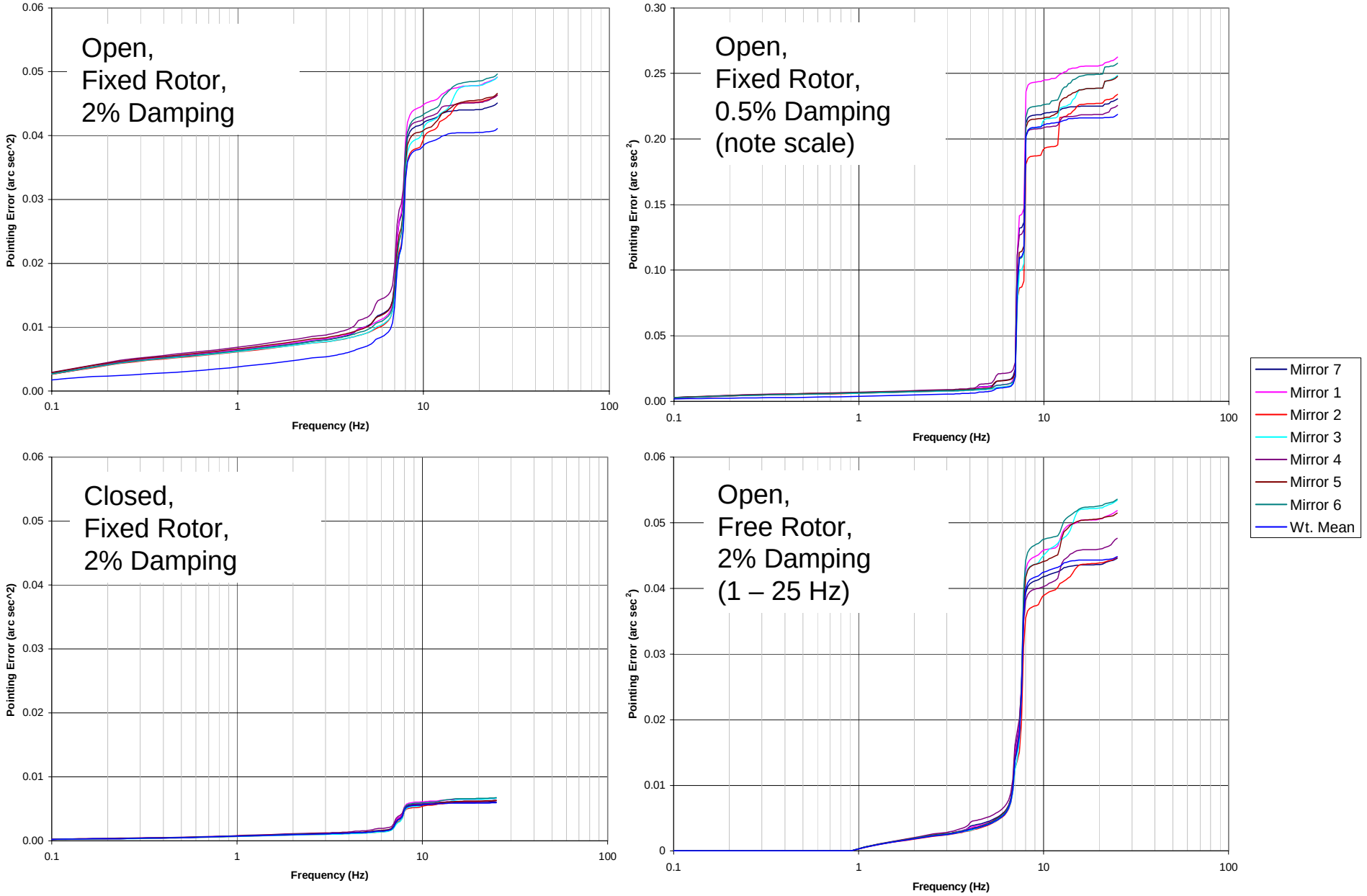

Figure 6-12 – Baseline Configuration, Cumulative Pointing Error in X-Direction

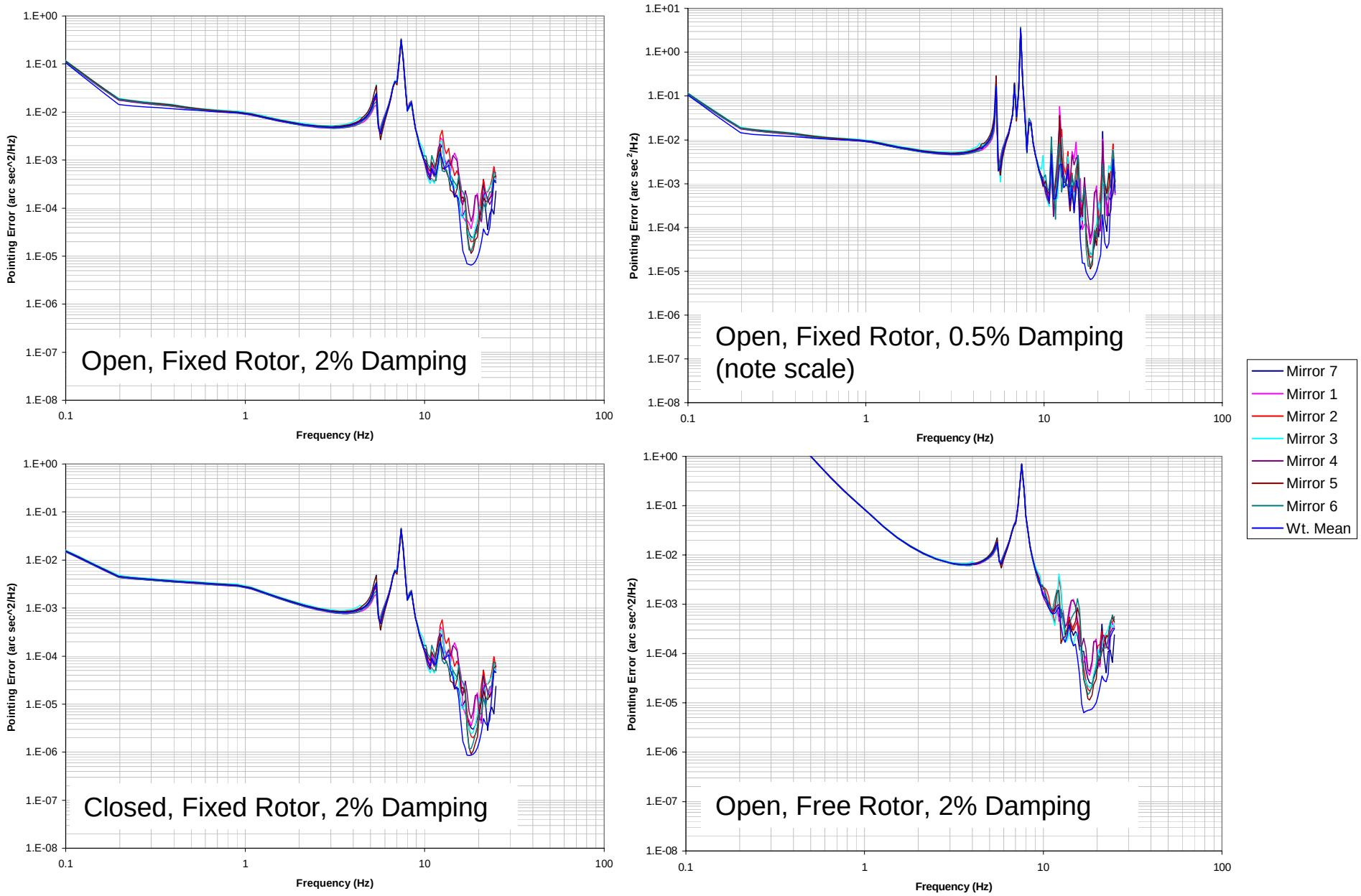

Figure 6-13 – Baseline Configuration, PSD of Pointing Error in Y-Direction

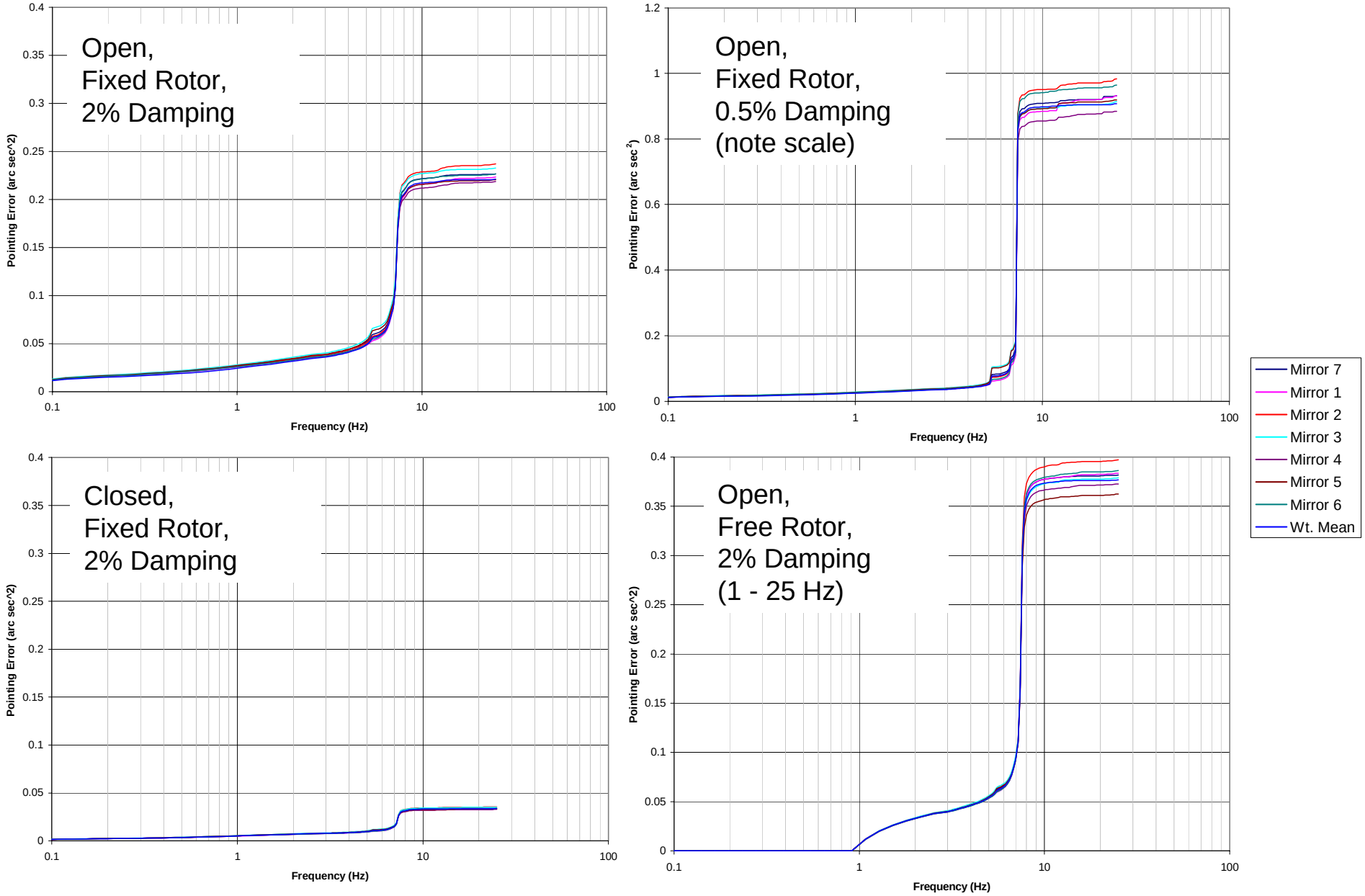

Figure 6-14 – Baseline Configuration, Cumulative Pointing Error in Y-Direction

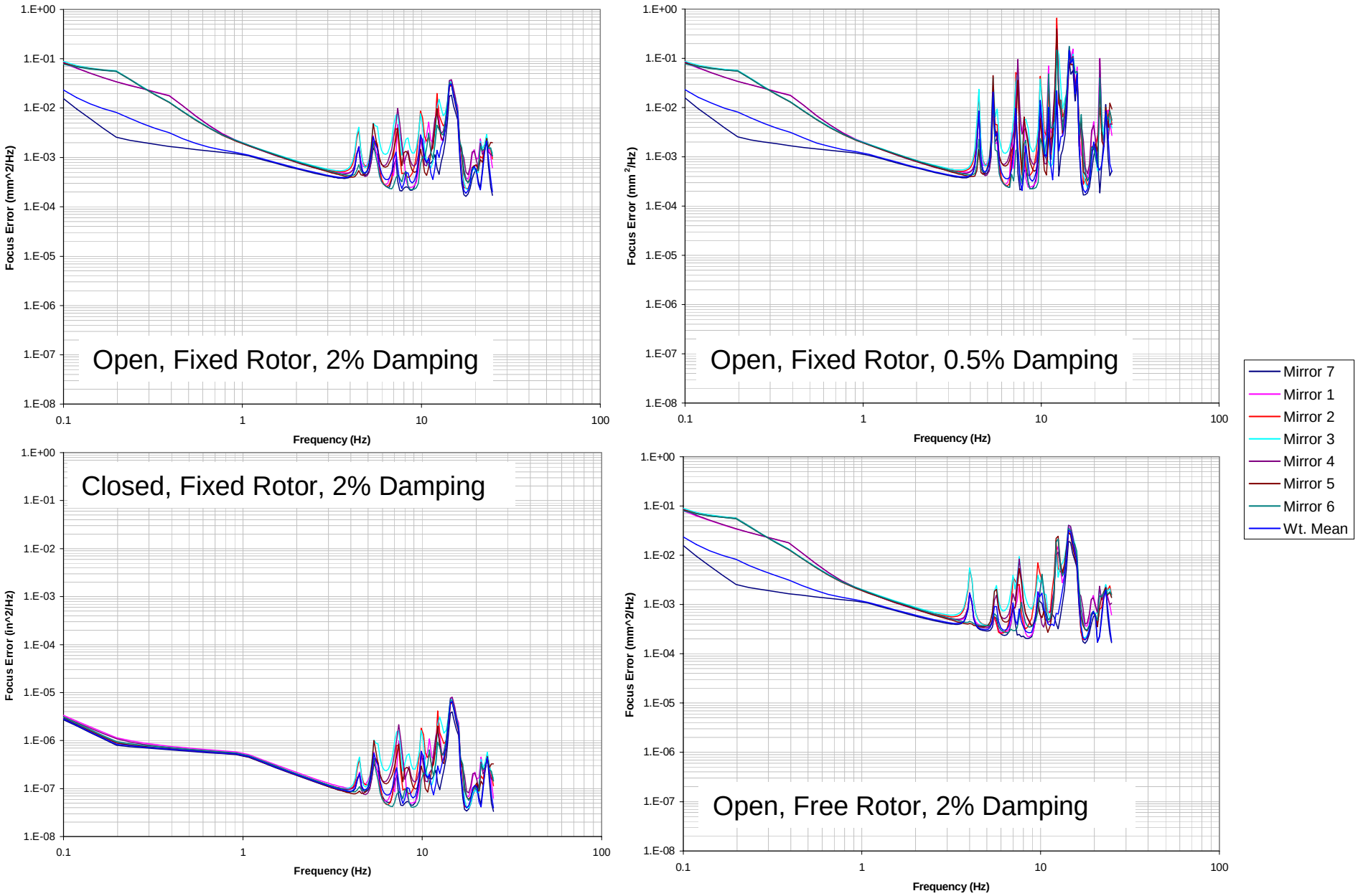

Figure 6-15 – Baseline Configuration, PSD of Focus Error

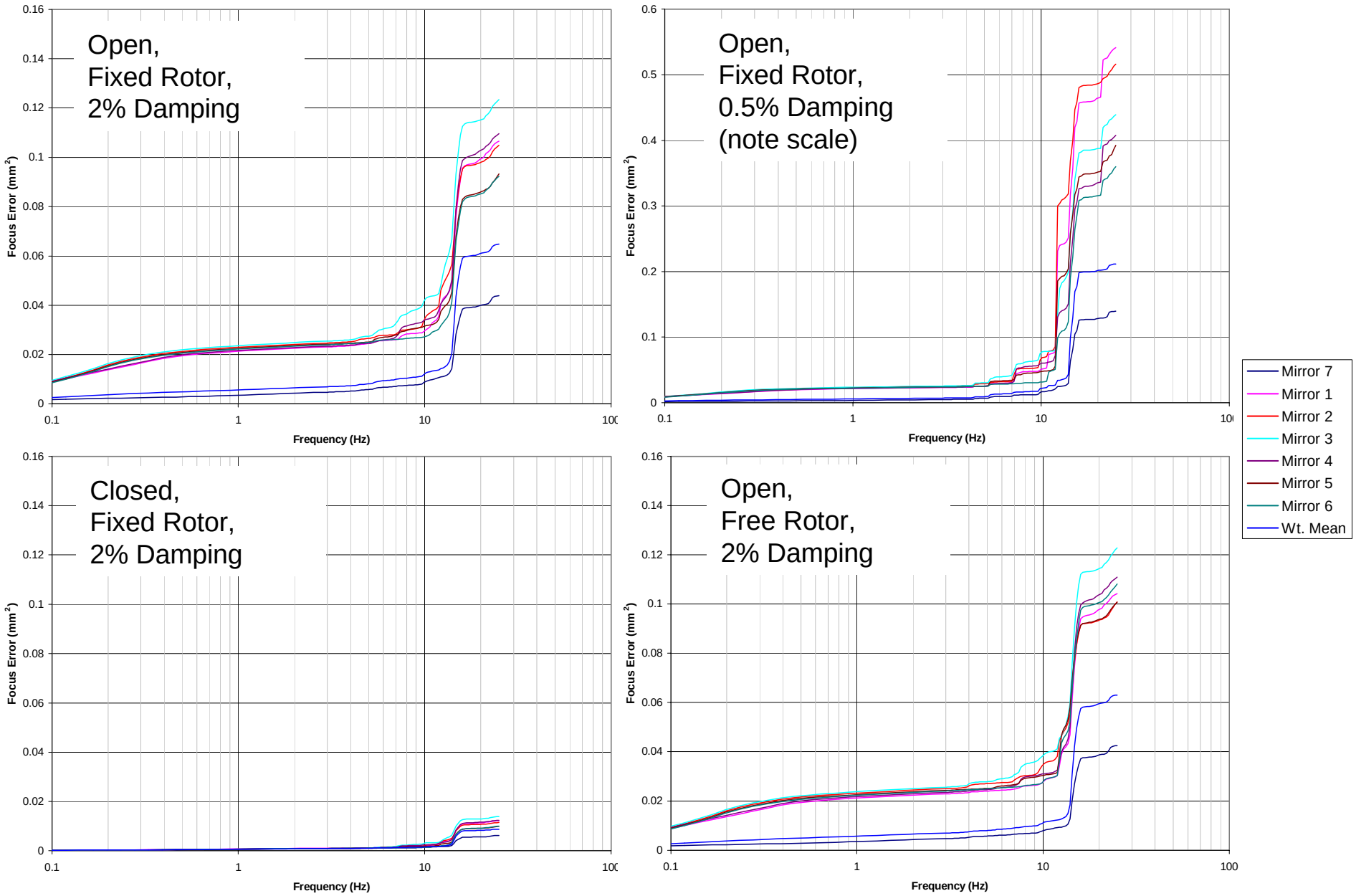

Figure 6-16 – Baseline Configuration, Cumulative Focus Error

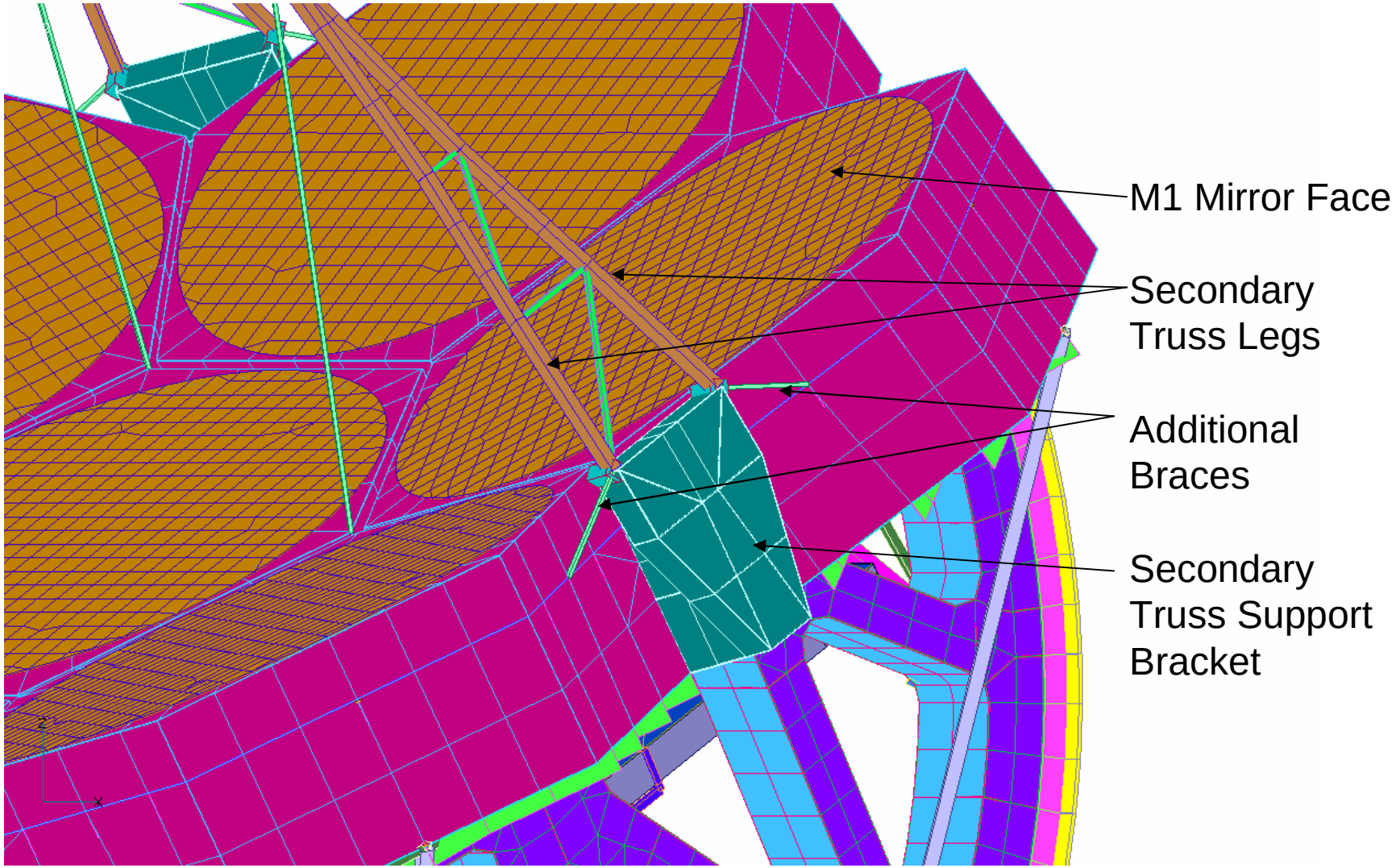

Figure 7-1 – Braces for Secondary Truss Support Bracket

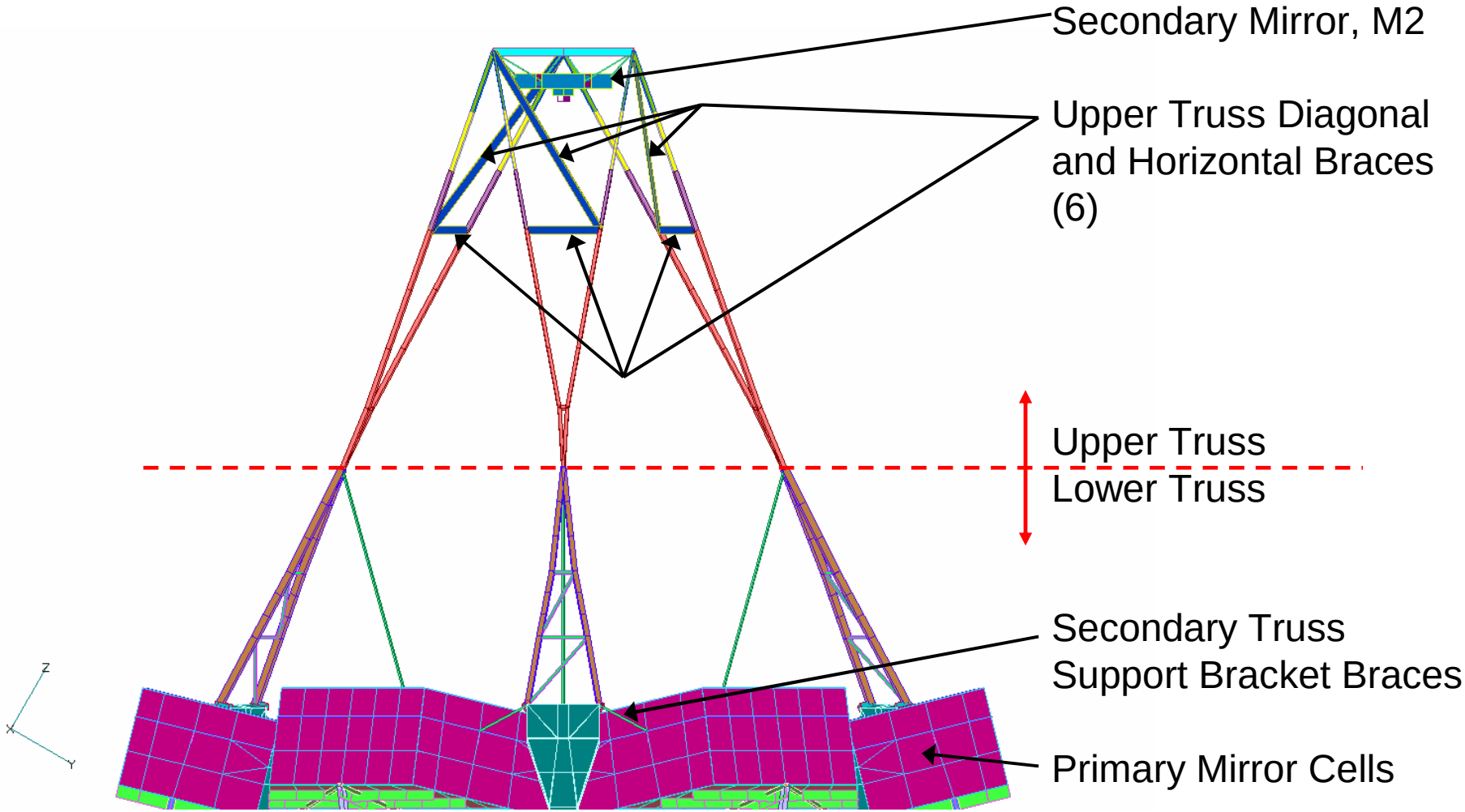

Figure 7-2 – Diagonal and Horizontal Braces for Upper Truss

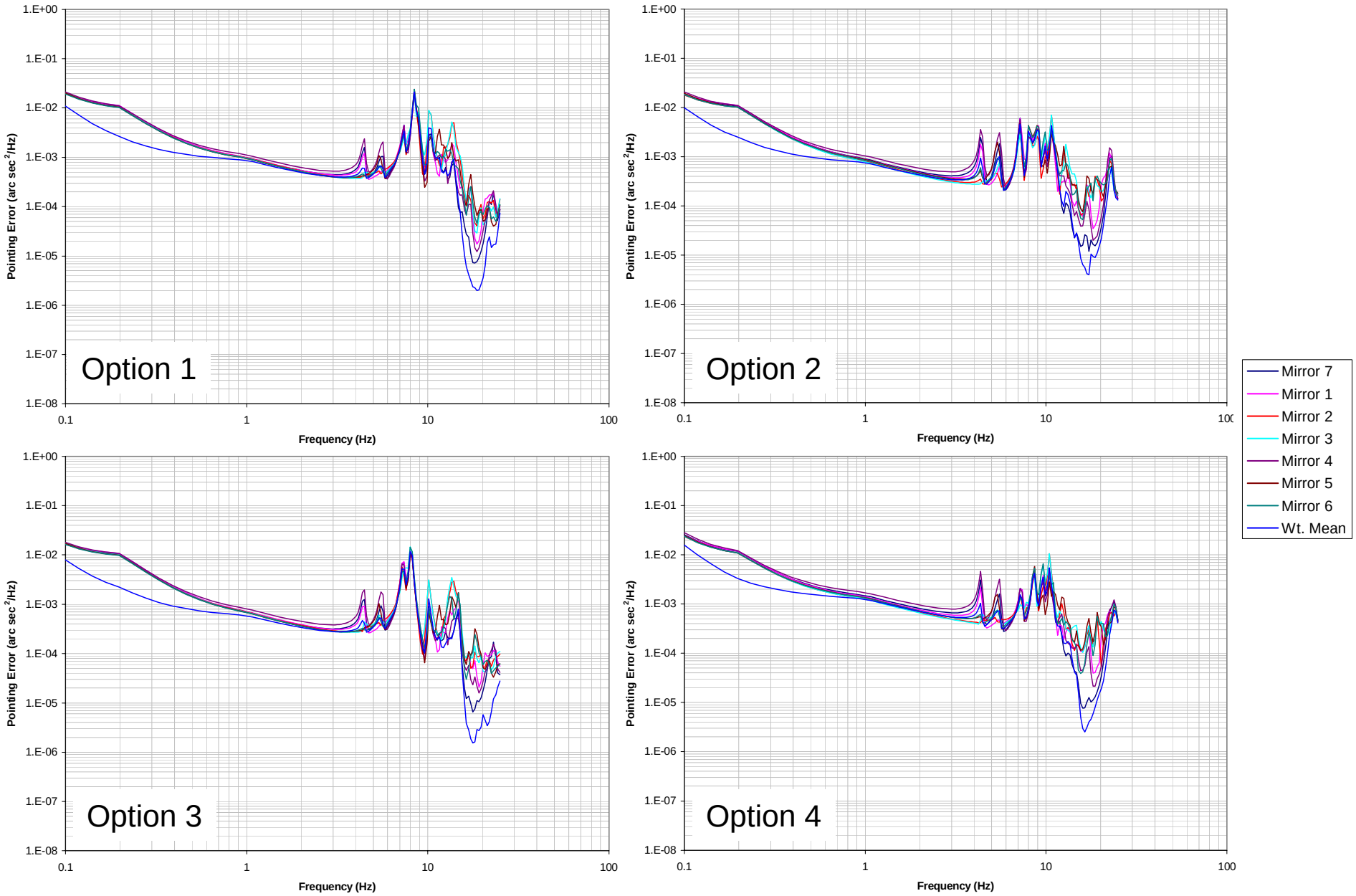

Figure 7-3 – Secondary Truss Stiffening Options, PSD of Pointing Error in X-Direction

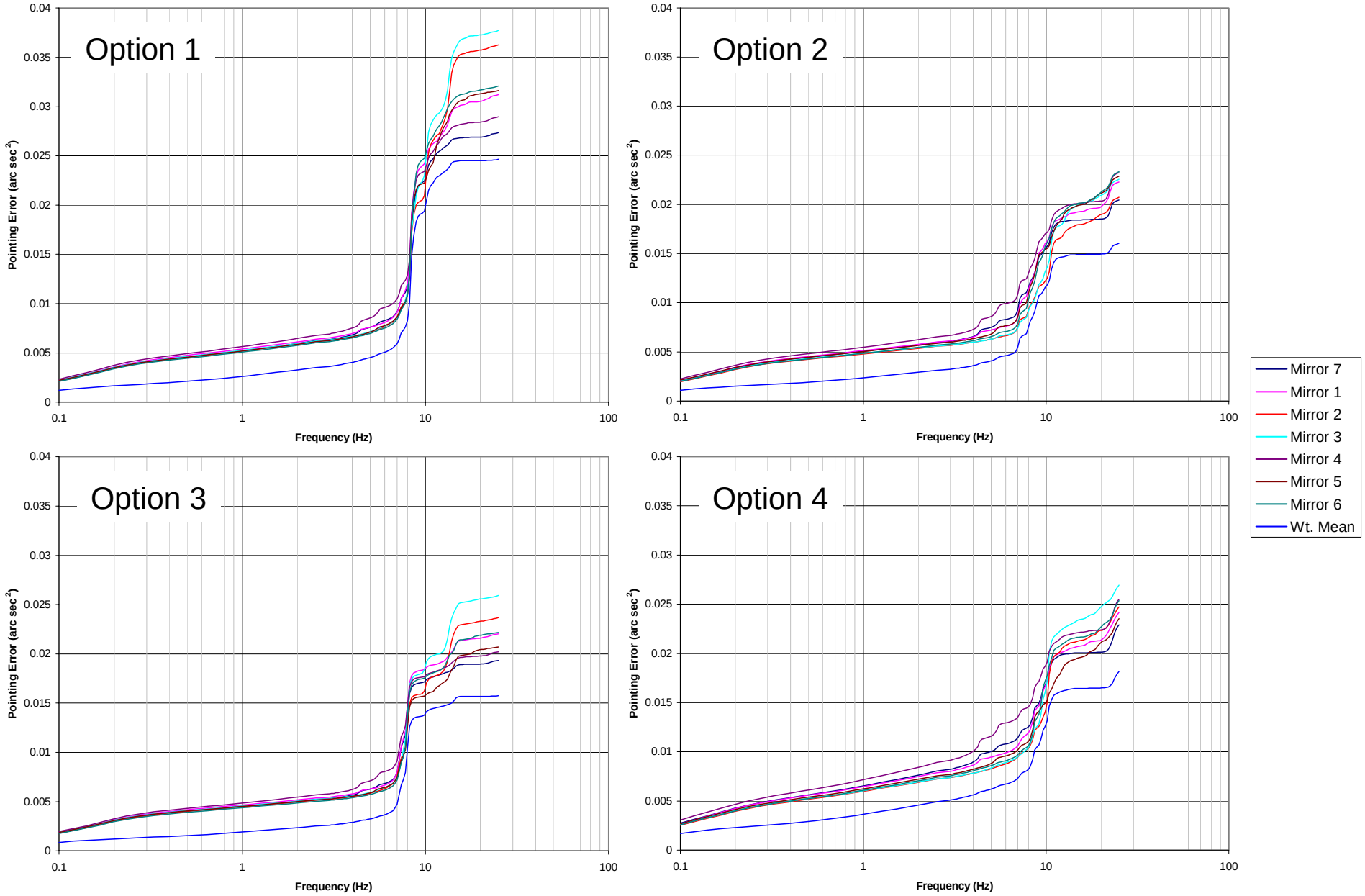

Figure 7-4 – Secondary Truss Stiffening Options, Cumulative Pointing Error in X-Direction

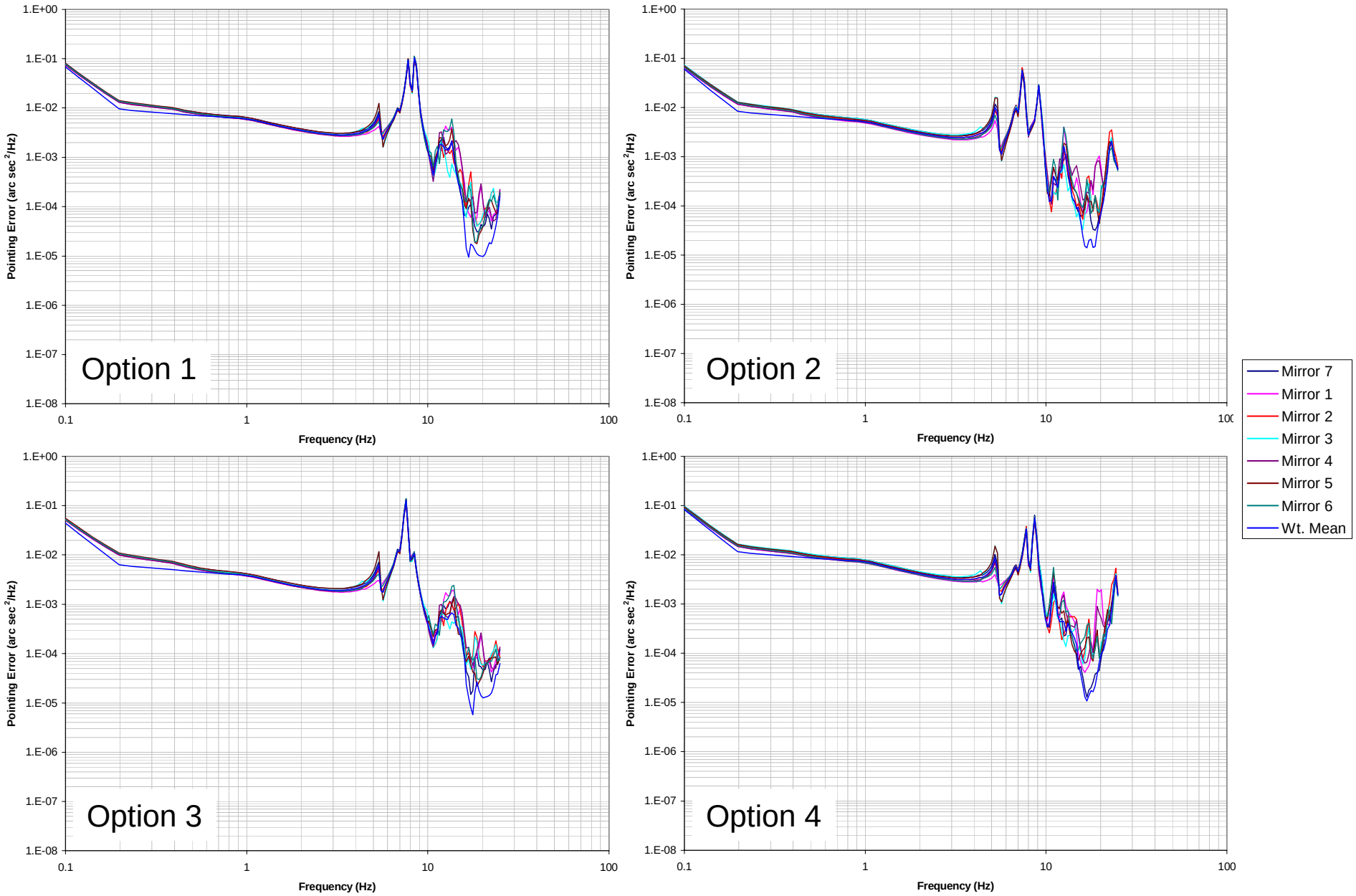

Figure 7-5 – Secondary Truss Stiffening Options, PSD of Pointing Error in Y-Direction

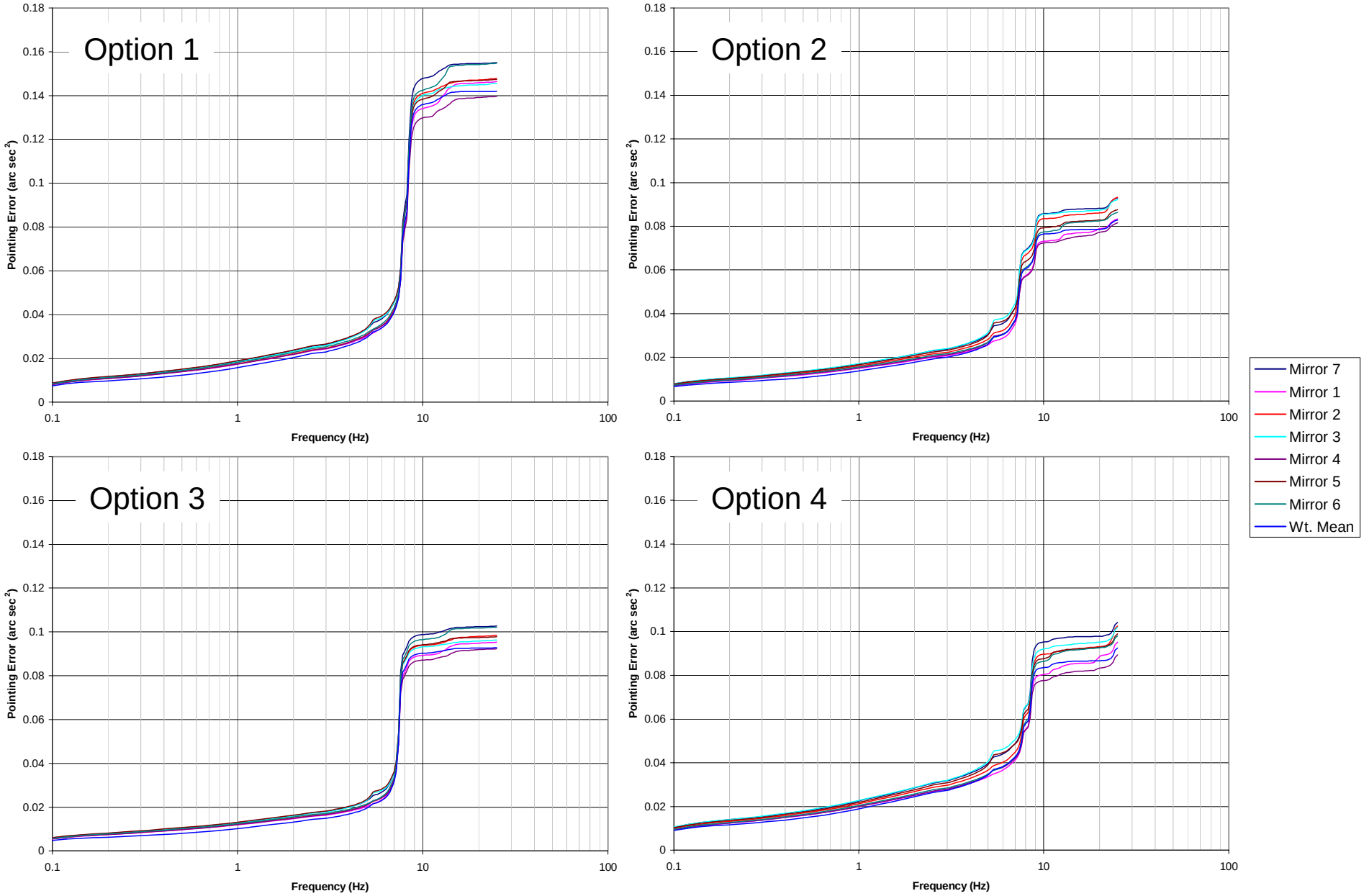

Figure 7-6 – Secondary Truss Stiffening Options, Cumulative Pointing Error in Y-Direction

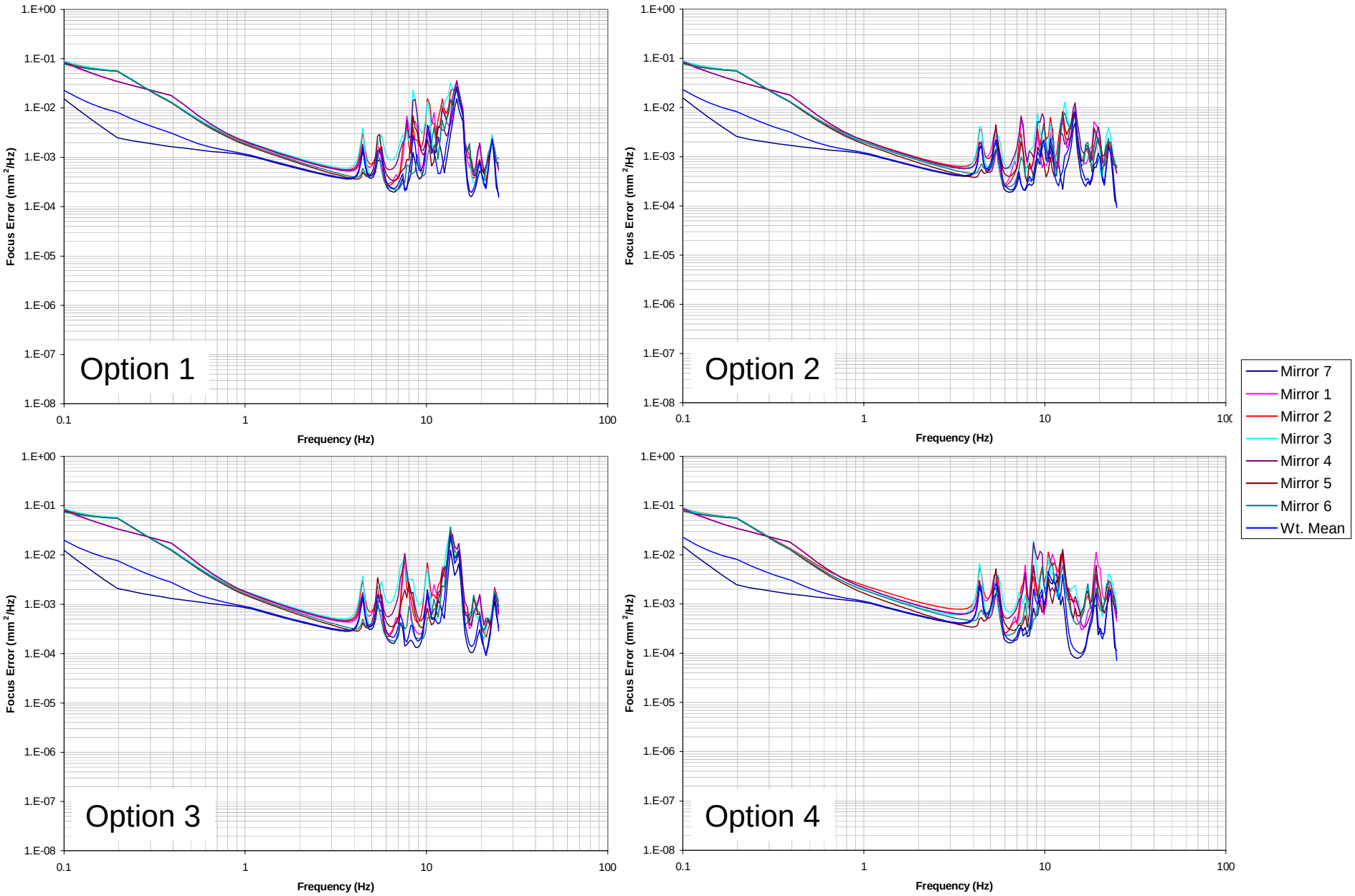

Figure 7-7 – Secondary Truss Stiffening Options, PSD of Focus Error

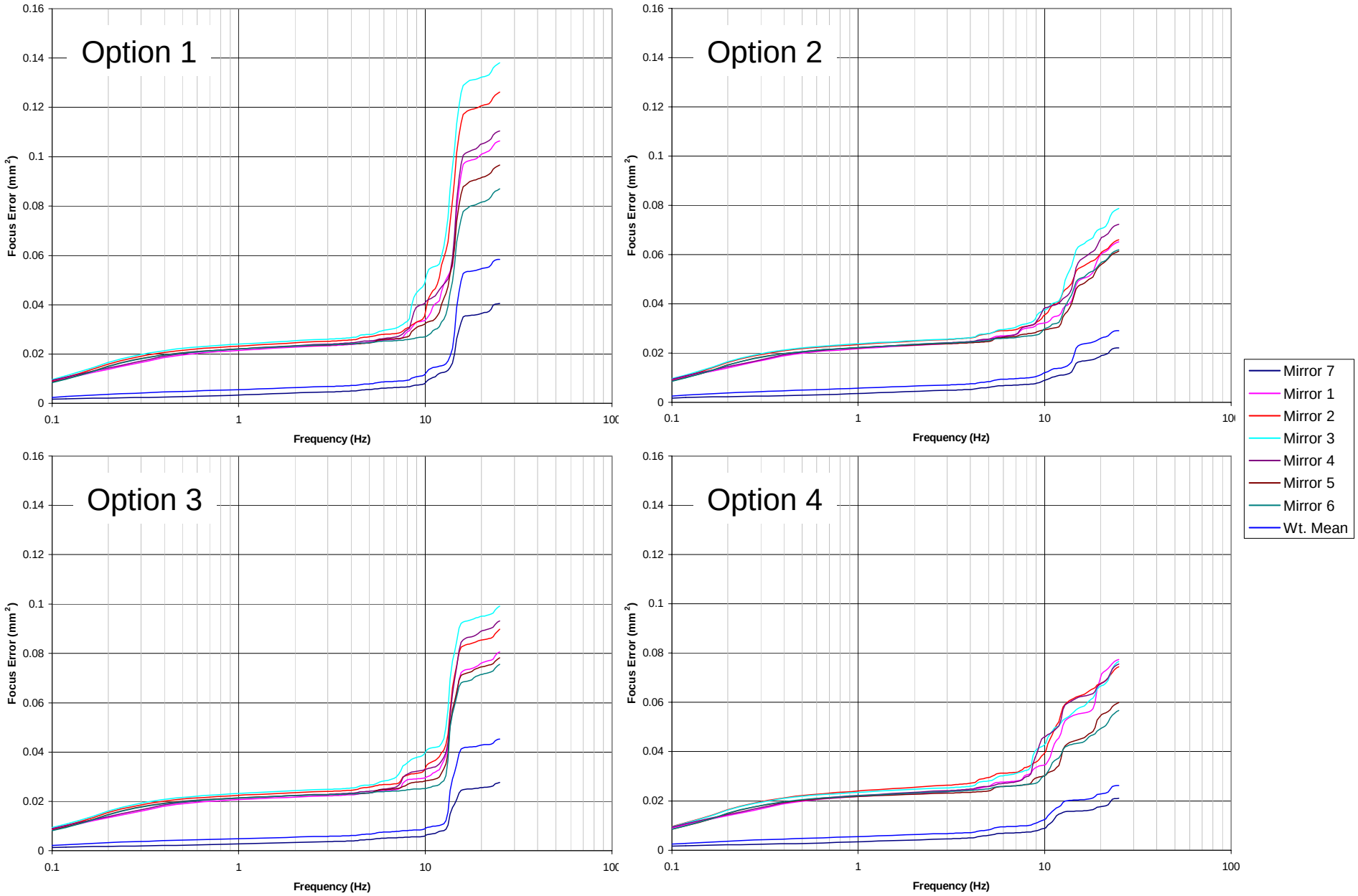

Figure 7-8 – Secondary Truss Stiffening Options, Cumulative Focus Error

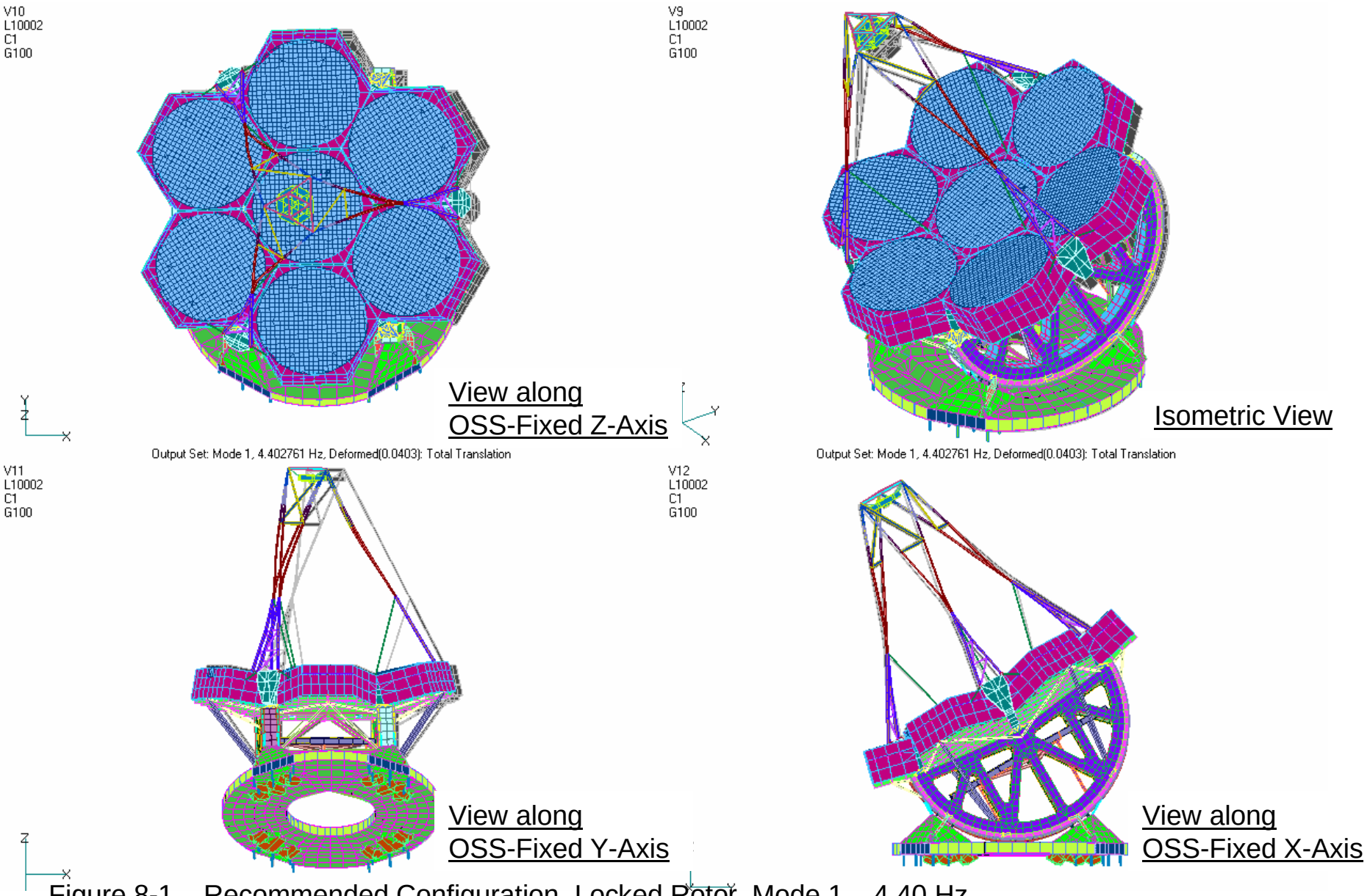

Figure 8-1 – Recommended Configuration, Locked Rotor, Mode 1 – 4.40 Hz
Undeformed Model in Grey

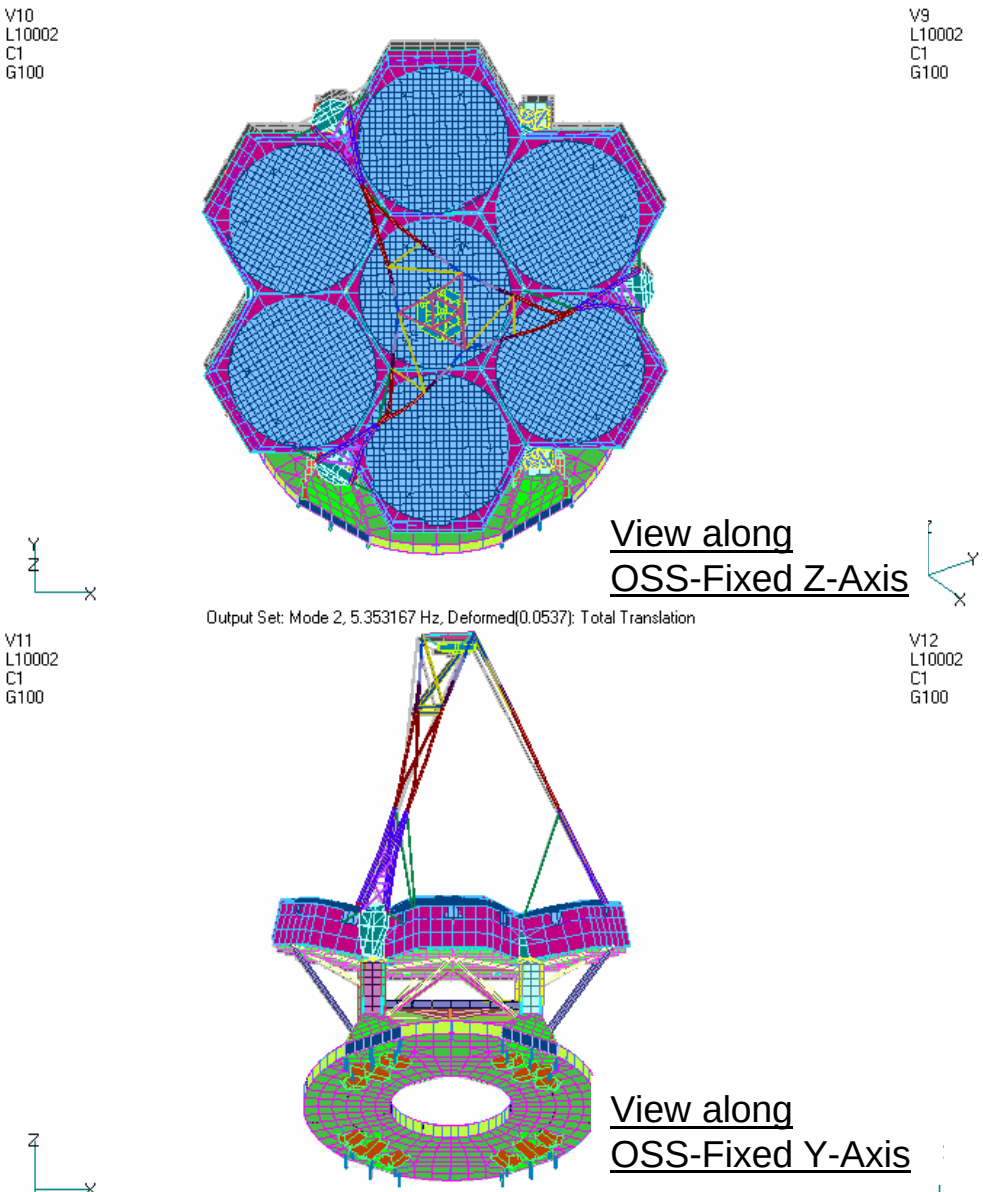

Figure 8-2 – Recommended Configuration, Locked Rotor, Mode 2 – 5.35 Hz
Undeformed Model in Grey

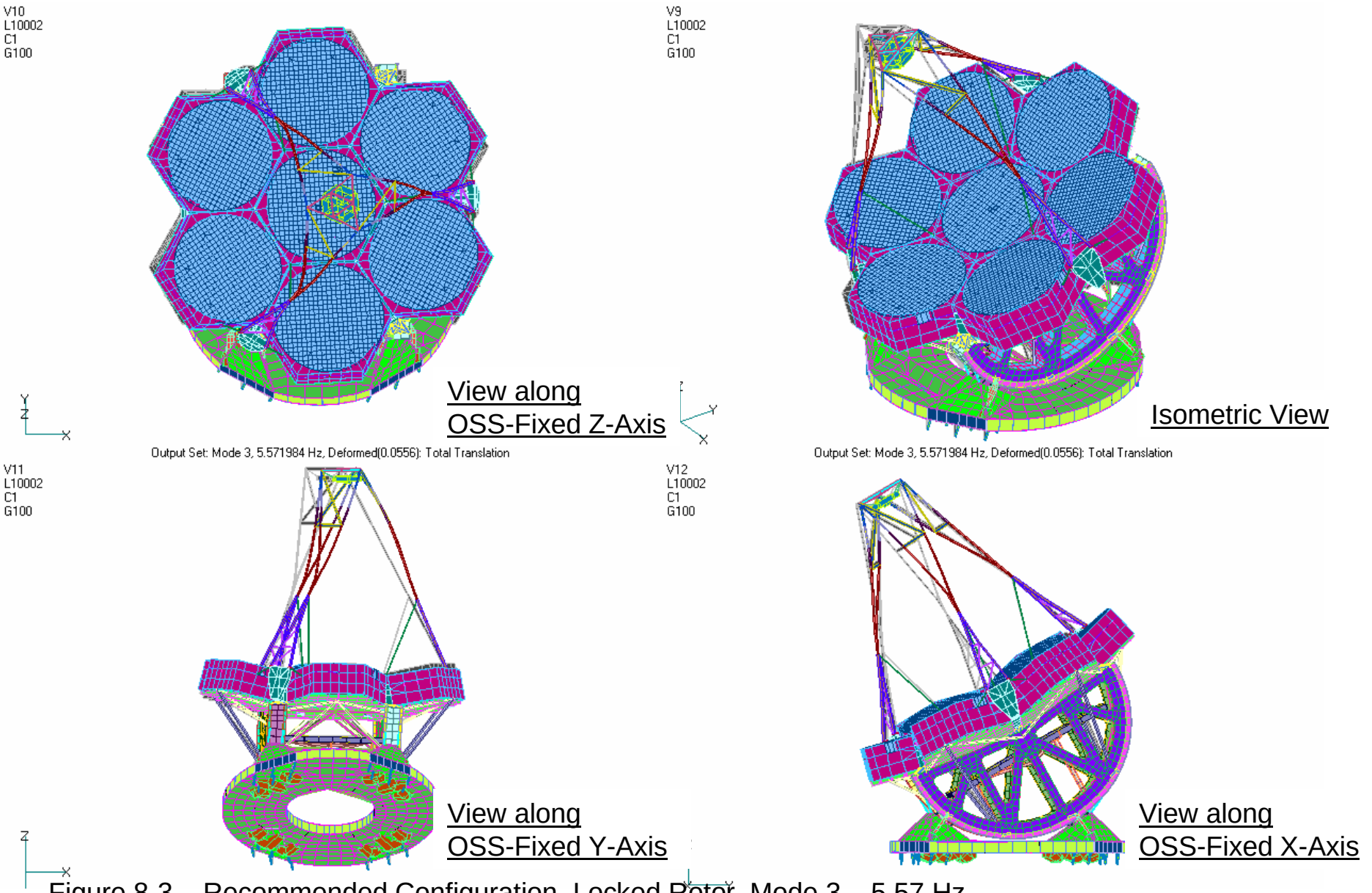

Figure 8-3 – Recommended Configuration, Locked Rotor, Mode 3 – 5.57 Hz
Undeformed Model in Grey

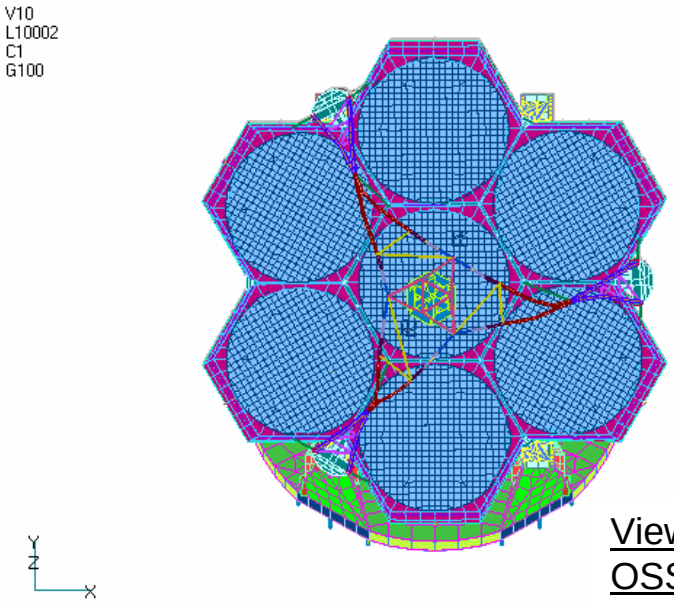

View along OSS-Fixed Z-Axis

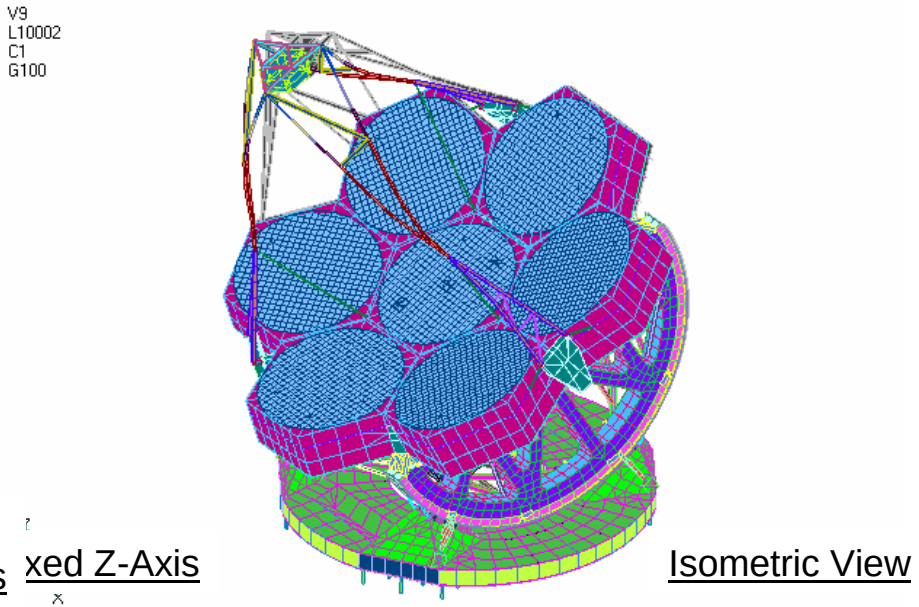

xed Z-Axis

Isometric View

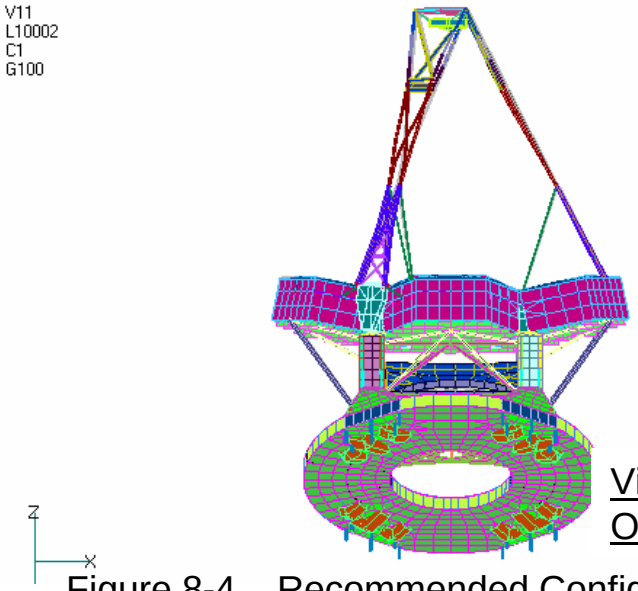

View along OSS-Fixed Y-Axis

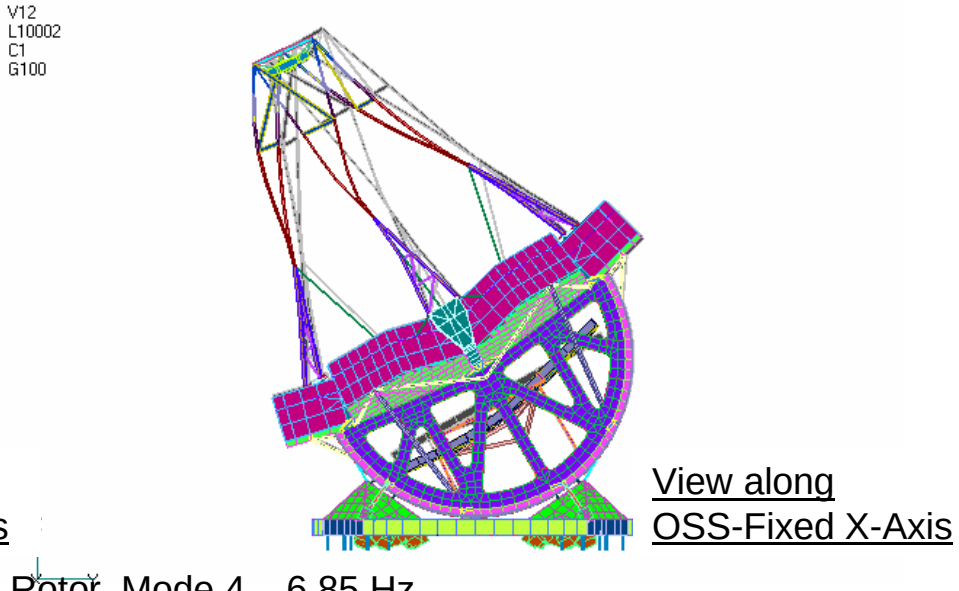

View along OSS-Fixed X-Axis

Figure 8-4 – Recommended Configuration, Locked Rotor, Mode 4 – 6.85 Hz
Undeformed Model in Grey

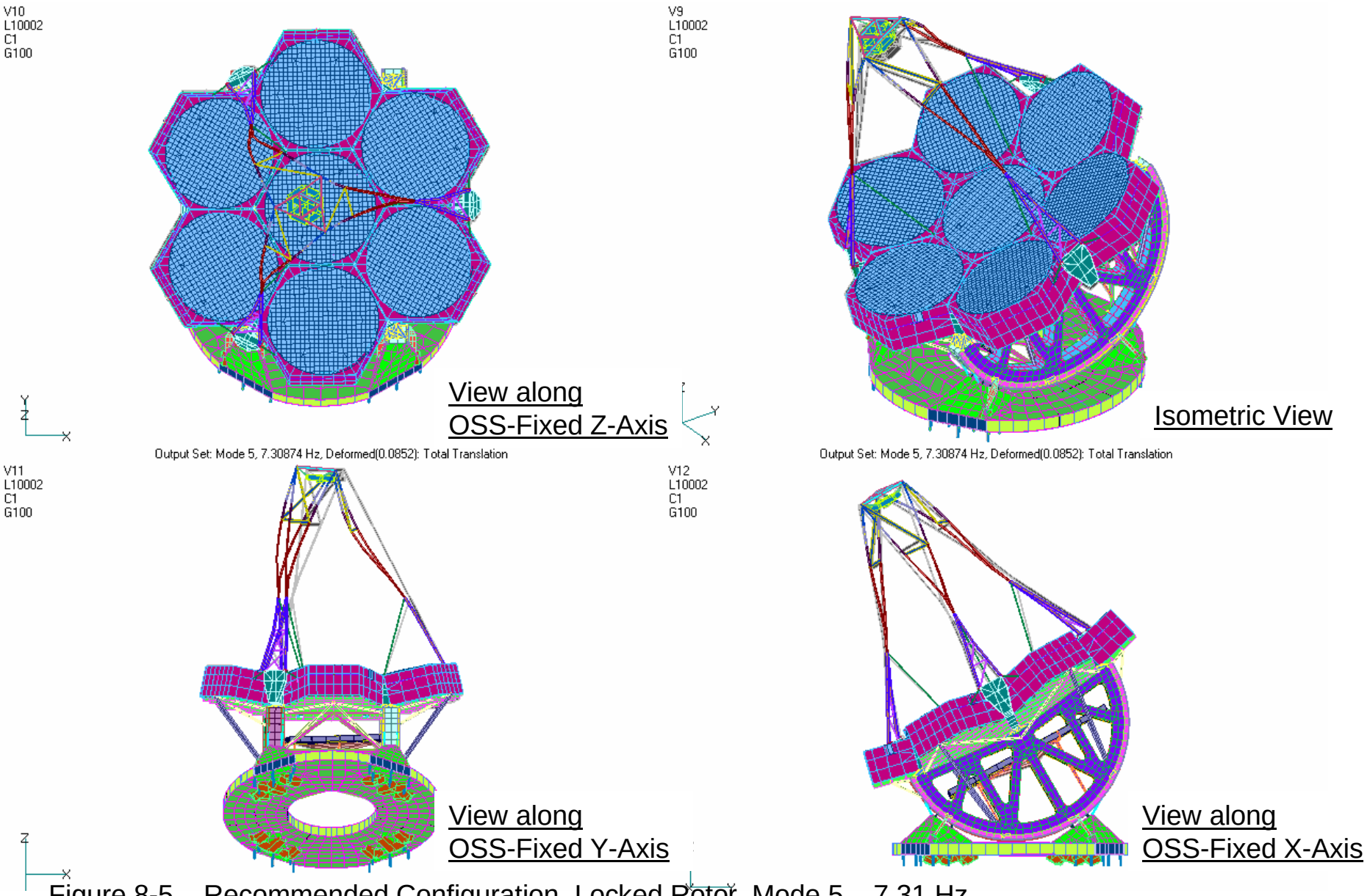

Figure 8-5 – Recommended Configuration, Locked Rotor, Mode 5 – 7.31 Hz
Undeformed Model in Grey

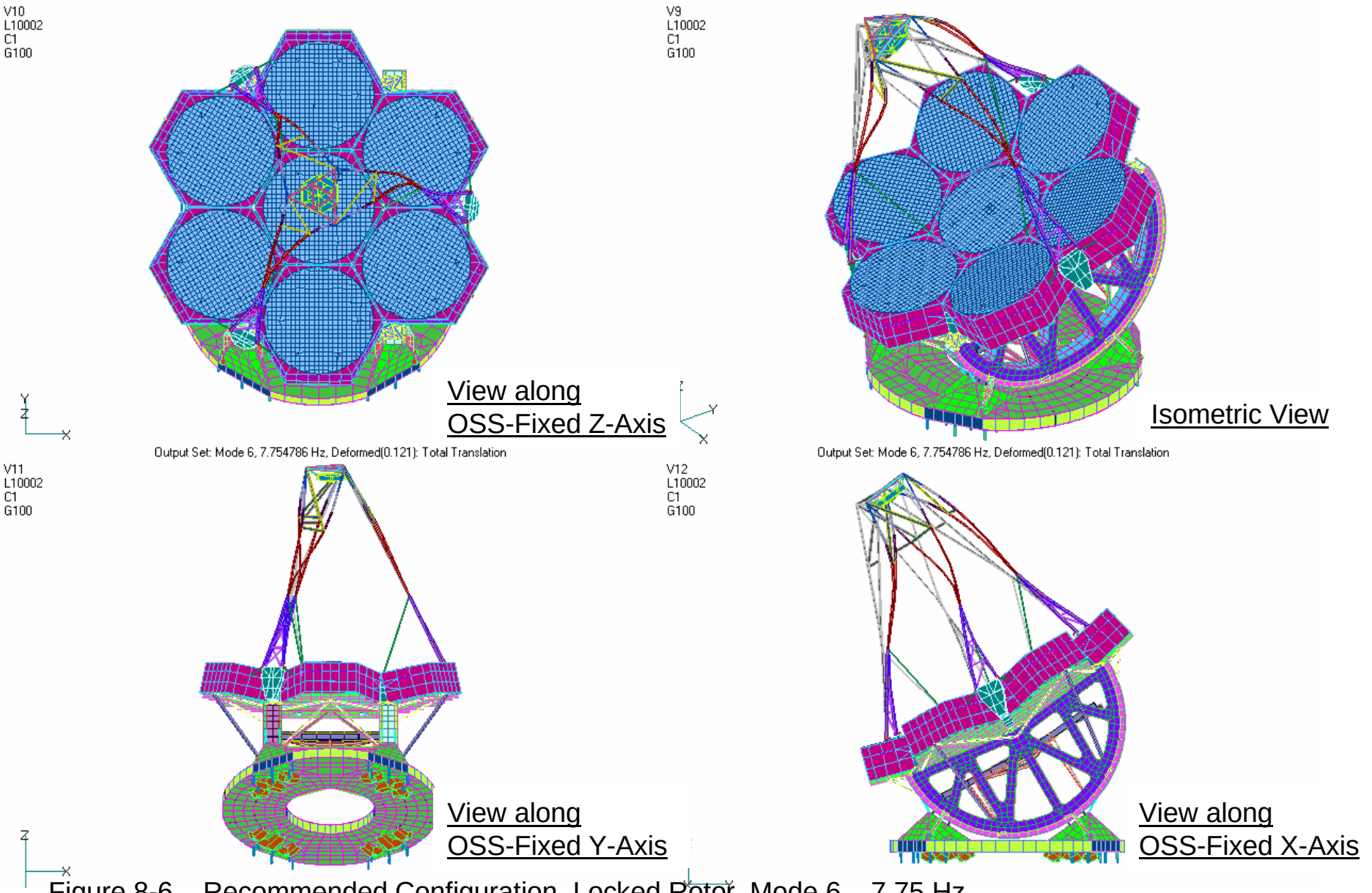

Figure 8-6 – Recommended Configuration, Locked Rotor, Mode 6 – 7.75 Hz
Undeformed Model in Grey

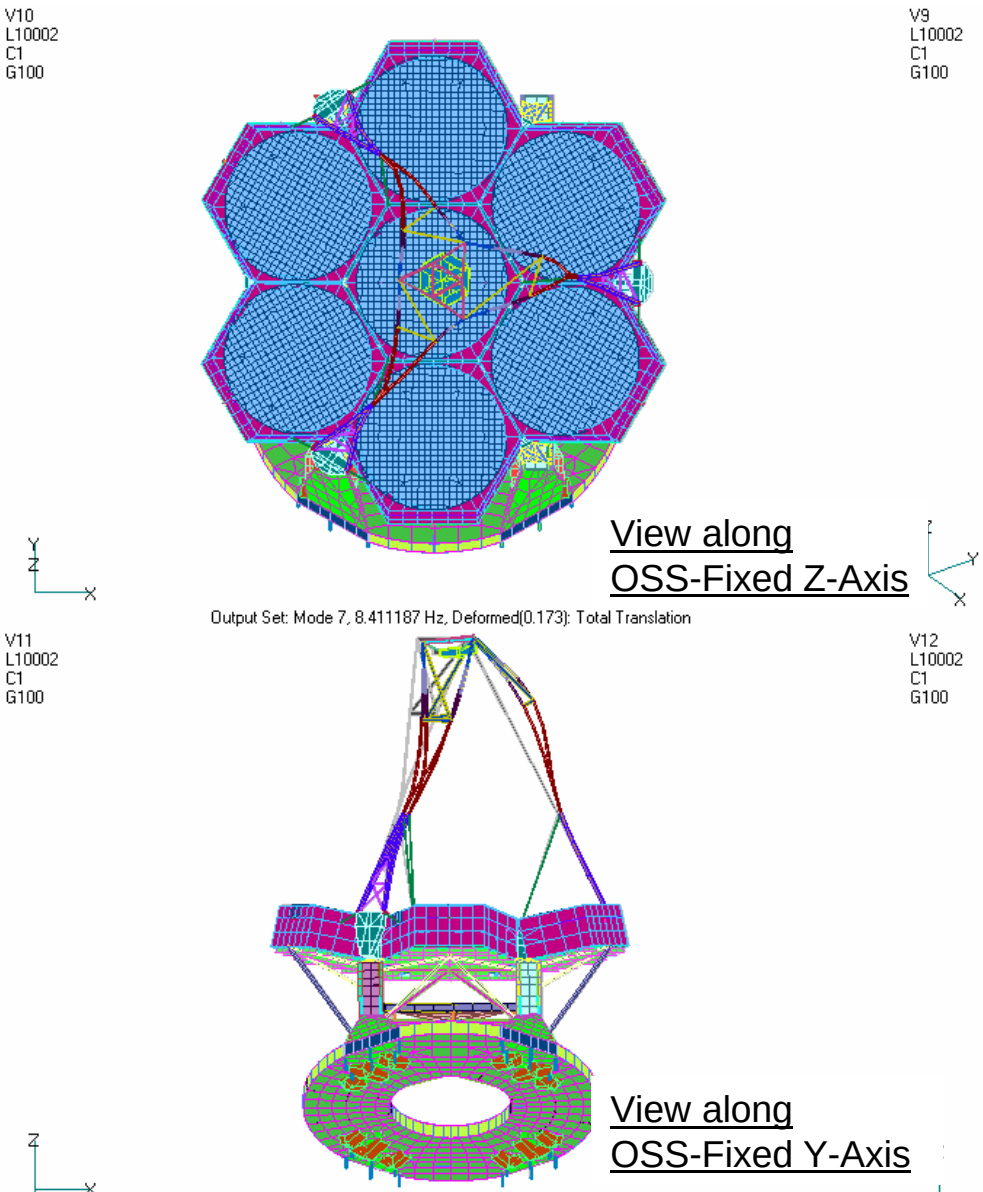

Figure 8-7 – Recommended Configuration, Locked Rotor, Mode 7 – 8.41 Hz
Undeformed Model in Grey

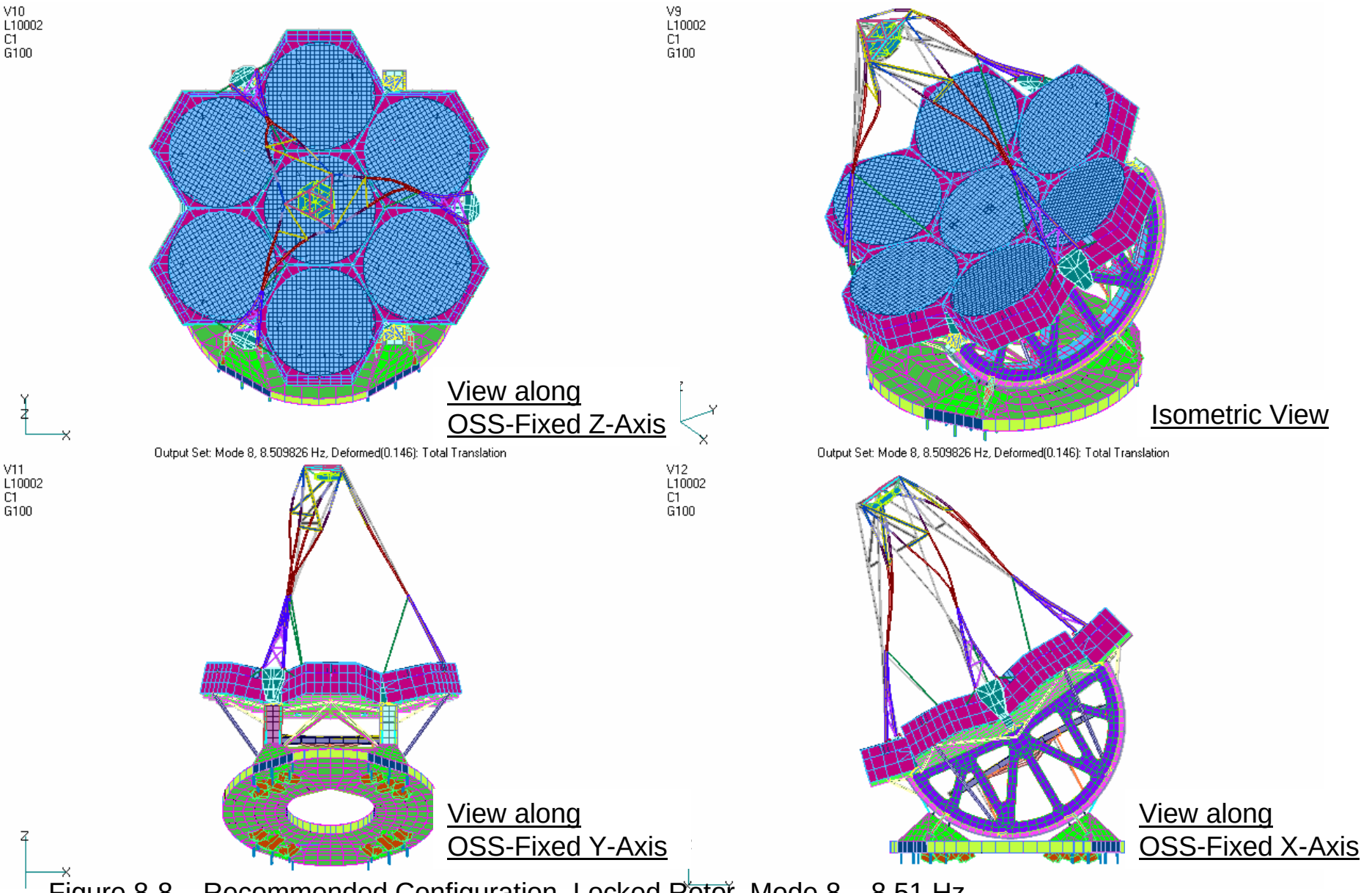

Figure 8-8 – Recommended Configuration, Locked Rotor, Mode 8 – 8.51 Hz
Undeformed Model in Grey

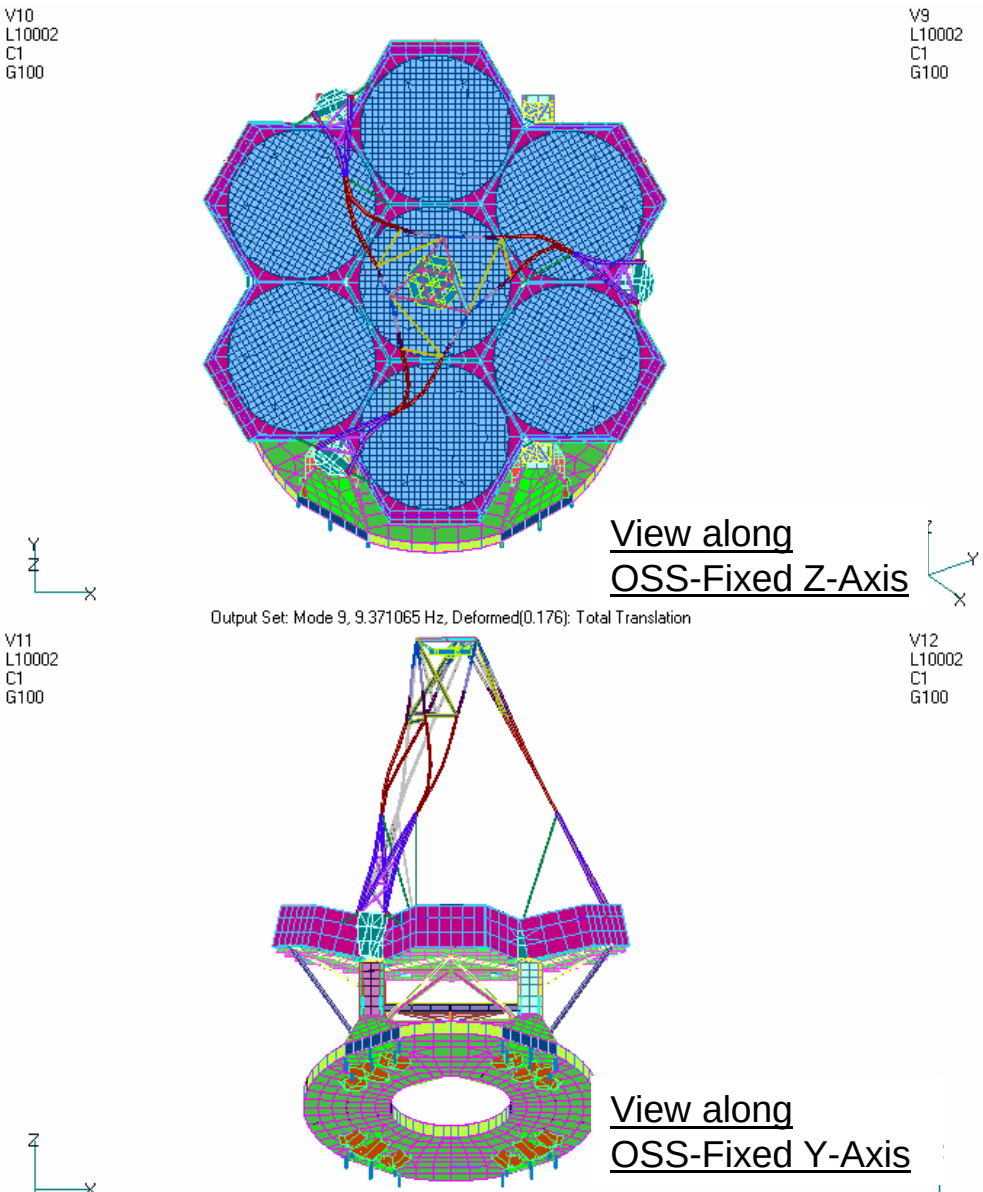

Figure 8-9 – Recommended Configuration, Locked Rotor, Mode 9 – 9.37 Hz
Undeformed Model in Grey

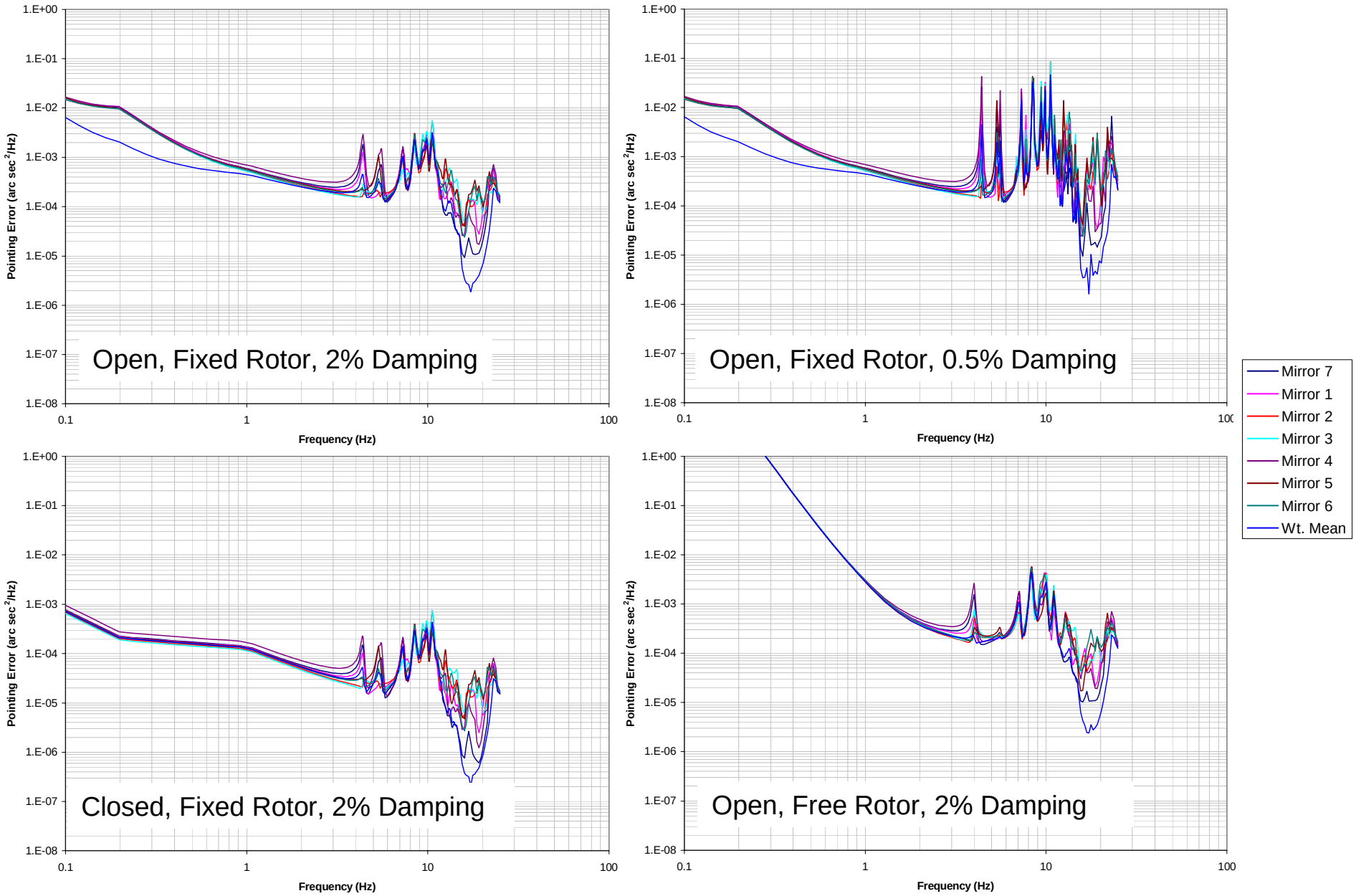

Figure 8-10 – Recommended Configuration, PSD of Pointing Error in X-Direction

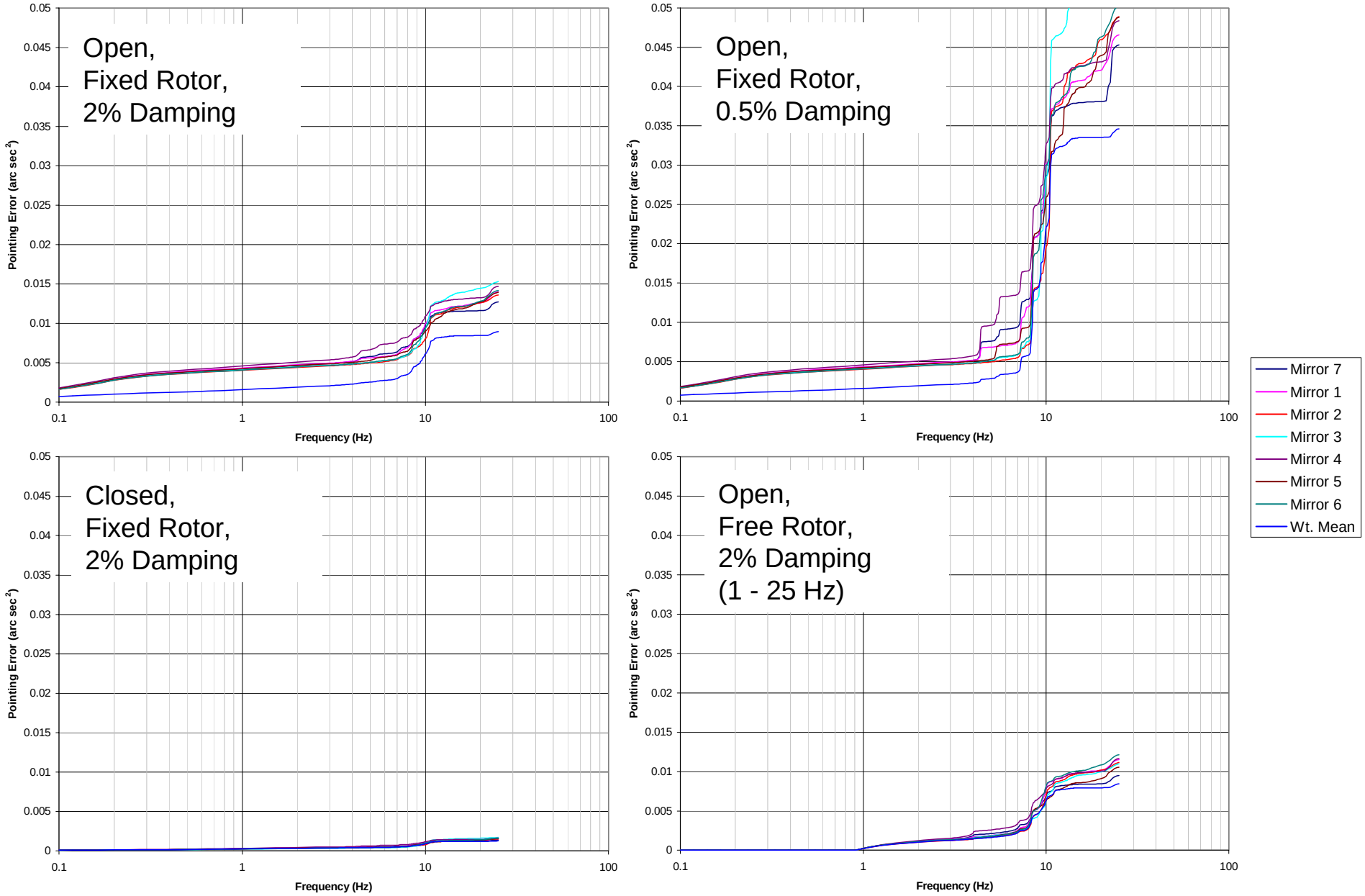

Figure 8-11 – Recommended Configuration, Cumulative Pointing Error in X-Direction

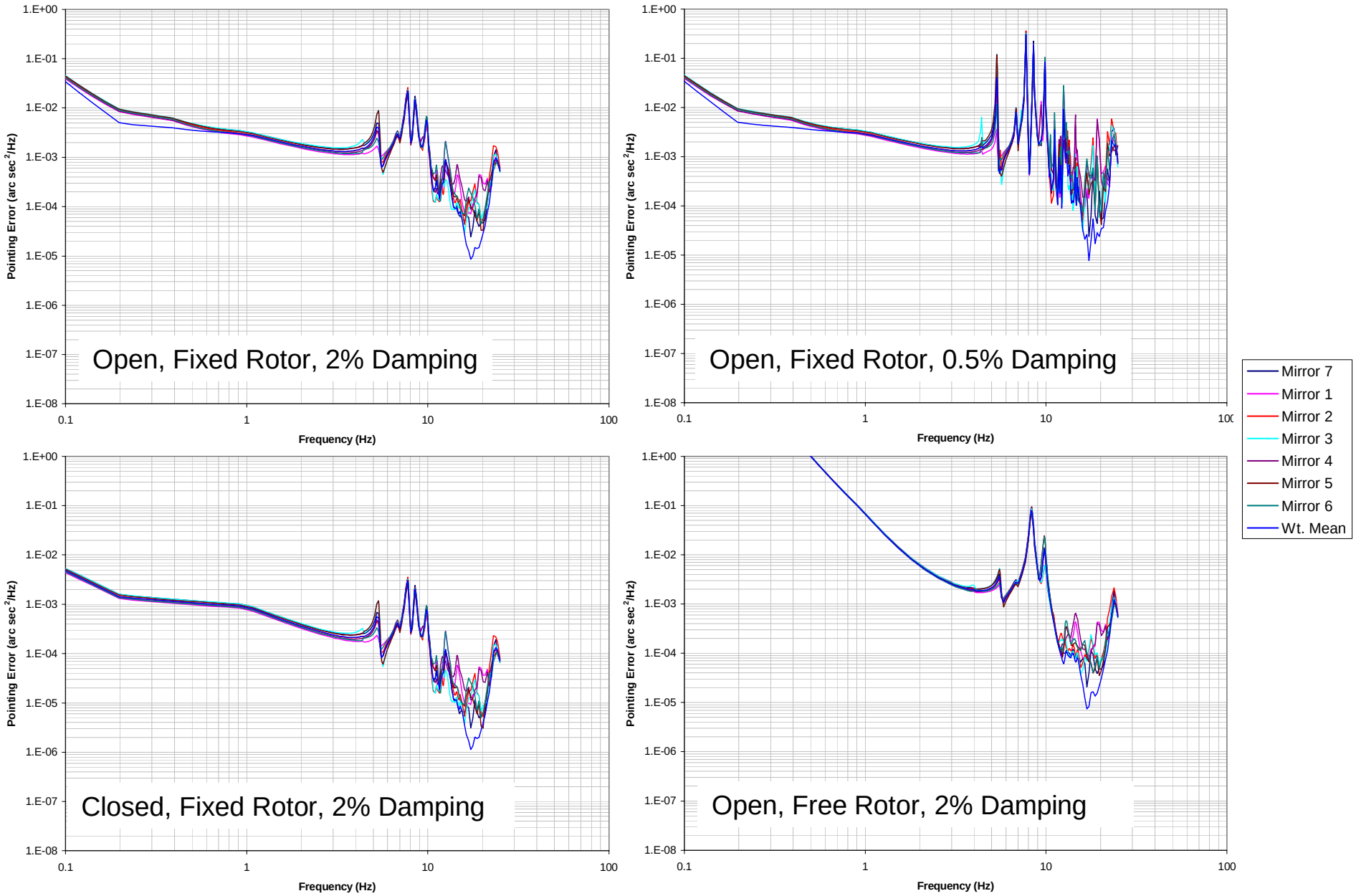

Figure 8-12 – Recommended Configuration, PSD of Pointing Error in Y-Direction

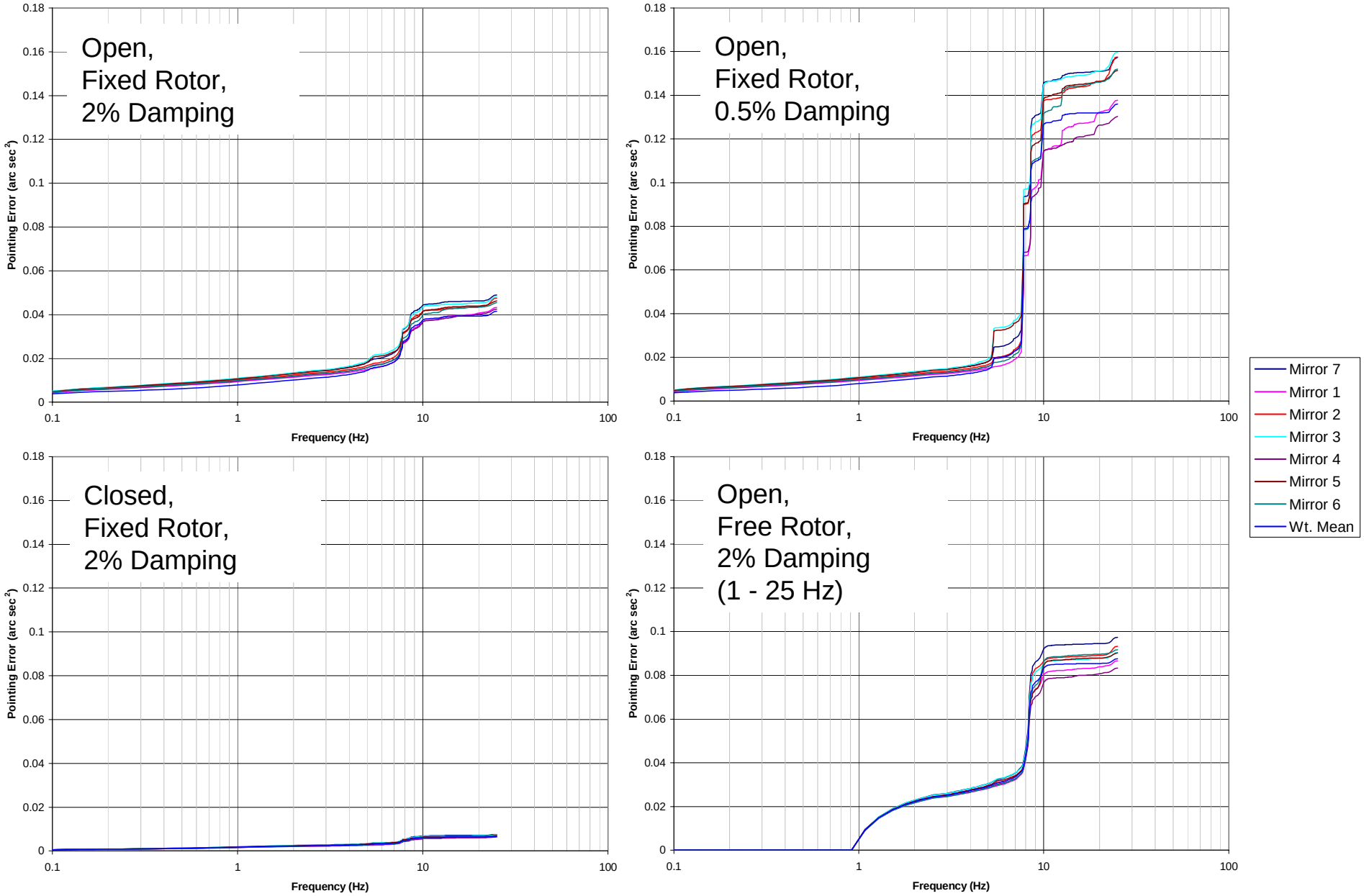

Figure 8-13 – Recommended Configuration, Cumulative Pointing Error in Y-Direction

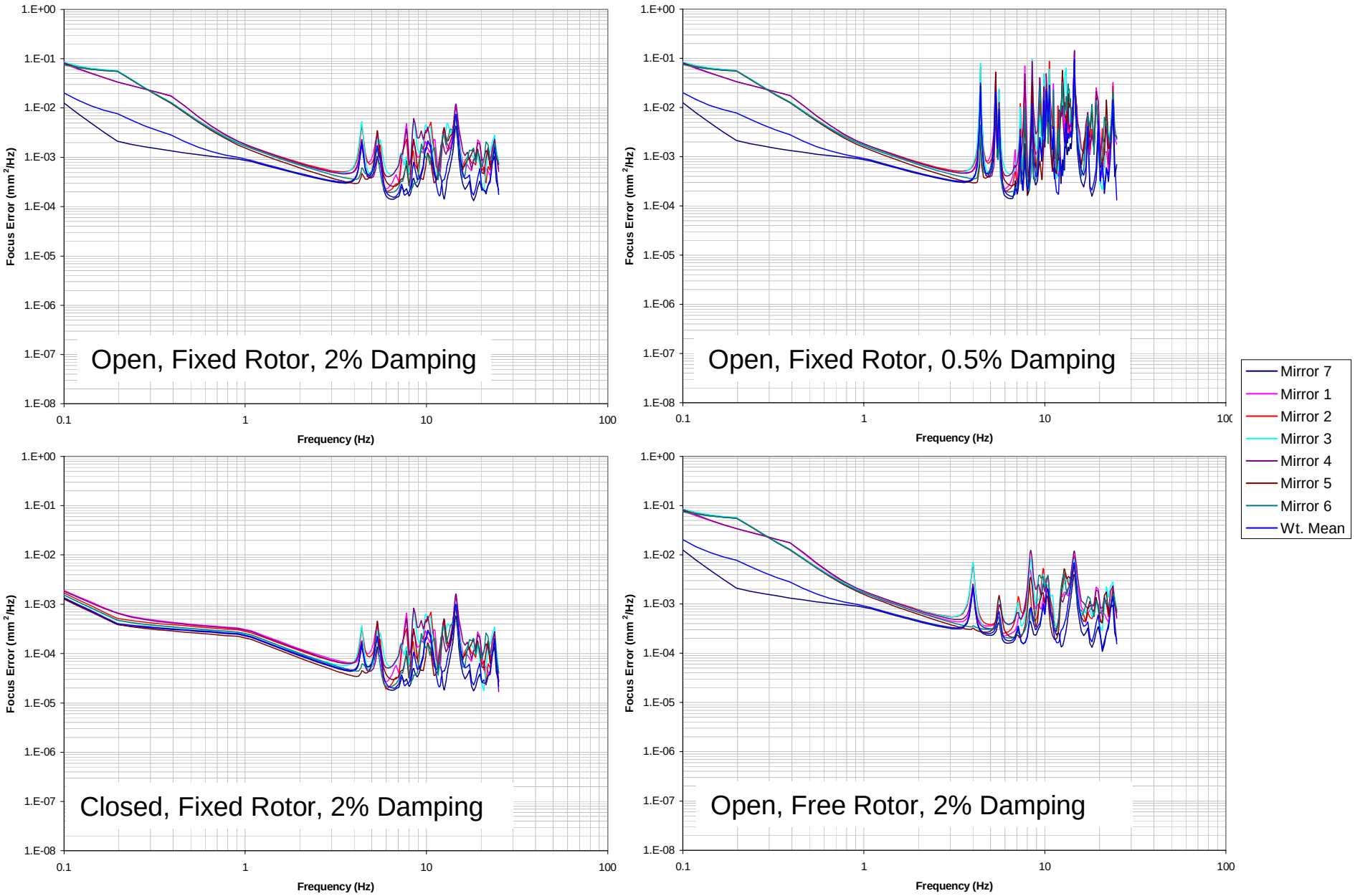

Figure 8-14 – Recommended Configuration, PSD of Focus Error

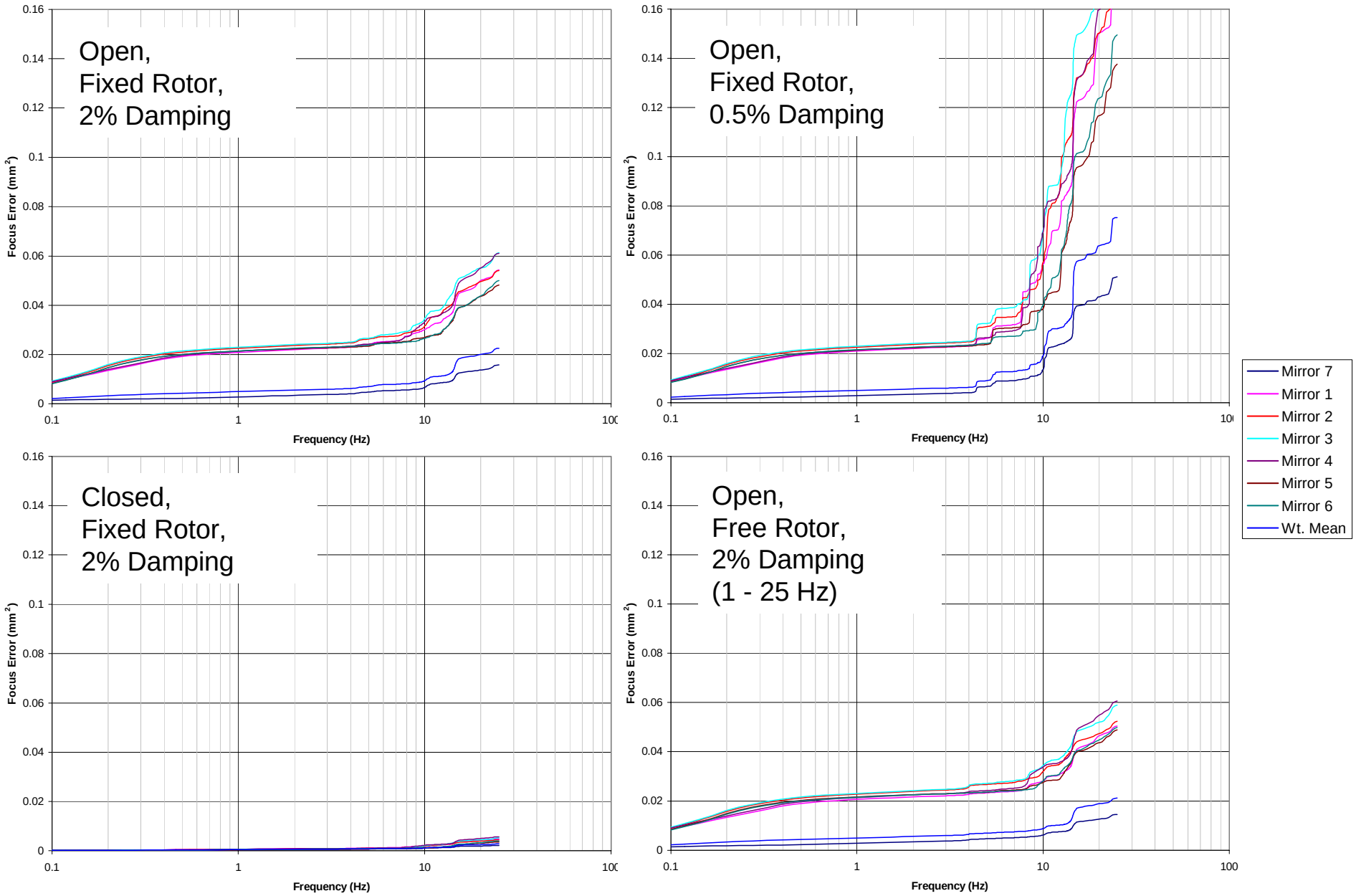

Figure 8-15 – Recommended Configuration, Cumulative Focus Error